

Washington University in St. Louis

Washington University Open Scholarship

McKelvey School of Engineering Theses & Dissertations

McKelvey School of Engineering

Summer 8-15-2016

Nanoparticle Formation in the Flame Synthesis of Multicomponent Nanostructured Materials for Clean Energy Applications

Jiayi Fang

Washington University in St. Louis

Follow this and additional works at: https://openscholarship.wustl.edu/eng_etds



Part of the [Chemical Engineering Commons](#), and the [Environmental Engineering Commons](#)

Recommended Citation

Fang, Jiayi, "Nanoparticle Formation in the Flame Synthesis of Multicomponent Nanostructured Materials for Clean Energy Applications" (2016). *McKelvey School of Engineering Theses & Dissertations*. 186. https://openscholarship.wustl.edu/eng_etds/186

This Dissertation is brought to you for free and open access by the McKelvey School of Engineering at Washington University Open Scholarship. It has been accepted for inclusion in McKelvey School of Engineering Theses & Dissertations by an authorized administrator of Washington University Open Scholarship. For more information, please contact digital@wumail.wustl.edu.

WASHINGTON UNIVERSITY IN ST LOUIS

Department Of Energy Environmental and Chemical Engineering

Dissertation Examination Committee:

Pratim Biswas, Chair

Richard L. Axelbaum

Parag Banerjee

Subramanya Herle

Dale R. Powers

Palghat Ramachandran

Brent Williams

Nanoparticle Formation in the Flame Synthesis of Multicomponent Nanostructured Materials for
Clean Energy Applications

by

Jiaxi Fang

A dissertation presented to the
Graduate School of Arts and Sciences
of Washington University in
partial fulfillment for the degree
of Doctor of Philosophy

August 2016

Saint Louis, Missouri

©2016, Jiayi Fang

Table of Contents

List of Figures	v
List of Tables	xii
Acknowledgements	xiv
Abstract	xvii
1. Introduction.....	1
1.1 Overview	2
1.2 Motivation.....	2
1.3 Background on combustion synthesis.....	4
1.4 Measurements of particle growth in flame aerosol reactors	6
1.5 Flame chemistry measurements	8
1.6 Precursor decomposition pathways:	9
1.7 Charging in flames	12
1.8 Sub 2nm cluster classification and mobility	13
1.9 Approach.....	19
1.10 References.....	20
2. Measurement of Sub 2 nm Clusters of Pristine and Composite Metal Oxides during Nanomaterials Synthesis in Flame Aerosol Reactors	25
2.1 Abstract	26
2.2 Introduction	27
2.3 Experimental Methods	29
2.3.1 Synthesis of TiO ₂ in a Flat Flame Aerosol Reactor	29
2.3.2 Utilization of a Half Mini DMA for Online Measurement of Sub 2 nm Clusters	31
2.3.3 Atomic Force Microscopy of Sub 2 nm TiO ₂ clusters	32

2.3.4	Electrical Mobility of Sub 2 nm Clusters	32
2.3.5	Experimental Plan.....	34
2.4	Results and Discussion.....	35
2.4.1	Single Component Nanoparticle Synthesis	36
2.4.2	Effect of Precursor Feed Rate	39
2.4.3	Effect of Sampling Height	40
2.4.4	Synthesis of Multicomponent TiO ₂ /SiO ₂ Nanocomposites	41
2.5	Conclusions	42
2.6	References	43
3.	Cluster Formation Mechanisms of Titanium Dioxide During Combustion Synthesis	49
3.1	Abstract	50
3.2	Introduction.....	51
3.3	Material and Methods	52
3.3.1	Flame aerosol reactor.....	53
3.3.2	API-TOF MS measurements of sub 2nm clusters in a flame aerosol reactor.....	54
3.3.3	Experimental plan.....	54
3.3.4	Reaction mechanisms of TiO ₂ in flames.....	56
3.4	Results and discussion	57
3.4.1	Background ions measured in methane air premixed combustion	57
3.4.2	Titanium dioxide particle formation during combustion synthesis	59
3.4.3	Mass defect plots.....	64
3.5	Conclusions	67
3.6	References	68
4.	The Initial Stages of Multicomponent Particle Formation During the Combustion Synthesis of Mixed SiO ₂ /TiO ₂	71
4.1	Abstract	72
4.2	Introduction.....	73
4.3	Material and Methods	75

4.3.1	Size resolved chemistry with tandem ion mobility spectrometry – mass spectrometry (IMS-MS)	77
4.3.2	Experimental plan	78
4.4	Results and discussion	79
4.4.1	Single component particle growth mechanisms.	79
4.4.2	Multicomponent new particle formation	85
4.4.3	Tandem Ion Mobility Spectrometry-Mass spectrometry	87
4.5	Conclusions	91
4.7	References	92
5.	Ions in Flames During Combustion Synthesis	94
5.1	Abstract	95
5.1	Introduction	96
5.2	Experimental Methods	98
5.2.1	Size distribution measurements	99
5.2.2	Neutral fraction particle size distributions	99
5.3	Results and Discussion	102
5.3.1	Naturally charged versus charge conditioned size distributions	102
5.3.2	IV curves for measuring electrical properties in flames	104
5.3.3	Boosted CPC battery for charge fraction measurements of sub 2nm clusters.	108
5.4	Conclusions	109
5.5	References	110
6.	Characterization of Nanostructured Niobium Doped TiO ₂ Thin Films Synthesized in a Flame Aerosol Reactor	112
6.1	Abstract	113
6.2	Introduction	114
6.3	Experimental Methods	116
6.3.1	Flame Aerosol Reactor	116
6.3.2	Chemicals	118
6.3.3	Characterization	118

6.4	Results and Discussion	120
6.4.1	Thin film composition and doping	120
6.4.2	Thin film Conductivity and performance	125
6.5	Conclusion	128
6.6	References	130
7.	Conclusion	132
7.1	Summary	133
7.2	Future steps	135
	Appendix I: Experimental Setup.....	138
	Appendix II: Thermochemical Data	146
	Appendix III: Controlled Studies on Aerosol Formation during Biomass Pyrolysis in a Flat Flame Reactor	149
	Curriculum Vitae.....	180

List of Figures

Figure 1.1: Overview of particle formation mechanisms in a flame aerosol reactor. Cluster and collisional growth mechanisms are outlined in red as an area of significant mechanistic knowledge gap.	5
Figure 1.2: Differential mobility analyzers used in measuring particle size distributions (a) and resulting size distributions measured in a flame aerosol reactor at various heights in a diffusion flame aerosol reactor during the combustion synthesis of TiO ₂	7
Figure 1.3: Principal scheme of MBMS for mass analyzers for flames [26]......	9
Figure 1.4: Transformation reactions of TTIP to TiO ₂ in a Hydrogen flame	11
Figure 1.5: Reduced electrical mobility as a function of atomic mass for various ions ⁵⁴	19
Figure 2.1: (a) Flat flame Aerosol Reactor used for the synthesis of pristine and TiO ₂ /SiO ₂ nanocomposites with a schematic diagram of the initial stages of particle formation during combustion synthesis. Collisional growth mechanisms from stable monomers to clusters (highlighted) have yet to be established. (b) Experimental setup of Half Mini DMA operated under closed loop conditions for measurement of sub 2 nm cluster size distributions.	30
Figure 2.2: Measurements of sub 2 nm cluster size distributions in a blank methane-air flat flame sampled 3.5 mm above the burner head using the Half Mini DMA for positively charged (–) and negatively charged (---) ions.....	35
Figure 2.3: (a) TiO ₂ cluster size distribution measurements at a height of 25 mm above the burner head with a TTIP precursor feed rate of 0.20 mmol/hr for positively charged (–) and negatively charged (---) particles; (b) SiO ₂ cluster size distribution measurements at a height of	

25 mm above the burner head with a TEOS precursor feed rate of 0.25 mmol/hr for positively charged (—) and negatively charged (---) nanoparticles. 37

Figure 2.4: (a) AFM image of TiO₂ clusters for substrate surface topography. (b) The corresponding height profile taken across the white dotted line is given below. (c) The AFM-phase image shows the Si wafer surface as the darker color and the TiO₂ clusters as the lighter color providing evidence of cluster formation. (d) The particle size distribution of over 100 particles is given below the AFM-height image. 38

Figure 2.5: Overall trends of measured TiO₂ cluster number concentrations presented as signal intensity on the y-axis (A.U.) with respect to the TTIP precursor feed rate for positively charged clusters on the x-axis (mmol/hr) measured in a methane-air flat flame reactor at a height of 3.5 mm above the burner head. 39

Figure 2.6: Effect of residence time for (a) positively charged (b) and negatively charged TiO₂ cluster number concentrations represented as signal intensity on the y-axis (A.U.) and height above the burner head (mm) on the x-axis for a fixed precursor feed rate of 0.33 mmol/hr. 40

Figure 2.7: Cluster size distribution measurements 25 mm above the burner head in a flame aerosol reactor comparing the flame synthesis of pristine TiO₂ (---) and TiO₂ doped with SiO₂ (—) at a molar ratio of 3:1. 41

Figure 3.1: Experimental set-up of the flat flame aerosol reactor for measurement of natively charged clusters in an atmospheric-pressure-interface time-of-flight mass spectrometer 55

Figure 3.2: Background ions measured in a flame aerosol reactor for naturally charged positive (left) and negative (right) ions, with nominal masses of major peaks labeled. For negatively

charged flame clusters, larger peaks were scaled at by multiplying the signal intensity by 20 (20X). 58

Figure 3.3: Negative TTIP spectra at two different precursor feed rates of 0.07 mmol/hr (top) and 0.15 mmol/hr (bottom). Colored spectra refer to portions of the mass spectra where Signal intensities were multiplied by 2 (2X), 5 (5X) and 10 (X). 61

Figure 3.4: Positively charged clusters during the combustion synthesis of TiO₂ at three different loading rates 63

Figure 3.5: Mass defect plots for (a) positively charged ions and (b) negatively charged ions during the combustion synthesis of TiO₂. 65

Figure 4.1: Experimental setup for the combustion synthesis of SiO₂ and TiO₂ in a premixed flat flame aerosol reactor along with the measurement of charged clusters using an atmospheric-pressure-inlet time-of-flight (APi-TOF) mass spectrometer. 77

Figure 4.2: Natively charged clusters of measured for SiO₂ nanoparticle formation in a flame aerosol reactor for positively (A) and negatively (B) charged clusters. 82

Figure 4.3: Direct comparison of resulting mass spectra of natively charged clusters for composite TiO₂/SiO₂ (black) and single component SiO₂ (gray) nanoparticle formation in a flame aerosol reactor. 85

Figure 4.4: DMA mobility scans comparing mobility spectra for negatively charged pure SiO₂ (solid) and composite SiO₂/TiO₂ nanoparticle formation 87

Figure 4.5: Negative mass spectra at a fixed electrical mobility for pure SiO₂ nanoparticle synthesis 88

Figure 4.6: Comparison of the mass-mobility relationship for clusters of SiO₂ and composite . 90

Figure 5.1: Experimental setup for measuring natively and charge conditioned particle size distributions..... 100

Figure 5.2: Measurement of IV curves in a flame aerosol reactor under a DC electric field along with measurement with a boosted CPC battery for measurement of sub 2nm cluster size distributions..... 101

Figure 5.3: Comparison of natively charged and neutralized particle size distributions measured in a flame aerosol reactor as during the combustion synthesis of TiO₂..... 103

Figure 5.4: Particle Size distributions for the natively charged fraction (CPR-OFF), and neutral fraction (CPR-ON+ Neutralizer) of particle. The effectiveness of the charged particle remover was confirmed as no particles were measured with the charged particle remover turned on without a neutralizer..... 104

Figure 5.5: Current-voltage characteristics of a methane air flame (A) and a hydrogen flame (B) as measured by a parallel ion collector plate 107

Figure 5.6: IV characteristics (a) and corresponding CPC battery measurements of clusters sampled in a flame aerosol reactor..... 108

Figure 6.1: Schematic diagram of hydrogen fuel flame aerosol reactor used for the synthesis of niobium-doped TiO₂ nanostructured thin films. 119

Figure 6.2: nanostructured morphology of NTO thin films synthesized through combustion synthesis..... 122

Figure 6.3: High resolution XPS spectra for (A) Ti 2p and (B) Nb 3d binding energies. The niobium percentages are labeled on the respective Nb peaks.	124
Figure 6.4: Normalized XRD spectra for NTO thin films synthesized through combustion synthesis.	125
Figure 6.5: Conductivity characterization through measurements of (A) resistivity and (B) Hall mobility for NTO thin films synthesized in a flame aerosol reactor.	127
Figure 6.7: Optical characterization of thin films using (A) transmittance and (B) absorbance measurements for Tauc plots to measure the bandgap shift of thin films	128
Figure I.1: Labview program for the control of the Half Mini DMA for measurement of sub 2m cluster size distributions.	139
Figure I.2: Schematic diagram of flat flame aerosol reactor along with calibration and method of measuring sub 2nm cluster size distributions in a flame aerosol reactor (top). Photograph of half-mini DMA experimental setup (bottom).	140
Figure I.3: Experimental Setup for coupling tandem ion mobility mass spectrometry using an API 2000 quadrupole mass spectrometer for measuring the size resolved chemistry of cluster formation.	141
Figure I.4: Experimental set up of flame aerosol reactor used for synthesis of multicomponent niobium-doped TiO ₂ thin films.	142
Figure I.5: Picture of premixed hydrogen flame aerosol reactor used for the combustion synthesis of niobium-doped TiO ₂ thin films.	143

Figure I.6: Resulting mass spectra at a fixed mobility for positively charged (top) and negatively charged (bottom) ions in a flame aerosol reactor for TiO₂ cluster formation as measured through tandem ion mobility mass spectrometry using an API 2000 quadrupole mass spectrometer to obtain mass spectra.144

Figure I.7: Contour plot of mass spectra measured over a range of mobilities for clusters of TiO₂ as measured using tandem ion mobility mass spectrometry. Increased DMA voltage indicates larger clusters (based on mobility diameter).145

Figure II.1: Experimental setup of the flat flame for measuring particle size distributions with mechanisms of biomass combustion.155

Figure II.2: Thermogravimetric mass % (2a) and DTG (2b) curves comparing applewood(▼), cottonstalk(○), Poplar(△), *Prosopis juliflora*(■), Cherrywood(●), Oak(□) at a constant heating rate of 15 K min⁻¹.....162

Figure II.3: Mass% (3a) and DTG (3b) curves comparing various heating rates for *Prosopis juliflora* for 50 K min⁻¹ (●), 100 K min⁻¹ (○), 200 K min⁻¹(▼), and 400 K min⁻¹ (△).....165

Figure II.4: Devolatilization of applewood particles for oven dry (solid) high moisture (dashed) fuel. Experiments were performed at a heating rate of 200K min⁻¹ (4a) and 400K min⁻¹ (4b)...168

Figure II.5: Measured size distributions for various types of fuel comparing applewood(●), cottonstalk(○), Poplar(▼), *Prosopis juliflora*(△), Cherrywood(■), Oak(□).....170

Figure II.6: Measured size distributions for high moisture applewood(▲), ambient moisture applewood(□), and oven dried applewood(●).....171

List of Tables

Table 2.1: The inverse mobility for TiO ₂ and SiO ₂ clusters determined using 2 methods. The calculated inverse mobility is based on empirical mass-mobility correlations[46] for clusters carrying a unit charge. The equivalent mass diameter was calculated from the measured cluster mobility using the curve fitted Stokes-Millikan relationship[45] and adjusting the particle diameter by subtracting an effective gas molecule diameter of 0.3 nm.	33
Table 2.2: List of experimental parameters for measuring charged clusters. A flat flame aerosol reactor was used for combustion synthesis of pristine and nanocomposite TiO ₂ /SiO ₂ and charged clusters were measured using a Half Mini DMA.	34
Table 3.1: Properties of the methane-air flat flame aerosol reactor	53
Table 3.3: Experimental plan for measuring cluster formation pathways	56
Table 3.4: Proposed molecular compositions for identified peaks in a negative mass spectrum	60
Table 4.1: Premixed flame aerosol reactor parameters and operating conditions	76
Table 4.2: Experimental plan	79
Table 4.3: Identified positive and negative ions measured by an API-TOF mass spectrometer .	84
Table 5.1: Experimental plan for the study of charging and the role of ions during combustion synthesis	98
Table 6.1: Flame parameters for the flame synthesis of NTO thin films.....	117
Table 6.2: Thickness, composition, and performance of nanostructured thin films	123
Table II.1: Enthalpy of formation for TTIP and TEOS intermediates.....	147

Table III.1: Proximate analysis of fuel.....	156
Table III.2: Experimental plan for thermogravimetric analysis.....	157
Table III.3: Shift in peak devolatilization at higher heating rates as seen in Figure III.2.....	166
Table III.4: Key kinetic parameters of devolatilization as measured by TGA (Figure III.2) and modulated TGA	169
Table III.5: Size distribution statistics regarding for measured size distributions	171

Acknowledgements

I am very thankful to Dr. Pratim Biswas for his guidance and support throughout my PhD. Dr. Biswas taught me what it meant to be a successful PhD student and great researcher. Throughout my time in the Aerosol and Air Quality Research Laboratory, Dr. Biswas continually challenged me while always providing me with opportunities and resources to execute and test my ideas. Furthermore Dr. Biswas was always supportive of my efforts outside the lab to further my professional development which really allowed me to gain a broader understanding of the importance of my work and how I can make a lasting impact after my time in AAQRL.

I am grateful to the support of my thesis committee as each committee member contributed to the development of this work. Richard Axelbaum taught me the fundamentals of combustion to help me understand my flame aerosol reactor. Through countless hours of discussion, Parag Banerjee's guidance helped me learn about characterization techniques so that I could understand the materials I was synthesizing in my flame aerosol reactor while providing his lab resources to allow me to perform the characterization of my samples. Brent Williams taught me about high resolution time of flight mass spectrometry and provided insight into how to interpret mass spectra. Palghat Ramachandran guided me on understanding transport phenomena and the kinetics in my system. Finally Dale Powers and Subramanya Herle provided insight from their experience in industry to help guide my direction of research.

My fellow AAQRL colleagues provided the rich academic environment for constant discussions on our work. I would particularly like to thank Yang Wang, Tandeep Chadha, Yi Jiang Sameer Patel, Anna Leavey, Nathan Reed, and Ramesh Raliya for their help and support in

characterization and collaboration on my projects. I would also like to thank other past and present lab members for the opportunity to learn from their work and for their help in providing constructive feedback and for making the lab a wonderful place to work.

I would like to thank my friends in the Energy Environmental and Chemical Engineering department who really made the difficult path of pursuing a PhD as enjoyable as possible. In no particular order I would like to thank Matthew Lawder, William Bricker, Jessica Ray, Paul Northrop, Craig Jacobson, Chelsea Niel, along with all the other members of Non-Ideal Behavior. Most of all, I would like to thank Amelia Nguyen's understanding and encouragement through my PhD.

I would like to acknowledge my funding sources which granted me the opportunity to perform this research. This includes the Olin W. & LaVerne C. Kriege Fellowship, the Photosynthetic Antennae Research Center, and Consortium for Clean Coal Utilization, and Solar Energy Research Institute for India and the US. I would also like to thank the staff in the EECE department, including Rose Baxter, Trisha Sutton, Beth Mehringer, and Christine Tilley, as they were instrumental in helping me with navigating the administrative aspects of my PhD.

Finally, I would especially like to thank my family for their unwavering support, more specifically my parents Rixun Fang and Shijin Wang, who always did whatever they could to encourage my pursuit of a PhD. They always taught me to be resilient, to never to give up, and to never settle. Without my parents, I would not have been able to complete my PhD

Jiaxi Fang

...dedicated to my parents and family

ABSTRACT OF THE DISSERTATION

Nanoparticle Formation in the Flame Synthesis of Multicomponent Nanostructured Materials for
Clean Energy Applications

by

Jiayi Fang

Doctor of Philosophy in Energy Environmental and Chemical Engineering

Washington University in St. Louis, 2016

Professor Pratim Biswas, Chair

This dissertation studies the initial stages of particle formation during the combustion synthesis of multicomponent nanomaterials. Combustion is commonly used for the production of nanomaterials at industrial scales and has advantages of high production rates, low waste generation, and scalability. However, there are limitations in being able to apply this synthesis approach to more advanced multicomponent systems. Gas to particle conversion in flames occurs through precursor decomposition, collisional growth, coagulation, condensation, and sintering. There is a fundamental gap in knowledge on the initial stages of particle formation in flames below 2nm due to measurement difficulties and instrumentation limitations. Using a high resolution differential mobility analyzer, the first mobility spectrum measurements of sub 2nm clusters were presented for single component TiO_2 and multicomponent $\text{SiO}_2/\text{TiO}_2$ synthesis demonstrating the importance of discrete clusters during particle growth.

Further insight into the nature of sub 2nm clusters were gained through the utilization of an atmospheric-pressure time-of-flight mass spectrometer to measure the chemical composition of

sub 2nm clusters. During the combustion synthesis of TiO_2 , it was revealed that for negatively charged species, chemical ionization plays an important role in the formation of TiO_2 clusters while large concentrations of high molecular weight organometallic Ti clusters could be measured. Using similar approaches for silica, intermediates of silica clusters could be identified. The main Si growth pathway was revealed to be through silicic acid clusters, where dehydration, hydrogen abstraction, and hydroxyl radical interactions persist through larger clusters of Si. With multicomponent systems of TiO_2 and SiO_2 , evidence of mixed oxide cluster growth could be seen along with independent cluster growth. Mass mobility plots from tandem ion mobility spectrometry-mass spectrometry further revealed that metal oxide cluster masses were much larger than predicted by the widely utilized Kilpatrick relationship used for mass-mobility correlations.

The role of ions during combustion synthesis was further studied through measurements of natively charged, charge conditioned, and neutral particle size distributions. Using current voltage measurements in an electric field, the concentration of ions and electric properties of flames were also used to provide insight into ion properties during combustion synthesis for TiO_2 and SiO_2 .

Finally, insight from previous studies on the mechanisms of particle formation were applied in developing a system for the synthesis of niobium doped TiO_2 nanostructured thin films towards transparent conducting oxide applications. Using a flame aerosol reactor, highly conductive and transparent thin films could be synthesized while enhanced conductivity was achieved through controlled-niobium doping into the anatase crystal lattice of TiO_2 . Findings from this dissertation have revealed the complexity of gas to particle conversion mechanisms in the initial stages and are the first step towards developing the ability to design flame aerosol reactors for advanced materials synthesis.

1. Introduction

1.1 Overview

As nanomaterials become more prevalent in applications such as sensors, clean energy, and medicine, the ability to manufacture advanced nanomaterials in a scalable, cost effective manner is limited by the ability to apply these approaches at commercially relevant scales. Aerosol synthesis techniques can be a scalable, cost effective method of manufacturing nanomaterials in large quantities but suffer from process design limitations due to a lack of fundamental knowledge regarding the initial stages of particle growth [1]. For example, the chloride process is commonly used for the production of TiO_2 nanoparticles, but a lack in understanding on the particle growth mechanisms limits the optimization of this process. Industrial flame aerosol reactors are mostly designed and developed through empirical approaches limiting their applicability to more complex systems and advanced materials. Factors such as the precursor type, flame chemistry, flow structure, and quenching all can have dramatic effects on the resulting particle size, morphology, and structure. Complexities in these areas are compounded with multicomponent systems making tailored nanomaterials even more difficult to synthesize at industrial quantities. The Long term success of combustion synthesis as an industrial technique will rely upon the ability to develop these processes for more advanced materials based on first principle approaches instead of empirical approaches [2].

1.2 Motivation

Nanotechnology as grown from a technology focused on discovery, to a technology now focused on commercialization and innovation as the nanotechnology industry is projected to reach \$75.8 Billion by 2020. In 2015, sales of nanomaterials alone grew from \$1.6 billion to \$2.1

billion [3]. Nanomaterials also have common features which make it applicable in a wide array of markets and materials with implementation in metal polymer alloys, fiber composites, coatings, polymers, catalysts and photovoltaics. These materials are consequently used in target applications such as cosmetics to cars to consumer electronics. As the demand for nanomaterials increases, more scalable, cost effective, and sustainable techniques for manufacturing will be required. This is further reflected in the National Nanotechnology Initiative (NNI) which proposes a 2016 budget of \$1.5 billion for federal agencies with investments in nanotechnology R&D. Most notable is the fact that several NNI participating agencies such as the DOE, NIH, and FDA are requesting significant increases in their 2016 nanotechnology investments [4]. Thus, as new technologies emerge from lab scale research, translation of this technology to commercial scales will require cost effective synthesis techniques.

Many techniques exist for gas phase nanoparticles synthesis but none has been utilized with more success than flame aerosol reactors as it has become a multibillion dollar U.S. business [5]. Different types of combustion systems can also be designed to accommodate different precursor delivery methods, flame chemistry, and production rates [6]. These include premixed flame aerosol reactors [7], diffusion flame aerosol reactors[8], and flame spray pyrolysis [9]. Advantages in flame aerosol reactors include being a single step process with no moving parts, scalability, low waste generation, and rapid rates of production. Limitations include difficulties in controlling particle morphology, composition, and accurate predictive capabilities. Currently applications of flame aerosol reactors include the synthesis of titania, aluminum oxides, fumed silica, and carbon black. Recent advances in flame aerosol reactors have allowed for the ability to functionalize nanoparticles and coat them. The ability to make

more complex nanoparticles has been demonstrated however proper control over composition and morphology still remains a critical issue.

1.3 Background on combustion synthesis

Combustion synthesis is a self-propagating high temperature synthesis process by which nanomaterials are manufactured through gas-particle conversions. Using a flame aerosol reactor (FLAR), gas phase synthesis can be performed to yield nanomaterials by utilizing gaseous precursors which are added to a flame. High temperature reactions and aerosol growth processes take place in the flame zone to convert precursors into stable the intended nanomaterial product. Particle formation mechanisms and pathways can be described as precursor decomposition [1], coagulation, condensation [10], nucleation [11], and sintering [12]. Figure 1.1 provides an overview of the pathways towards particle formation in a flame aerosol reactor. Among each of these steps, the formation of stable clusters below 2nm has been neglected due to difficulties in measurement, thus there is a significant knowledge gap on the mechanisms of the initial stages of particle formation.

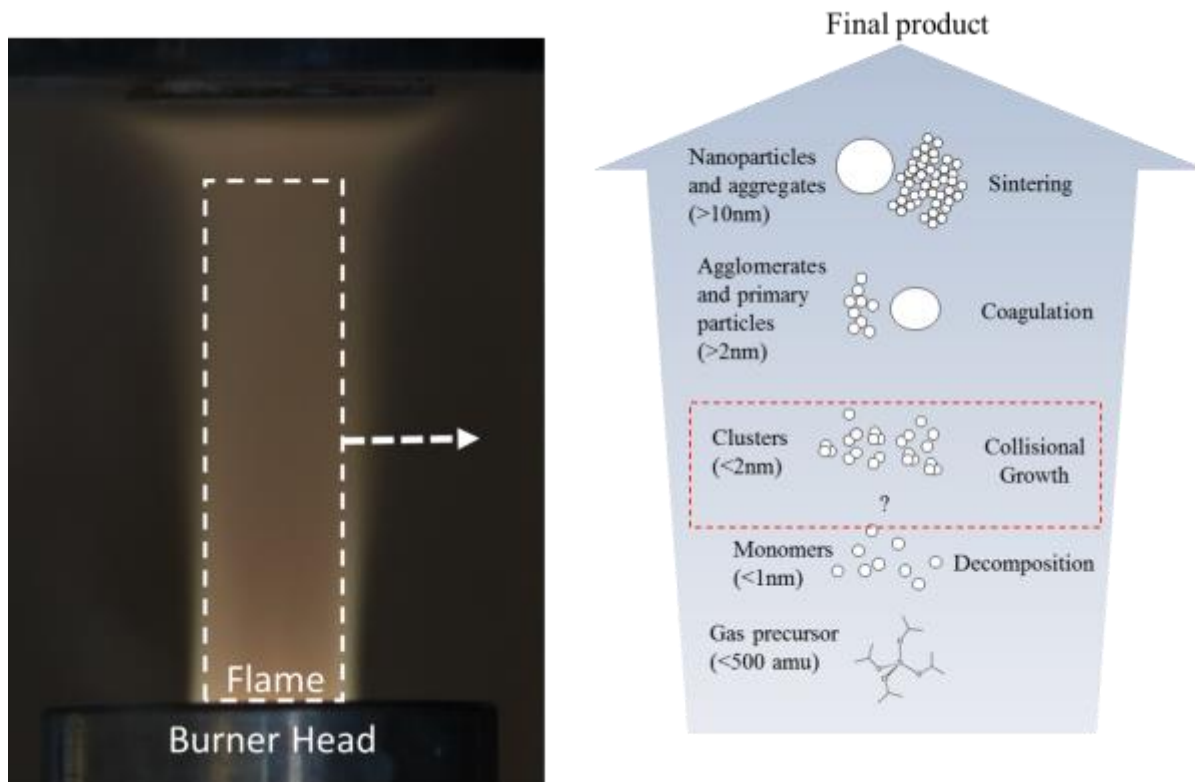


Figure 1.1: Overview of particle formation mechanisms in a flame aerosol reactor. Cluster and collisional growth mechanisms are outlined in red as an area of significant mechanistic knowledge gap.

Attempts to model aerosol growth processes must rely on a mechanistic understanding of how these particles form. Particle growth processes above 2nm such as coagulation, condensation, and sintering, mostly due to the ability to measure these processes in detail with established measurement techniques. The steps for particle growth are described below:

1. **Decomposition:** gaseous precursors such as titanium(IV) isopropoxide are converted to monomers through various chemical pathways such as decomposition, oxidation, and hydrolysis[13].

2. **Collisional growth:** monomer products from precursor decomposition undergo molecular coagulation due to Brownian motion (typically in the free molecular regime) to grow into stable clusters and primary particles [14, 15].
3. **Nucleation:** Particle birth due to thermodynamically favorable conditions from supersaturated vapor concentrations [16].
4. **Condensation and surface growth:** attachment of vapor phase molecules onto the surface of larger particles [17].
5. **Coagulation:** aggregation through collisional growth due to Brownian motion in the continuum regime [18].
6. **Sintering:** coalescence of aggregates through solid state diffusion or viscous flow towards the reduction of surface area [19].

1.4 Measurements of particle growth in flame aerosol reactors

Here we present an overview of real-time measurement techniques for particle growth in flame aerosol reactors. A majority of studies on particle formation during combustion synthesis relies on electrical mobility measurements ranging from 10-400 nm using differential mobility analyzers (DMA). Commercially available scanning mobility particle sizers (SMPS) provide the ability to measure size distributions in real time using electrostatic classification and particle counting (Figure 1.2, [20]). These methods are well established and are the most common means of measuring size distributions.

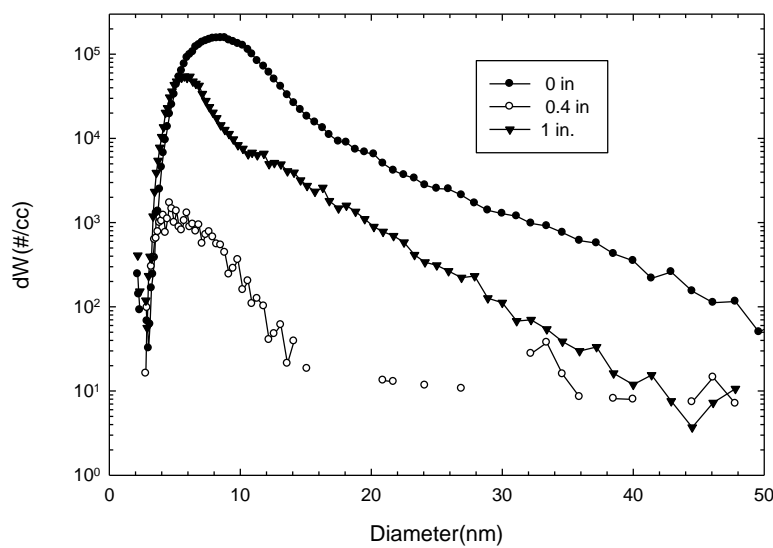


Figure 1.2: A resulting size distributions measured in a flame aerosol reactor at various heights in a diffusion flame aerosol reactor during the combustion synthesis of TiO₂ using a nano DMA

Optical approaches have also been utilized commonly for in situ diagnostic measurements of particle formation in flames. This includes laser induced incandescence (LII) [21], laser induced breakdown spectroscopy (LIBS) [22], and laser induced fluorescence (LIF) [23], and light scattering measurements [12]. Each of these techniques have been applied to a variety of aerosols to study mechanisms of particle formation, for example, Yang and Biswas [12] used light scattering to study the sintering of titania nanoparticles in premixed flames. Advantages of these techniques revolve around the ability to measure characteristics in the flame without significant intrusion or external influence on the flame. Furthermore these techniques have been successfully extended towards mixed systems, for example, Mcmillan et al. [24] used LIF to study multicomponent particle nucleation mechanisms with the vapor phase growth of iron oxide-silica nanocomposites. Light based approaches however are not suitable for studies below a certain size range (~5-10 nm) due to limitations in signal intensity and detection limits.

1.5 Flame chemistry measurements

Some of the earliest studies on combustion have utilized mass spectrometric techniques to answer questions regarding flame chemistry [25]. Detailed reviews regarding ion measurements in flames have mainly focused on flame chemistry, flame structure, ionization mechanisms, and soot formation mechanisms [26, 27]. Despite over 30 years of research, a detailed understanding of soot formation, and overall particle formation at the initial stages is lacking. Such measurements are based off of molecular beam mass spectrometry (MBMS) due to their high sensitivity and ability to detect single molecules and radicals. Briefly, a flame MBMS consists of a sampling probe, skimmer, and a detection system (Figure 1.3, [26]). Sampling probes are designed to minimize perturbations in the flame while extracting flame gases with a rapid expansion to reach collision-less free molecular flow thus preventing further chemical reactions. A molecular beam is created through a multistage expansion where the 1st and 2nd stage is pumped to a pressure of 10^{-4} and 10^{-6} Torr respectively. After the molecular beam enters the 2nd stage expansion through a skimmer, ionization of gas molecules takes place through either electron or photoionization. The subsequent ion masses are measured with a quadrupole mass spectrometer in the final stage. Perpendicularly with a flame, where the distance between the burner head and sampling probe can be modulated [27].

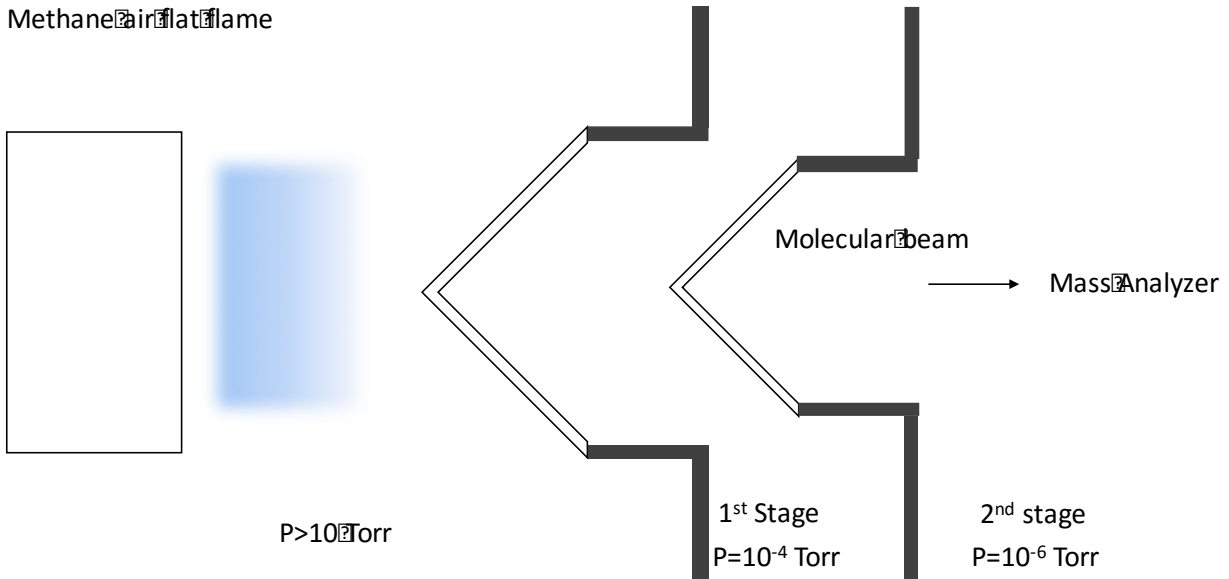


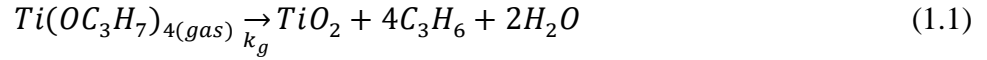
Figure 1.3: Principal scheme of MBMS for mass analyzers for flames [26].

This technique has been applied to understanding the chemical pathways of TiO_2 formation in a hydrogen flame [28] and TEOS decomposition kinetics [29]. Both studies have revealed more detailed chemical pathways of precursor decomposition, but have been unable to address the resulting particle growth mechanisms. Such precursor decomposition kinetics are addressed in the following:

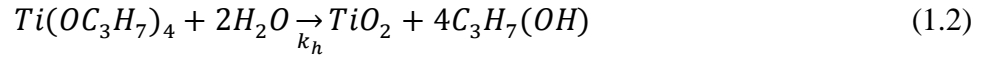
1.6 Precursor decomposition pathways:

Simplifications on the reaction mechanisms for organometallic precursor decomposition has assumed single step reactions based on 1st or 2nd order reactions. The kinetics and chemistry of precursor oxidation and decomposition for the synthesis of TiO_2 [30] from TTIP has assumed three main pathways:

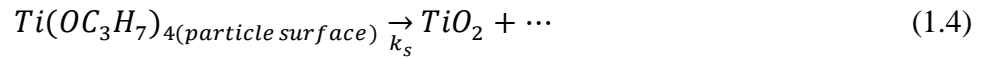
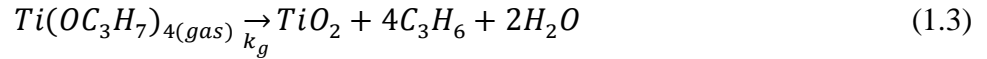
- I. Gas phase thermolysis for TTIP [31] :



II. Gas phase hydrolysis [32]:



III. Gas phase and surface thermal decomposition of TTIP is predicted as follows [33]:



Where the overall kinetics of decomposition are $k_{TiO_2} = k_g + k_s A \rho_g$. The actual surface kinetics of TTIP decomposition are highly dependent on experimental conditions. For flame synthesis, hydrolysis reactions (case II) are near instantaneous when compared to pure thermal decomposition and is the dominant method of TTIP decomposition. Shmakov et al. [28] performed the most detailed study in this regard for hydrogen flames and was able identify a more detailed reaction scheme (Figure 1.4). Based on newly measured experimental data, a newly proposed bimolecular rate constant was also proposed to be $k = 2 \times 10^{12} \exp((-12.2 \text{ kcal/mol})/RT) \text{ mol}^{-1}\text{s}^{-1}$.

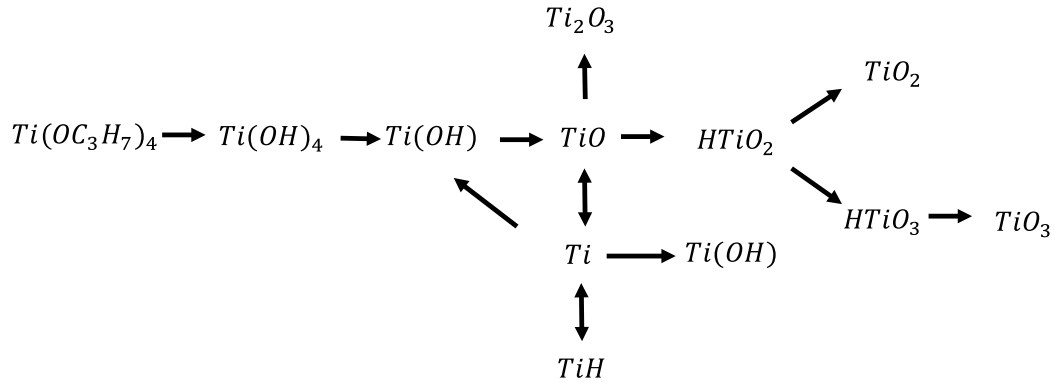
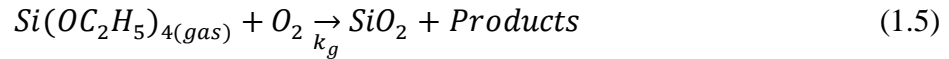
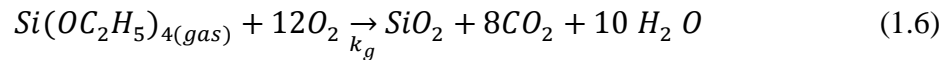


Figure 1.4: Transformation reactions of TTIP to TiO₂ in a Hydrogen flame [28].

Similar studies for TEOS decomposition have been performed. For TEOS decomposition, kinetic models have been based on the simplified pathways:



Where measurements have yielded kinetic rate constants of $k_g = 3.4 \times 10^{11} \exp(-1304 \text{ K/T}) \text{ cm}^{-1}$. In the case of a diffusion flame [34], characteristics of silica generation from TEOS was measured for various flame conditions based on the following mechanism:



More recently, comprehensive models have been generated through tracking elemental fluxes and sensitivity analyses [35]. Challenges still remain for applying such models to flame systems where hydrolysis reactions and other decomposition mechanisms may take place.

1.7 Charging in flames

One of the most important aspects of studying the initial stages of particle formation is the ability to charge aerosols below 2nm. In conventional studies using particle size distributions, a size dependent, steady state charge fraction is assumed for proper data inversion. Such charge fractions are believed to be generated through ion particle collisions from bipolar ions generated either through a charge conditioner such as a radioactive neutralizer. However such assumptions may not be appropriate for combustion synthesis due to the transient nature of flames. As particles nucleate in flames, the high concentrations of ions, rapidly evolving kinetics of precursor decomposition, and high temperature can result in different charging mechanisms as seen in conventional systems.

The main mechanisms of charging include diffusion charging, photoionization, thermoionization, and chemi-ionization [36]. The earliest calculation of charge distributions were based on either the Boltzmann distribution [37, 38], or the Fuchs theory of charging[39]. The Boltzmann charge distribution is presented as a function of the particle diameter (d_p), number of elementary charges (p) and temperature (T):

$$f(p, d_p) = \frac{2e}{\sqrt{\pi d_p k T}} \exp\left[-\frac{pe^2}{d_p k T}\right] \quad (1.7)$$

where $f(p, d_p)$ is the size dependent charge fraction, e is the charge of a single electron, and k is the Boltzmann factor.

The Wiedensholer approximation, which is based on the Fuchs theory of charging, is the most widely used method for data inversion in particle size distribution measurements [40].

However these approximations require fixed input parameters for the ion mobility and mass for positive ions and negative ions which may change with regards to the system. Significant correction factors and improvements on Fuchs theory have further been proposed with improved accuracies [41-43], while recent measurements comparing different aerosol diffusion chargers and revealed differences in charge fractions ranging from 4% up to 18% [44]. Up to this point it is clear that particle charging in the free molecular and transition regime is highly system specific while any data for charge fractions below 2nm is lacking. To this date, there has yet to be a consensus on the correct mechanisms of particle charging below 10 nm.

1.8 Sub 2nm cluster classification and mobility

Electrostatic classification relies on the ability to add a known charge on an aerosol to measure the drag force in a known electric field [45]. A balance between the drag force and the electrical mobility yields the electrical mobility equivalent diameter which can be calculated based on mobility-size relations, commonly referred to as the Stokes-Millikan equation. Below 2nm however, this relationship no longer holds as the cluster charge and shape can affect particle interactions with the background gas molecules thus altering the drag force estimations. In the continuum regime the drag force is well established to exhibit hard sphere elastic scattering. As the cluster size transitions to the free molecular limit ($Kn \gg 1$), two main effects will alter the drag force[46]. First, the transition from diffuse scattering to elastic-specular collisions will cause an increase in mobility. Second, polarization effects with neutral gas molecules decrease the mobility as particle size decreases. The inability in using Stokes-Millikan below 2nm arises from the size dependence complexities of these two effects.

A common method of estimation for particle diameter is through bulk physical parameters, the particle diameter based on its mass (m_p) can be estimated from the bulk density assuming a spherical morphology:

$$d_m = \sqrt[3]{\frac{6m_p}{\pi\rho}} \quad (1.8)$$

where m_p is the particle mass and ρ is the bulk density. Equation 1.8 is commonly used to calculate monomer size, for example TiO_2 monomers would have a mass diameter of 0.4nm. However, experimental mass mobility measurements often yield different mobility diameters. Evidently, macroscopic parameters such as the bulk density ρ may not be accurate in the sub 2nm regime due to changes in the lattice constant and void fractions [47]. In the free molecular limit, where the particle size is similar to that of the background gas molecule, further definitions such as the collision cross section and Van der Waals radius can be used to define the particle diameter. Below 2nm, the physical particle size is difficult to measure as an assumption of a spherical morphology may no longer hold, thus this work will focus primarily on equivalent mobility diameter. Particle size determination based on electrical mobility is commonly utilized since the electrical mobility is a measureable quantity for real time particle size detection.

Mobility of clusters and ions

A brief overview regarding the mobility of clusters and ions below 2nm will be given in the following section. The mobility (Z) is a measureable parameter and is most commonly defined with respect to a particle size where $Z=F(d_p)$. The mobility diameter is often determined through an inverse function $d=F^{-1}(Z)$. Mechanical mobility (B) and electrical mobility are

interchangeable by the relation $Z_p = qB$ where q is the particle charge and Z_p is the electrical mobility. Depending on the size of the particle in relation to the gas particle diameter, particle transport can be classified based upon the Knudsen number which is defined as $2\lambda/(d_p+d_g)$ where λ is the mean free path of air. Three main classifications are the free molecule (kinetic) regime ($Kn \gg 1$), transition regime ($Kn \sim 0.1-10$), and continuum regime ($Kn \ll 1$). In the continuum regime, the mobility can be expressed as the classical Stokes Millikan equation:

$$Z = \frac{qC}{3\pi\mu d_p} \quad (1.9a)$$

where $q=ze$ represents the particle charge. C is the Cunningham slip correction factor and can be represented in the general form:

$$C = 1 + Kn(a + be^{-c/Kn}) \quad (1.9b)$$

Where a , b , and c are constants determined through interpolation for limiting forms of Z . For macroscopic particles in the continuum regime, C is effectively unity beyond a certain size range. For particles in the transition and free molecular regime, values of a , b and c have been proposed as 1.257, 0.4, and 1.1 respectively although different values have been reported depending on the authors [48-50].

Equation 1.9 is primarily empirical and experience many issues below 2nm as the particle size approaches the free molecular limit. Equation 1.9 is unable to take into account the finite diameter of a gas molecule (d_g) and cannot take into account polarization effects. Furthermore collisions between the particle and gas molecules transition from inelastic to elastic. In the free

molecular regime ($Kn \ll 1$), more fundamental expressions have been derived for hard sphere collisions using Chapman-Enskog theory using the kinetic theory of gases.

$$Z_{FM} = \frac{3(2\pi)^{-1/2} q(kT/m_g)^{1/2}}{2(1+\alpha\pi/8) p(d_m+d_g)^2} \quad (1.10a)$$

Where k is the Boltzmann constant, m_g is the mass of the background gas, and p is the pressure α is the accommodation coefficient, and T is the temperature. A modified form of equation 1.10a can also be used to relate the collision cross section (Ω) and mobility:

$$Z_{FM} = \frac{3}{16} \frac{ze(2\pi kT/m_g)^{1/2}}{p} \left(1 + \frac{m_g}{m}\right)^{1/2} \frac{1}{\Omega} \quad (1.10b)$$

In the free molecular limit, simple expressions assuming geometrical cross sections for Ω can be used.

As the particle is much larger than atomic dimensions yet much smaller than the gas mean free path, λ , an accommodation coefficient must be introduced to account for the fact that gas molecule collisions will begin to exhibit diffuse scattering. In the free molecular regime where collisions are elastic, α is assumed to be unity. The accommodation coefficient represents the fraction of the gas molecules that scatter diffusely, thus when the particle diameter is beyond the free molecular limit but still significantly lower than the gas mean free path, a value 0.441 is calculated from $3(2\pi)^{-1/2}/2(1+\alpha\pi/8)$ by taking α to be 0.91. The resulting expression from equation 1.3 below 2nm becomes [47, 51]:

$$Z = 0.441 \frac{q(kT/m_g)^{1/2}}{p d_p^2} \quad (1.10c)$$

Recent *ab initio* approaches have further confirmed the value of α demonstrating that approximately 91% of collisions between gas molecules and particles are diffuse while the other 9% are specular [52].

The above expressions have limitations being unable to account for polarization effects and the finite mass of gas molecules. An improved expression for particle mobility with was generated by Tammet by combining the Millikan Fuchs formula with Langevin type dependency for the particle mobility Z_p [48]:

$$Z_p = f_1 f_2 \frac{1 + \frac{\lambda}{\delta} [a + b e^{-c \frac{\delta}{\lambda}}]}{6\pi\eta\delta} \quad (1.11a)$$

$$f_1 = \sqrt{1 + \frac{m_g}{m_p}} \quad (1.11b)$$

$$f_2 = \frac{2.25}{(a+b)(\Omega_{\infty-4}^{(1.1)*} + s_1 - 1)} \quad (1.11c)$$

The factor f_1 takes into account for mass dependency of the Langevin type which depend on the mass of the gas molecule (m_g) and particle mass (m_p). The factor f_2 takes into account inelastic collisions with polarization interaction and depends on slip factor coefficients a , b , and s_1 . the collision integral is $\Omega_{\infty-4}^{(1.1)*}$. From equation 1.11, [48] demonstrated that below 1.4nm, particles can be considered clusters or molecules while equation 1.5 fits well in the range of 0.6-1.4nm. Equation 1.11 is the first attempt to capture the transition from stable clusters to molecular states however this equation has only been examined in detail for one type of aerosol and has not been verified experimentally in great detail for various other aerosol types.

In recent DMA-Mass spectrometry studies, a hybrid approach has been taken to account for the finite diameter of a gas molecule [53]. The mobility based particle diameter can be calculated by measuring the electrical mobility $Z(d_p)$ and is calculated using the Stokes-Millikan law:

$$\frac{Z_p}{\sqrt{1+m_g/m_p}} = Z_p^* = \left[\frac{3\pi\mu}{qe} \frac{(d_m+d_g)}{1+Kn(1.257+0.4exp(-1.1/Kn))} \right] \quad (1.12)$$

Where q is the cluster charge, d_m and d_g are the mass diameter and respectively. The factor $(1+m_g/m_p)^{-1/2}$ is introduced to account for the mass of two body collisions. Equation 1.12 has been utilized for tandem mass spectrometry studies of sub 3nm ionic clusters and have found that for singly charged clusters of 7-41 ion pairs, there is an excellent agreement when the volume diameter is increased by 0.3 nm while for smaller ion pairs, ion dipole interactions cause deviation up to 14.3% [47]. It should be noted that equation 1.5 and 1.2 are the same except for the addition of the correction factor $(1+m_g/m_p)^{1/2}$ and augmented particle diameter $d_p=d_m+d_g$. Although equation 1.12 has been demonstrated to be surprisingly accurate, discrepancies still exist since it ignores polarization effects. Equation 1.12 remains a good approximation but cannot be used to infer cluster structure. Much work remains for a truly accurate prediction of sub 2nm cluster mobility. A more precise numerical expression along with further experimental validation is required.

Up to this point, experimental validation of sub 2nm relationships has been done only for limited types of aerosols such as organic molecules, liquid ionic nanodrops, and atmospheric ions. The most recent measurements have revealed that mass mobility relationships in this regime is system specific and material dependent [54].

1.9 Approach

The goal of this thesis is to study and elucidate the mechanisms of the initial stages of particle formation during the combustion synthesis of nanomaterials through three perspectives:

- 1) Measurement of cluster formation mechanisms in flame aerosol reactors
- 2) The role of ions and charging during the measurement of cluster formation during combustion synthesis
- 3) Applications of combustion synthesis towards doped nanostructured thin films for transparent conducting oxide applications

The next 5 chapters of this dissertation will focus on the initial stages of particle formation the context of these perspectives beginning with the ability to measure sub 2nm clusters in flame aerosol reactors using high resolution differential mobility analyzers (Chapter 2). Insight from these initial measurements are then further extended towards more detailed measurements for the size resolved chemistry of particle formation below 2nm using tandem ion mobility mass spectrometry both for single component (Chapter 3) and multicomponent cluster formation mechanisms (Chapter 4). Since a flame can essentially be described as a high temperature flowing plasma, the role of ions both during measurement and during particle formation for flame aerosol reactors is studied (Chapter 5). Knowledge from previous sections will be applied towards the synthesis of niobium doped TiO₂ thin films for TCO applications (Chapter 6). Finally the Appendix presents further details on the experimental setups used and data that was not included in the previous chapters (Appendix I), an additional first author publication on particle formation from biomass pyrolysis (Appendix II), and a curriculum vitae (Appendix III).

1.10 References

- [1] M. Mehta, Y. Sung, V. Raman, R.O. Fox, Multiscale Modeling of TiO₂ Nanoparticle Production in Flame Reactors: Effect of Chemical Mechanism, *Industrial & Engineering Chemistry Research*, 49 (2010) 10663-10673.
- [2] B. Buesser, S.E. Pratsinis, Design of nanomaterial synthesis by aerosol processes, *Annual review of chemical and biomolecular engineering*, 3 (2012) 103.
- [3] T. Matich, Nanotechnology Future Outlook 2016, in: *Investing news*, 2015.
- [4] T. Kalil, The National Nanotechnology Initiative: Supplement to the President's 2016 Budget, in: E. Subcommittee on Nanoscale Science, and Technology (Ed.), 2016.
- [5] R. Strobel, S.E. Pratsinis, Flame aerosol synthesis of smart nanostructured materials, *Journal of Materials Chemistry*, 17 (2007) 4743-4756.
- [6] D.E. Rosner, Flame Synthesis of Valuable Nanoparticles: Recent Progress/Current Needs in Areas of Rate Laws, Population Dynamics, and Characterization, *Industrial & Engineering Chemistry Research*, 44 (2005) 6045-6055.
- [7] E. Thimsen, P. Biswas, Nanostructured photoactive films synthesized by a flame aerosol reactor, *AIChE journal*, 53 (2007) 1727-1735.
- [8] K. Wegner, S.E. Pratsinis, Scale-up of nanoparticle synthesis in diffusion flame reactors, *Chemical Engineering Science*, 58 (2003) 4581-4589.
- [9] L. Mädler, H. Kammler, R. Mueller, S. Pratsinis, Controlled synthesis of nanostructured particles by flame spray pyrolysis, *J. Aerosol. Sci.*, 33 (2002) 369-389.
- [10] W. Widiyastuti, A. Purwanto, W.N. Wang, F. Iskandar, H. Setyawan, K. Okuyama, Nanoparticle formation through solid-fed flame synthesis: Experiment and modeling, *AIChE journal*, 55 (2009) 885-895.
- [11] G.D. Ulrich, Theory of particle formation and growth in oxide synthesis flames, *Combustion Science and Technology*, 4 (1971) 47-57.
- [12] G. Yang, P. Biswas, Study of the sintering of nanosized titania agglomerates in flames using in situ light scattering measurements, *Aerosol Sci. Technol.*, 27 (1997) 507-521.
- [13] A. Shmakov, O. Korobeinichev, D. Knyazkov, A. Paletsky, R. Maksutov, I. Gerasimov, T. Bolshova, V. Kiselev, N. Gritsan, Combustion chemistry of Ti (OC₃H₇)₄ in premixed flat burner-stabilized H₂/O₂/Ar flame at 1atm, *Proceedings of the Combustion Institute*, 34 (2013) 1143-1149.

- [14] J.X. Fang, Y. Wang, M. Attoui, T.S. Chadha, J.R. Ray, W.N. Wang, Y.S. Jun, P. Biswas, Measurement of Sub-2 nm Clusters of Pristine and Composite Metal Oxides during Nanomaterial Synthesis in Flame Aerosol Reactors, *Anal. Chem.*, 86 (2014) 7523-7529.
- [15] A. D'Alessio, A.C. Barone, R. Cau, A. D'Anna, P. Minutolo, Surface deposition and coagulation efficiency of combustion generated nanoparticles in the size range from 1 to 10 nm, *Proceedings of the Combustion Institute*, 30 (2005) 2595-2603.
- [16] Y. Sung, V. Raman, R.O. Fox, Large-eddy-simulation-based multiscale modeling of TiO₂ nanoparticle synthesis in a turbulent flame reactor using detailed nucleation chemistry, *Chemical Engineering Science*, 66 (2011) 4370-4381.
- [17] P.T. Spicer, O. Chaoul, S. Tsantilis, S.E. Pratsinis, Titania formation by TiCl₄ gas phase oxidation, surface growth and coagulation, *J. Aerosol. Sci.*, 33 (2002) 17-34.
- [18] D.E. Rosner, J.J. Pyykönen, Bivariate moment simulation of coagulating and sintering nanoparticles in flames, *AIChE journal*, 48 (2002) 476-491.
- [19] K. Cho, P. Biswas, Sintering rates for pristine and doped titanium dioxide determined using a tandem differential mobility analyzer system, *Aerosol Sci. Technol.*, 40 (2006) 309-319.
- [20] S.C. Wang, R.C. Flagan, Scanning electrical mobility spectrometer, *Aerosol Sci. Technol.*, 13 (1990) 230-240.
- [21] D. Hebert, A. Coppalle, M. Talbaut, 2D soot concentration and burning rate of a vertical PMMA slab using Laser-Induced Incandescence, *Proceedings of the Combustion Institute*, 34 (2013) 2575-2582.
- [22] Y. Zhang, S. Li, Y. Ren, Q. Yao, S.D. Tse, A new diagnostic for volume fraction measurement of metal-oxide nanoparticles in flames using phase-selective laser-induced breakdown spectroscopy, *Proceedings of the Combustion Institute*, 35 (2015) 3681-3688.
- [23] B.K. McMillin, P. Biswas, M.R. Zachariah, In situ characterization of vapor phase growth of iron oxide-silica nanocomposites: Part I. 2-D planar laser-induced fluorescence and Mie imaging, *Journal of Materials Research*, 11 (1996) 1552-1561.
- [24] B.K. McMillin, P. Biswas, M.R. Zachariah, In situ characterization of vapor phase growth of iron oxide-silica nanocomposites .1. 2-D planar laser-induced fluorescence and Mie imaging, *Journal of Materials Research*, 11 (1996) 1552-1561.
- [25] J.C. Biordi, C.P. Lazzara, J.F. Papp, Investigation of chemical flame inhibition by molecular-beam mass-spectrometry, *Abstr. Pap. Am. Chem. Soc.*, (1973) 53-53.

- [26] A.B. Fialkov, Investigations on ions in flames, *Progress in Energy and Combustion Science*, 23 (1997) 399-528.
- [27] N. Hansen, T.A. Cool, P.R. Westmoreland, K. Kohse-Höinghaus, Recent contributions of flame-sampling molecular-beam mass spectrometry to a fundamental understanding of combustion chemistry, *Progress in Energy and Combustion Science*, 35 (2009) 168-191.
- [28] A.G. Shmakov, O.P. Korobeinichev, D.A. Knyazkov, A.A. Paletsky, R.A. Maksutov, I.E. Gerasimov, T.A. Bolshova, V.G. Kiselev, N.P. Gritsan, Combustion chemistry of $\text{Ti}(\text{OC}_3\text{H}_7)_4$ in premixed flat burner-stabilized $\text{H}_2/\text{O}_2/\text{Ar}$ flame at 1 atm, *Proceedings of the Combustion Institute*, 34 (2013) 1143-1149.
- [29] O. Sanogo, M. Zachariah, Kinetic studies of the reaction of tetraethoxysilane with oxygen atoms, *Journal of The Electrochemical Society*, 144 (1997) 2919-2923.
- [30] A.G. Shmakov, O.P. Korobeinichev, D.A. Knyazkov, A.A. Paletsky, R.A. Maksutov, I.E. Gerasimov, T.A. Bolshova, V.G. Kiselev, N.P. Gritsan, Combustion chemistry of $\text{Ti}(\text{OC}_3\text{H}_7)_4$ in premixed flat burner-stabilized $\text{H}_2/\text{O}_2/\text{Ar}$ flame at 1 atm, *Proceedings of the Combustion Institute*, 34 (2013) 1143-1149.
- [31] K. Okuyama, J.-T. Jeung, Y. Kousaka, H.V. Nguyen, J.J. Wu, R.C. Flagan, Experimental control of ultrafine TiO_2 particle generation from thermal decomposition of titanium tetraisopropoxide vapor, *Chemical Engineering Science*, 44 (1989) 1369-1375.
- [32] F. Kirkbir, H. Komiyama, Effects of Temperature and Reactant Concentration on Properties of Fine TiO_2 Particles Prepared by Vapor-Phase Hydrolysis of Titanium Tetraisopropoxide, in: *MRS Proceedings*, Cambridge Univ Press, 1988, pp. 263.
- [33] S. Tsantilis, H. Kammler, S. Pratsinis, Population balance modeling of flame synthesis of titania nanoparticles, *Chemical Engineering Science*, 57 (2002) 2139-2156.
- [34] H.D. Jang, Generation of silica nanoparticles from tetraethylorthosilicate (TEOS) vapor in a diffusion flame, *Aerosol Science & Technology*, 30 (1999) 477-488.
- [35] D. Nurkowski, P. Buerger, J. Akroyd, M. Kraft, A detailed kinetic study of the thermal decomposition of tetraethoxysilane, *Proceedings of the Combustion Institute*, 35 (2015) 2291-2298.
- [36] J. Jiang, M.H. Lee, P. Biswas, Model for nanoparticle charging by diffusion, direct photoionization, and thermionization mechanisms, *J. Electrostat.*, 65 (2007) 209-220.
- [37] R. Gunn, R.H. Woessner, Measurements of the systematic electrification of aerosols, *Journal of Colloid Science*, 11 (1956) 254-259.

- [38] D. Keefe, Charge equilibrium in aerosols according to the Boltzmann law, *Proceedings of the Royal Irish Academy*, 60 (1959) 27-45.
- [39] N.A. Fuchs, On the stationary charge distribution on aerosol particles in a bipolar ionic atmosphere, *Geofisica Pura e Applicata*, 56 (1963) 185-193.
- [40] A. Wiedensohler, An approximation of the bipolar charge distribution for particles in the submicron size range, *J. Aerosol. Sci.*, 19 (1988) 387-389.
- [41] W. Hoppel, G. Frick, Comment on the comparison of measured and calculated values of ion aerosol attachment coefficients, *Aerosol Sci. Technol.*, 11 (1989) 254-258.
- [42] X. López-Yglesias, R.C. Flagan, Ion-aerosol flux coefficients and the steady-state charge distribution of aerosols in a bipolar ion environment, *Aerosol Sci. Technol.*, 47 (2013) 688-704.
- [43] L. Tigges, A. Jain, H.J. Schmid, On the bipolar charge distribution used for mobility particle sizing: Theoretical considerations, *J. Aerosol. Sci.*, 88 (2015) 119-134.
- [44] J. Jiang, C. Kim, X. Wang, M.R. Stolzenburg, S.L. Kaufman, C. Qi, G.J. Sem, H. Sakurai, N. Hama, P.H. McMurry, Aerosol charge fractions downstream of six bipolar chargers: effects of ion source, source activity, and flowrate, *Aerosol Sci. Technol.*, 48 (2014) 1207-1216.
- [45] S.K. Friedlander, *Smoke, dust and haze: Fundamentals of aerosol behavior*, New York, Wiley-Interscience, 1977. 333 p., 1 (1977).
- [46] C. Larriba, C.J. Hogan Jr, M. Attoui, R. Borrajo, J.F. Garcia, J.F. de la Mora, The mobility-volume relationship below 3.0 nm examined by tandem mobility-mass measurement, *Aerosol Sci. Technol.*, 45 (2011) 453-467.
- [47] C. Larriba, C.J. Hogan, M. Attoui, R. Borrajo, J.F. Garcia, J.F. de la Mora, The Mobility-Volume Relationship below 3.0 nm Examined by Tandem Mobility-Mass Measurement, *Aerosol Science and Technology*, 45 (2011) 453-467.
- [48] H. Tammet, Size and Mobility of Nanometer particles, clusters, and Ions, *Journal of Aerosol Science*, 26 (1995) 459-475.
- [49] B.K. Annis, A.P. Malinauskas, E.A. Mason, Theory of drag on neutral or charged spherical aerosol particles, *Journal of Aerosol Science*, 3 (1972) 55-64.
- [50] S.K. Friedlander, *Smoke, Dust, and Haze: Fundamentals of Aerosol Dynamics*, Oxford University Press, 2000.
- [51] J.F. de la Mora, L. de Juan, T. Eichler, J. Rosell, Differential mobility analysis of molecular ions and nanometer particles, *TrAC Trends in Analytical Chemistry*, 17 (1998) 328-339.

[52] C. Larriba, C.J. Hogan, Ion Mobilities in Diatomic Gases: Measurement versus Prediction with Non-Specular Scattering Models, *The Journal of Physical Chemistry A*, 117 (2013) 3887-3901.

[53] B.K. Ku, J.F. de la Mora, Relation between Electrical Mobility, Mass, and Size for Nanodrops 1-6.5 nm in Diameter in Air, *Aerosol Science and Technology*, 43 (2009) 241-249.

[54] G. Steiner, T. Jokinen, H. Junninen, M. Sipilä, T. Petäjä, D. Worsnop, G.P. Reischl, M. Kulmala, High-resolution mobility and mass spectrometry of negative ions produced in a 241Am aerosol charger, *Aerosol Sci. Technol.*, 48 (2014) 261-270.

2. Measurement of Sub 2 nm Clusters of Pristine and Composite Metal Oxides during Nanomaterials Synthesis in Flame Aerosol Reactors

Reprinted with permission from: Fang, J., Wang, Y., Attoui, M., Chadha, T.S., Ray, J.R., Wang, W.N., Jun, Y.S. and Biswas, P., (2014). Measurement of sub-2 nm clusters of pristine and composite metal oxides during nanomaterial synthesis in flame aerosol reactors. *Analytical chemistry*, 86(15), pp.7523-7529. Copyright 2014 American Chemical Society

2. 1 Abstract

Measuring stable clusters to understand particle inception will aid the synthesis of well-controlled nanoparticles via gas-phase aerosol routes. Using a Half Mini differential mobility analyzer (DMA), the presence of monomers, dimers, trimers and tetramers were detected for the first time in a flame aerosol reactor during the synthesis of pristine TiO_2 and $\text{TiO}_2/\text{SiO}_2$ nanocomposites. Atomic force microscopy (AFM) confirmed the presence and the size of sub 2 nm clusters. The detection of these clusters elucidated the initial stages of particle formation during combustion synthesis and supported previous hypothesis that collisional growth from stable monomers of metal oxides are the first steps to particle growth.

2.2 Introduction

Recent advances in materials synthesis and design have focused on scalable schemes through aerosol routes [1, 2]. Among these schemes, flame aerosol synthesis is a dominant method for the production of nanoparticles such as titanium dioxide (6 Mtons/yr), carbon black (1.5 Mtons/yr), and fumed silica (50 ktons/yr). To extend this methodology to synthesize advanced materials for applications such as catalysis [3], batteries, and photovoltaic systems [4]. A greater degree of precision and control is essential. As we lack a fundamental understanding of particle inception and growth mechanisms, our ability to control process parameters is limited. In addition, challenges in studying flame aerosol reactors arise from the fact that particle formation occurs at extremely high temperatures and short length and times scales. A direct measurement of clusters below 2nm, hitherto not done before, will help improve our understanding and address these limitations [5, 6].

Oxide nanoparticles in flames are conjectured to be formed by the oxidation/decomposition of a precursor which results in the formation of molecules that are assumed to be stable clusters. A simple first order precursor decomposition rate [7-9] is often used to determine the rate of formation of these clusters. Following this initial formation rate, particle growth by collision mechanisms has been proposed [10, 11]. Recently, molecular modeling approaches have also been used to outline the pathways of cluster growth [12, 13]. In addition to single component oxides, doped and composite oxides are often synthesized for a variety of applications [14, 15]. The presence of multiple components resulting in composite oxide formation further complicates the understanding of the synthesis process. Real time measurements of particle size based on electrical mobility is the most commonly utilized characterization method however limitations in the DMA design has constrained the ability to classify particles below 2nm [16, 17]. In this technique, a

quantitative size distribution at a given sampling point is measured by extracting a sample from the reactor and measuring the electrical mobility of the sampled aerosol nanoparticles. Alternatively, there have been studies on measuring the concentrations of gas phase products from precursor decomposition (e.g. by LIF [18-20]), however, real time particle measurements using this technique have been limited to sizes greater than 5 nm. Time-resolved laser-induced incandescence has also been used for in-situ real time particle measurements during combustion synthesis [21, 22]. This technique has been applied towards the synthesis of iron nanoparticles [23], titania nanoparticles [24], soot [25], and carbon blacks [26] but it has shown similar limitations in size measurements. Thus, there is a gap in the measurement of the smallest stable clusters between the molecular species (by mass spectrometry [27]) and larger particles (by real time mobility instruments [28]). The direct measurement of clusters in this gap will aid in the verification of various proposed pathways and provide data for accurate kinetic estimation of particle formation rates.

Additional considerations must be taken into account when attempting to measure particles below 2 nm. Below 2 nm, commercially available differential mobility analyzers (DMAs) suffer from very low resolution due to Brownian broadening and flow instabilities[29-31]. Recent advances in DMAs have allowed for detailed analyses of the size, mobility, and mass of sub 3 nm particles [32, 33]. High flow DMAs have already been applied successfully to studying atmospheric nucleation [34] and sub 3 nm cluster mobility and mass [35-37]. A Half Mini DMA is an example of such an instrument that was developed by de la Mora and Kozlowski [38]. However, no size measurements of small clusters have been made during a nanoparticle synthesis process.

In this study we characterized sub 2 nm clusters during the synthesis of pristine and multicomponent TiO₂ in a premixed flame reactor using a Half Mini DMA. Cluster size distributions in flame aerosol reactors were measured using the Half Mini DMA and then verified by atomic force microscopy (AFM) size measurements. Process parameters such as feed rate and height above the burner head were varied to examine the evolution of discrete size distributions and presence of ions. We examined how the addition of dopants affects the mechanisms of metal oxide nanoparticle inception. To the best of our knowledge, our study is the first attempt to demonstrate the existence of stable clusters during combustion synthesis and provides new understanding on cluster formation.

2.3 Experimental Methods

2.3.1 Synthesis of TiO₂ in a Flat Flame Aerosol Reactor

Titanium dioxide nanoparticles were synthesized in a premixed methane-air flat flame aerosol reactor (Figure 2.1a). Premixed methane-air flat flames have been used successfully to generate ultrafine aerosols and serve as a model for more complex hydrocarbon flames [39]. The flame geometry is a radially uniform thin flame sheet stabilized over a 1” burner head which consisted of a honey comb nozzle mounted on 1/8” diameter stainless steel balls. The various gases were premixed prior to entering the burner head, with the methane and oxygen flow rates set at 0.89 and 2.00 lpm, respectively, while the nitrogen flow rate was controlled so that the flow velocity in the burner head was enough to stabilize the flame. In this study, the total nitrogen flow was maintained at 6.0 lpm. Gas flow rates were controlled using mass flow controllers (MKS Instruments).

Organometallic precursors were introduced into the premixed flame by bubbling nitrogen through a sealed bubbler (MDC Vacuum Products) containing titanium(IV) isopropoxide (TTIP

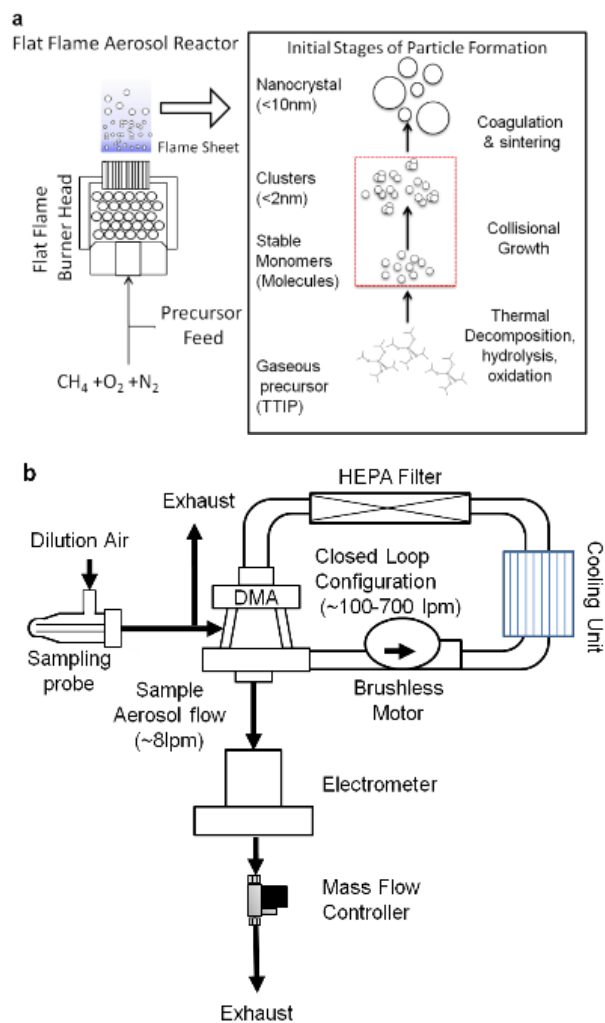


Figure 2.1: (a) Flat flame Aerosol Reactor used for the synthesis of pristine and $\text{TiO}_2/\text{SiO}_2$ nanocomposites with a schematic diagram of the initial stages of particle formation during combustion synthesis. Collisional growth mechanisms from stable monomers to clusters (highlighted) have yet to be established. (b) Experimental setup of Half Mini DMA operated under closed loop conditions for measurement of sub 2 nm cluster size distributions.

,97%, Sigma Aldrich) or tetraethylorthosilicate (TEOS, 99%, Sigma Aldrich) and fed to the premixed flame. The tubing leading up to the burner head was wrapped with heating tape to prevent precursor condensation. The molar feed rate of the precursor was calculated using the

feed gas flow rates and vapor pressure data from Siefering and Griffin [40] for TTIP and Jang[41] for TEOS.

2.3.2 Utilization of a Half Mini DMA for Online Measurement of Sub 2 nm Clusters

Flame generated nanoparticles were measured directly above the flame using a venturi sampling probe with a temperature adjusted dilution ratio of 120:1. The dilution gas used was particle free, oil free, dry compressed air with a temperature of 298K. The sample aerosol was then injected into the Half Mini DMA at 8 lpm while excess flow was exhausted. Stainless steel sampling lines were used to ensure no contamination, and the tubing length between the sampling probe outlet and DMA inlet was kept at 10 cm to minimize particle diffusion losses.

Cluster size distributions were measured using the Half Mini DMA (Figure 2.1b). Design considerations, calibration, and the operation of high resolution DMAs have been reported by de la Mora and Kozlowski [38]. The configuration of the Half Mini DMA model used in this study had a classification length of 4 mm with an inner and outer radius of 4 mm and 6 mm respectively. The Half Mini DMA was run under a closed loop configuration using filtered room air as the sheath gas at an approximate sheath flow rate of 200 lpm using a DC brushless motor (Domel). Sheath air flow rates were measured before and after each experimental run by electrospray calibration using a 200 μ M tetraheptylammonium bromide (THABr, 99.9%, Sigma Aldrich) solution diluted in methanol [30, 42]. An inline radiator and HEPA filter was used to cool the sheath flow and remove unclassified nanoparticles. A high voltage power supply (Applied Kilovolts) using a \pm 0-10 V control signal was used to control the DMA voltage from 0-5 kV with both positive and negative polarity. The concentration of classified particles was detected using a Faraday cup electrometer. The sample aerosol flow was controlled using a mass flow controller

(MKS Instruments) downstream from the Faraday cup electrometer. Data acquisition and control was performed using a data acquisition system (Data Translation Inc.) and LabView (National Instruments Corporation).

2.3.3 Atomic Force Microscopy of Sub 2 nm TiO₂ clusters

To verify the cluster size distributions measured by the Half Mini DMA, *in situ* thermophoretic sampling onto single crystal silicon wafers was conducted. The substrates were rapidly passed 5 times through the flame approximately 25 mm above the burner head to allow for rapid thermophoretic collection onto the cold substrate [6]. Using an AFM (Nanoscope V Multimode, Veeco), height, amplitude and phase contrast images were captured in air under ambient conditions in the tapping mode. The AFM probes, 125 μm in length, were made of phosphorus (n) doped silicon tips with a nominal tip radius of 10 nm (MPP-11100-10, Bruker probes). The images were collected with drive frequencies of 312–320 kHz, typical spring constants of 20–80 N/m, scan sizes of 2 μm \times 2 μm , and scan rates of around 0.8 – 1.0 Hz.

2.3.4 Electrical Mobility of Sub 2 nm Clusters

Using the measured cluster electrical mobility, the species was inferred by calculating equivalent mobility diameters and mass. Below 2 nm, the relationship between a particle's drag force and size is different than the relationship in the continuum regime [43]. In the continuum regime, aerosol mobility may be described using the Stokes-Millikan relationship as a function of the particle diameter and the particle charge. However, as the cluster size further decreases towards molecular dimensions, charged cluster and dipole interactions along with the presence of diffuse collisions can significantly increase the mobility [44]. In this work, the equivalent mobility

diameter (d_p) of charged clusters was calculated using the curve fitted Stokes-Millikan law provided by Mäkelä et al. (equation 2.1, [45]). Furthermore, the mass equivalent particle diameter (d_m) was calculated by adding a gas molecule diameter (d_g) of 0.3 nm thus replacing d_p with d_m+d_g . Since the bulk density of TiO₂ cannot be used to infer the particle diameter in this size range; the mobility (Z) of TiO₂ molecular clusters was calculated using the mass (m) based empirical correlations presented by Mäkelä et al [46].:

$$Z = 4.33317m^{-0.0376} \exp[-0.0347 \ln^2(m)] \quad (2.1)$$

The calculated inverse mobility ($1/Z$, Vs/cm²) of the TiO₂ and SiO₂ monomers, dimers, and trimers based on this expression are listed in Table 2.1 for comparison with the measured inverse mobilities.

Table 2.1: The inverse mobility for TiO₂ and SiO₂ clusters determined using 2 methods. The calculated inverse mobility is based on empirical mass-mobility correlations[46] for clusters carrying a unit charge. The equivalent mass diameter was calculated from the measured cluster mobility using the curve fitted Stokes-Millikan relationship[45] and adjusting the particle diameter by subtracting an effective gas molecule diameter of 0.3 nm.

Cluster Type	Cluster Size	Mass (Dalton)	Calculated Inverse Mobility (Vs/cm ²)	Mass equivalent diameter (nm)
TiO ₂	1 ○	79.87	0.530	0.74
	2 ∞	159.73	0.682	0.88
	3 ∞∞	239.60	0.804	0.98
	4 ∞∞∞	319.46	0.909	1.07
SiO ₂	1 ●	60.80	0.483	0.70
	2 ●●	121.60	0.615	0.83
	3 ●●●	182.40	0.719	0.92
OH	1 ●	17.01	0.344	-

2.3.5 Experimental Plan

To understand cluster growth mechanisms, we measured sub 2nm size distributions in flame aerosol reactors and their concentrations for different process parameters. A list of the experiments performed is summarized in Table 2.1. Measurements of positive and negative cluster size distributions were made for Tests 1-7. The effect of precursor concentration was studied by varying the precursor feed rates (Tests 1-4). The effect of residence time was studied by sampling at various heights above the burner head at a fixed feed rate (Tests 5-7). Finally, cluster formation for mixed oxides was studied by comparing pristine TiO_2 and nanocomposite $\text{TiO}_2/\text{SiO}_2$ synthesis (Tests 8 and 9).

Table 2.2: List of experimental parameters for measuring charged clusters. A flat flame aerosol reactor was used for combustion synthesis of pristine and nanocomposite $\text{TiO}_2/\text{SiO}_2$ and charged clusters were measured using a Half Mini DMA.

	Test Number	TTIP Feed Rate (mmol/hr)	TEOS Feed Rate (mmol/hr)	Sampling Height (mm)
Effect of Precursor Feed Rate	1	0.066	0	25
	2	0.2	0	25
	3	0.33	0	25
	4	0.66	0	25
Effect Sampling Height	5	0.2	0	3.5
	6	0.2	0	32
	7	0.2	0	42
Nanocomposite Synthesis	8	0	0.11	25
	9	0.33	0.11	25

2.4 Results and Discussion

To obtain background measurements, the presence of charged ions in a methane-air flat flame using the Half Mini DMA without the addition of precursors was measured. Figure 2.2 displays the number concentration of charged clusters plotted as a function of the signal intensity (A.U.) on the y-axis with respect to the inverse mobility ($1/Z$, Vs/cm²) on the x-axis. Two characteristic peaks can be seen for positive ions, with an inverse mobility of 0.48 Vs/cm² and 0.51 Vs/cm². Similarly, two mobility peaks for negative ions are observed at 0.48 and 0.54 Vs/cm². The presence of these ions in the flame environment will affect both the chemical pathways of precursor decomposition and the charging mechanisms for nanoparticles, thereby affecting particle inception and growth. More specifically, the presence of ions may promote particle formation as it is well known that the presence of ions can significantly lower the free energy of cluster formation due to electrostatic interactions [47].

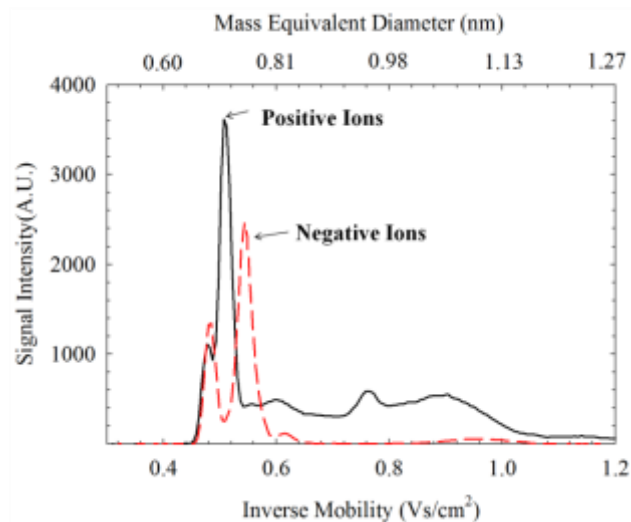


Figure 2.2: Measurements of sub 2 nm cluster size distributions in a blank methane-air flat flame sampled 3.5 mm above the burner head using the Half Mini DMA for positively charged (—) and negatively charged (---) ions.

2.4.1 Single Component Nanoparticle Synthesis

Upon the addition of either TTIP or TEOS precursors in the flat flame, new distinct clusters were detected (See Figure 2.3). The emergence of these new peaks implies that they are charged clusters of TiO_2 and SiO_2 molecules in the flame. These clusters can be assumed to be singly charged because in flat flames, diffusion charging is the dominant charging mechanism [48]. These peaks are more characteristic of discrete size distributions and support the notion of single molecules acting as stable nuclei for particle inception and growth in the formation of metal oxide nanoparticles. Scans of positive ions and negative ions in the Half Mini DMA show that the concentration of positively charged clusters is much higher than that of negatively charged clusters; this implies that positively charged TiO_2 and SiO_2 clusters may play a significant role in the overall particle formation process. Higher concentrations of positively charged clusters indicate that thermionic charging mechanisms may also contribute to particle charging [49]. As seen in Figure 2.3b, many types of stable clusters are present during SiO_2 cluster formation, indicating the presence of stable intermediate species such as partially oxidized silicon oxides. In addition, OH attachment has been shown to be significant during the cluster formation of SiO_2 from TEOS decomposition showing the importance of $\text{Si}(\text{OH})_4$ monomers [50]. Ours is the first real-time online experimental evidence demonstrating the presence of stable clusters during the initial stages of particle growth. Atomic force microscopy was used to measure the physical cluster size to allow for comparisons with mobility equivalent diameter. Figure 2.4 shows AFM images and their analyses for flame generated clusters deposited on single crystalline Si wafers for experimental test number 1 (Table 2.1). Because these clusters were deposited thermophoretically, both charged and uncharged species were measured.

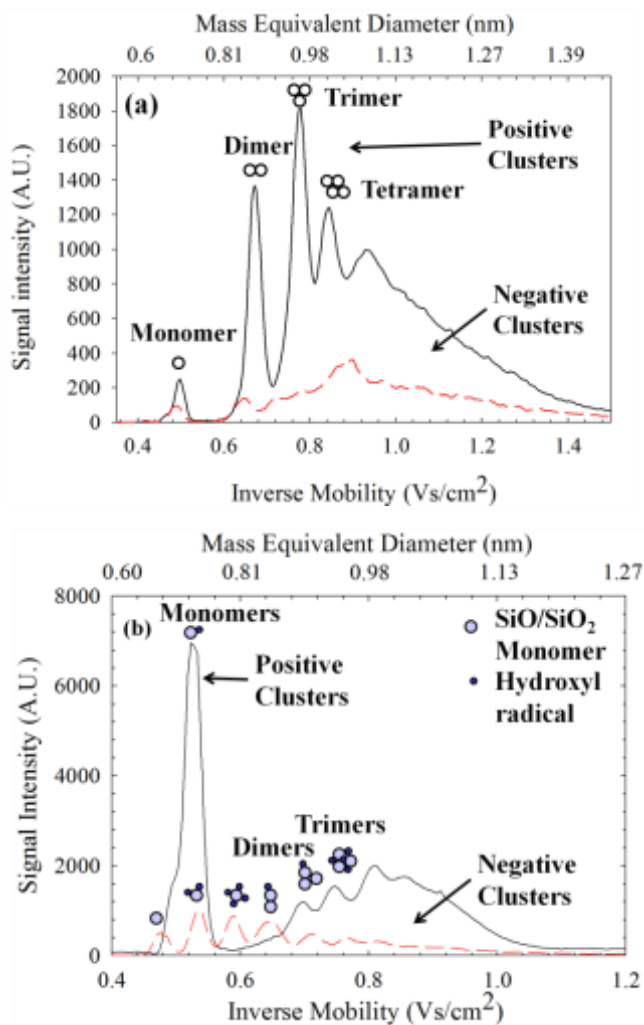


Figure 2.3: (a) TiO₂ cluster size distribution measurements at a height of 25 mm above the burner head with a TTIP precursor feed rate of 0.20 mmol/hr for positively charged (—) and negatively charged (---) particles; (b) SiO₂ cluster size distribution measurements at a height of 25 mm above the burner head with a TEOS precursor feed rate of 0.25 mmol/hr for positively charged (—) and negatively charged (---) nanoparticles.

Figures 2.4a and 2.4c show the AFM-height and AFM-phase images. The AFM-height images (Figure 2.4a) were used for the measurement of physical particle size while the phase plots (Figure 4b) were used to distinguish mechanical properties due to different phase of particles

from the Si substrate surface [51]. Resulting particle sizes are summarized in a histogram plot (Figure 2.4b) where the size of more than 100 randomly chosen clusters was measured. These results provide further evidence that sub 2 nm clusters are present for combustion synthesis of nanoparticles. From the sample of particles, the cluster sizes ranged from 0.5-5.03 nm. However very few clusters were larger than 2 nm. By comparing Figure 2.4d to cluster size distribution scans (Figure 2.3a) it could be seen that a high concentration of sub 2 nm clusters exist in both cases while the highest concentrations exist at 1nm. Because the surface roughness of the substrate was approximately 0.3 nm, AFM measurements were limited to particle sizes down to 0.5 nm below which the signal is similar to noise level.

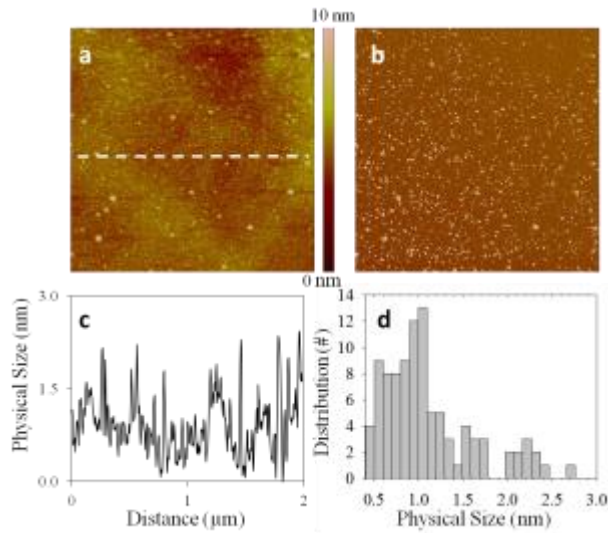


Figure 2.4: (a) AFM image of TiO_2 clusters for substrate surface topography. (b) The corresponding height profile taken across the white dotted line is given below. (c) The AFM-phase image shows the Si wafer surface as the darker color and the TiO_2 clusters as the lighter color providing evidence of cluster formation. (d) The particle size distribution of over 100 particles is given below the AFM-height image.

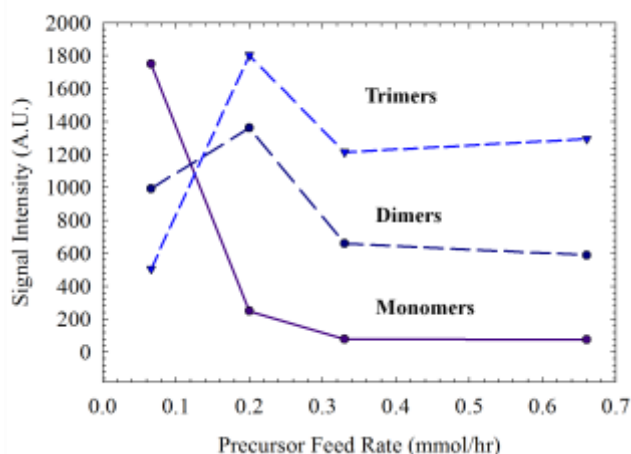


Figure 2.5: Overall trends of measured TiO_2 cluster number concentrations presented as signal intensity on the y-axis (A.U.) with respect to the TTIP precursor feed rate for positively charged clusters on the x-axis (mmol/hr) measured in a methane-air flat flame reactor at a height of 3.5 mm above the burner head.

2.4.2 Effect of Precursor Feed Rate

To illustrate the kinetics of cluster formation, the precursor concentration was varied in the flame aerosol reactor. In Figure 2.5, the effect of four different precursor feed rates for TTIP ranging from 0.022 mmol/hr to 0.22 mmol/hr on particle number concentration of different clusters are compared. As the feed rate is increased, the relative heights of positively charged TiO_2 peaks change. Most notably the rapid decrease in the height of the monomer peak (0.526 Vs/cm^2) implies that these particles were being rapidly consumed at a higher rate due to collisional growth mechanisms. Using equation 2.1, the atomic mass of the respective clusters was estimated (Table 2.2). From the five distinct peaks in Figure 2.3b-2.3d, the average atomic mass in Daltons can be estimated as 79.07, 172.98, 247.36, and 311.67 for peaks 1-4, respectively. Comparing these values to the mass of TiO_2 clusters, we find that they correspond

to a calculated difference of 1.01%, 8.30%, 3.24%, and 2.44% for peaks 1-4. The measured electrical mobility of these clusters and their estimated size provides further support that these ion peaks are monomers, dimers, and trimers of TiO_2 .

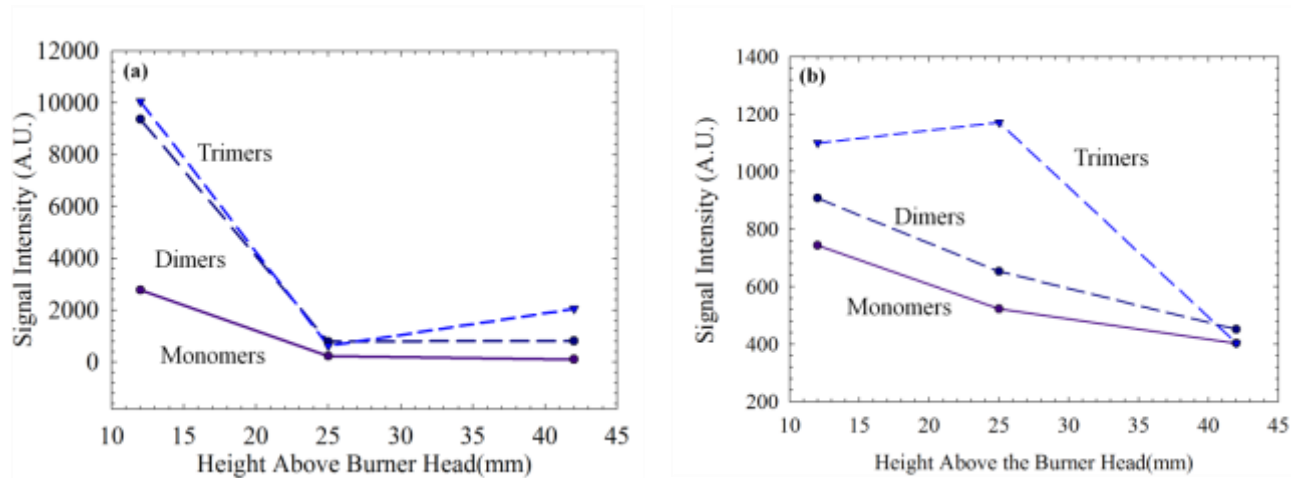


Figure 2.6: Effect of residence time for (a) positively charged (b) and negatively charged TiO_2 cluster number concentrations represented as signal intensity on the y-axis (A.U.) and height above the burner head (mm) on the x-axis for a fixed precursor feed rate of 0.33 mmol/hr.

2.4.3 Effect of Sampling Height

To understand both the kinetics of particle formation and the role of clusters, the effect of sampling height above the burner head was examined (Figure 2.6). The residence time in the flame aerosol reactor was approximately 0.1-3 ms depending on the sampling height, while the characteristic reaction time for TTIP was approximately 3 ms [52]. Because the residence time and characteristic reaction times were on the same order of magnitude, stable clusters were detected. The concentration of monomers, dimers, and trimers changed with increasing height; most notably, the concentration of all three clusters decreased. This decrease demonstrates that initially, stable primary clusters of TiO_2 were being formed and then consumed as the reaction

proceeds. The concentration of TiO_2 monomers decreased much more dramatically than that of the dimer and trimer peaks, indicating a scavenging of monomers through cluster collisions.

2.4.4 Synthesis of Multicomponent $\text{TiO}_2/\text{SiO}_2$ Nanocomposites

Mechanisms of nanocomposite formation in flames were studied by introducing multiple precursors into the flame aerosol reactor. Using TTIP and TEOS as precursors, we synthesized mixed oxide nanocomposites of TiO_2 and SiO_2 (Figure 2.7) at a molar ratio of 1:3 to elucidate the mechanisms of multicomponent nanoparticle inception. Figure 2.7 displays the resulting scans from multicomponent $\text{SiO}_2/\text{TiO}_2$ mixtures. Comparing the resulting scans for pristine TiO_2 , several peak shifts are observed, while other characteristic peaks also emerge. These peaks are hypothesized to be stable clusters of mixed oxides. Although the exact composition of these clusters is not known, it is clear that they consist of various combinations of SiO_2 and TiO_2

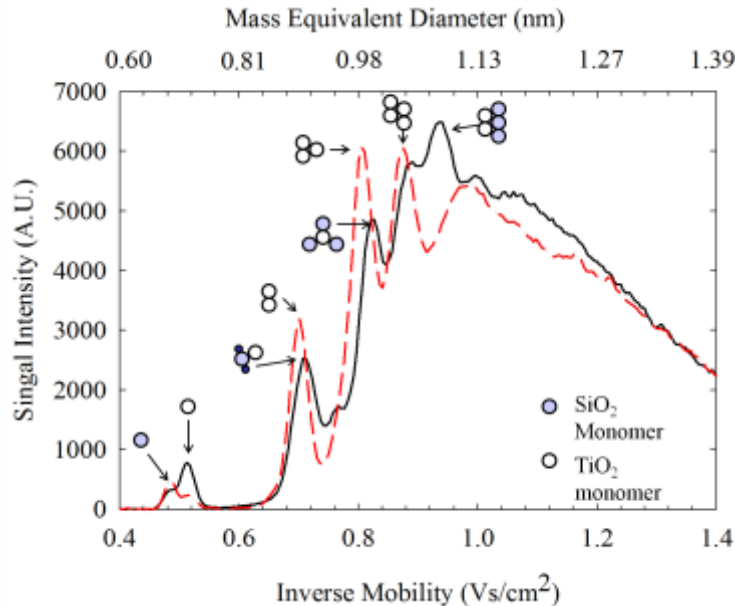


Figure 2.7: Cluster size distribution measurements 25 mm above the burner head in a flame aerosol reactor comparing the flame synthesis of pristine TiO_2 (---) and TiO_2 doped with SiO_2 (—) at a molar ratio of 3:1.

monomers and dimers, suggesting that stable clusters of mixed oxides will begin to form immediately. Of the several pathways hypothesized previously by Ehrman et al. [53], radical driven pathways appear to dominate at the initial stages. As these mixed oxides begin to grow in size, they may begin to coalesce and form stable particles, while phase segregation will occur within the particle via liquid or solid state diffusion [54].

2.5 Conclusions

In summary, for the first time, the presence of stable clusters below 2 nm during the flame synthesis of pristine and multicomponent TiO_2 and SiO_2 was measured. Using a high resolution, high flow, Half Mini DMA, natively charged clusters during the flame synthesis of pristine and doped TiO_2 were detected. This was verified by an AFM measurement of deposited TiO_2 clusters. During the flame synthesis of pristine TiO_2 distinct peaks corresponding to monomers, dimers, trimers, and tetramers were detected. With an increase in residence time in the flame, the concentration of these clusters decreased due to collisional growth. When multiple precursors, mixed oxides begin to form at the very initial stages of cluster formation. Further work would include characterizing the fraction of charged and uncharged nanoparticles along with the implementation of a DMA-Mass spectrometry system to characterize the mass mobility relations for metal oxide clusters.

2.6 References

- [1] W.-N. Wang, Y. Jiang, P. Biswas, Evaporation-Induced Crumpling of Graphene Oxide Nanosheets in Aerosolized Droplets: Confinement Force Relationship, *Journal of Physical Chemistry Letters*, 3 (2012) 3228-3233.
- [2] P.M. Rao, X. Zheng, Rapid Catalyst-Free Flame Synthesis of Dense, Aligned α -Fe₂O₃ Nanoflake and CuO Nanoneedle Arrays, *Nano Letters*, 9 (2009) 3001-3006.
- [3] W.N. Wang, W.J. An, B. Ramalingam, S. Mukherjee, D.M. Niedzwiedzki, S. Gangopadhyay, P. Biswas, Size and structure matter: Enhanced CO₂ photoreduction efficiency by size-resolved ultrafine Pt nanoparticles on TiO₂ single crystals, *Journal of the American Chemical Society*, 134 (2012) 11276-11281.
- [4] V.B. Shah, P. Biswas, Aerosolized Droplet Mediated Self-Assembly of Photosynthetic Pigment Analogues and Deposition onto Substrates, *ACS Nano*, 8 (2014) 1429-1438.
- [5] M.L. Eggersdorfer, A.J. Grohn, C.M. Sorensen, P.H. McMurry, S.E. Pratsinis, Mass-mobility characterization of flame-made ZrO₂ aerosols: Primary particle diameter and extent of aggregation, *J. Colloid Interface Sci.*, 387 (2012) 12-23.
- [6] G. Yang, P. Biswas, Study of the Sintering of Nanosized Titania Agglomerates in Flames Using In Situ Light Scattering Measurements, *Aerosol Science and Technology*, 27 (1997) 507-521.
- [7] K. Okuyama, J.-T. Jeung, Y. Kousaka, H.V. Nguyen, J.J. Wu, R.C. Flagan, Experimental control of ultrafine TiO₂ particle generation from thermal decomposition of titanium tetraisopropoxide vapor, *Chemical Engineering Science*, 44 (1989) 1369-1375.
- [8] A. Fujishima, X. Zhang, D.A. Tryk, TiO₂ photocatalysis and related surface phenomena, *Surface Science Reports*, 63 (2008) 515-582.
- [9] S.E. Pratsinis, H. Bai, P. Biswas, M. Frenklach, S.V.R. Mastrangelo, Kinetics of Titanium(IV) Chloride Oxidation, *Journal of the American Ceramic Society*, 73 (1990) 2158-2162.
- [10] G.D. Ulrich, Theory of Particle Formation and Growth in Oxide Synthesis Flames, *Combustion Science and Technology*, 4 (1971) 47-57.

- [11] A.G. Shmakov, O.P. Korobeinichev, D.A. Knyazkov, A.A. Paletsky, R.A. Maksutov, I.E. Gerasimov, T.A. Bolshova, V.G. Kiselev, N.P. Gritsan, Combustion chemistry of $Ti(OC_3H_7)_4$ in premixed flat burner-stabilized $H_2/O_2/Ar$ flame at 1atm, Proceedings of the Combustion Institute, 34 (2013) 1143-1149.
- [12] M.R. Zachariah, W. Tsang, Application of Ab-Initio Molecular-Orbital and Reaction-Rate Theories to Nucleation Kinetics, Aerosol Science and Technology, 19 (1993) 499-513.
- [13] M.R. Zachariah, W. Tsang, Theoretical calculation of thermochemistry, energetics, and kinetics of high-temperature SixHyOz reactions, The Journal of Physical Chemistry, 99 (1995) 5308-5318.
- [14] P. Biswas, C.Y. Wu, M.R. Zachariah, B. McMillin, Characterization of iron oxide-silica nanocomposites in flames .2. Comparison of discrete-sectional model predictions to experimental data, Journal of Materials Research, 12 (1997) 714-723.
- [15] M.R. Zachariah, R.D. Shull, B.K. McMillin, P. Biswas, In situ characterization and modeling of the vapor-phase formation of a magnetic nanocomposite, in: G.M. Chow, K.E. Gonsalves (Eds.) Nanotechnology: Molecularly Designed Materials, 1996, pp. 42-63.
- [16] A. Camenzind, W.R. Caseri, S.E. Pratsinis, Flame-made nanoparticles for nanocomposites, Nano Today, 5 (2010) 48-65.
- [17] J. Jingkun, C. Da-Ren, B. Pratim, Synthesis of nanoparticles in a flame aerosol reactor with independent and strict control of their size, crystal phase and morphology, Nanotechnology, 18 (2007) 285603.
- [18] B.K. McMillin, P. Biswas, M.R. Zachariah, In situ characterization of vapor phase growth of iron oxide-silica nanocomposites .1. 2-D planar laser-induced fluorescence and Mie imaging, Journal of Materials Research, 11 (1996) 1552-1561.
- [19] P. Biswas, M.R. Zachariah, In Situ Immobilization of Lead Species in Combustion Environments by Injection of Gas Phase Silica Sorbent Precursors, Environmental Science & Technology, 31 (1997) 2455-2463.
- [20] C. Hecht, H. Kronemayer, T. Dreier, H. Wiggers, C. Schulz, Imaging measurements of atomic iron concentration with laser-induced fluorescence in a nanoparticle synthesis flame reactor, Applied Physics B, 94 (2009) 119-125.

- [21] P. Roth, Particle synthesis in flames, *Proceedings of the Combustion Institute*, 31 (2007) 1773-1788.
- [22] D.E. Rosner, Flame Synthesis of Valuable Nanoparticles: Recent Progress/Current Needs in Areas of Rate Laws, Population Dynamics, and Characterization, *Industrial & Engineering Chemistry Research*, 44 (2005) 6045-6055.
- [23] A. Eremin, E. Gurentsov, C. Schulz, Influence of the bath gas on the condensation of supersaturated iron atom vapour at room temperature, *Journal of Physics D: Applied Physics*, 41 (2008) 055203.
- [24] F. Cignoli, C. Bellomunno, S. Maffi, G. Zizak, Laser-induced incandescence of titania nanoparticles synthesized in a flame, *Applied Physics B*, 96 (2009) 593-599.
- [25] S. Will, S. Schraml, K. Bader, A. Leipertz, Performance Characteristics of Soot Primary Particle Size Measurements by Time-Resolved Laser-Induced Incandescence, *Appl. Opt.*, 37 (1998) 5647-5658.
- [26] S. Dankers, S. Schraml, S. Will, A. Leipertz, Application of Laser-Induced Incandescence for the Determination of Primary Particle Sizes of Nanoparticles Demonstrated Using Carbon Blacks, *Chemical Engineering & Technology*, 25 (2002) 1160-1164.
- [27] R.E. Goacher, H. Luo, J.A. Gardella, Formation of High-Mass Cluster Ions from Compound Semiconductors Using Time-of-Flight Secondary Ion Mass Spectrometry with Cluster Primary Ions, *Analytical Chemistry*, 80 (2008) 3261-3269.
- [28] S. Guha, X. Ma, M.J. Tarlov, M.R. Zachariah, Quantifying Ligand Adsorption to Nanoparticles Using Tandem Differential Mobility Mass Analysis, *Analytical Chemistry*, 84 (2012) 6308-6311.
- [29] J.G. Radney, X. Ma, K.A. Gillis, M.R. Zachariah, J.T. Hodges, C.D. Zangmeister, Direct Measurements of Mass-Specific Optical Cross Sections of Single-Component Aerosol Mixtures, *Analytical Chemistry*, 85 (2013) 8319-8325.
- [30] Y. Wang, J. Fang, M. Attoui, T.S. Chadha, W.-N. Wang, P. Biswas, Application of Half Mini DMA for sub 2 nm particle size distribution measurement in an electrospray and a flame aerosol reactor, *J. Aerosol. Sci.*, 71 (2014) 52-64.

- [31] C.J. Hogan, E.M. Kettleson, B. Ramaswami, D.R. Chen, P. Biswas, Charge reduced electrospray size spectrometry of mega- and gigadalton complexes: Whole viruses and virus fragments, *Analytical Chemistry*, 78 (2006) 844-852.
- [32] B.K. Ku, J.F. de la Mora, Relation between Electrical Mobility, Mass, and Size for Nanodrops 1-6.5 nm in Diameter in Air, *Aerosol Science and Technology*, 43 (2009) 241-249.
- [33] D.A. Saucy, S. Ude, I.W. Lenggoro, J. Fernandez de la Mora, Mass Analysis of Water-Soluble Polymers by Mobility Measurement of Charge-Reduced Ions Generated by Electrosprays, *Analytical Chemistry*, 76 (2004) 1045-1053.
- [34] M. Kulmala, J. Kontkanen, H. Junninen, K. Lehtipalo, H.E. Manninen, T. Nieminen, T. Petäjä, M. Sipilä, S. Schobesberger, P. Rantala, A. Franchin, T. Jokinen, E. Järvinen, M. Äijälä, J. Kangasluoma, J. Hakala, P.P. Aalto, P. Paasonen, J. Mikkilä, J. Vanhanen, J. Aalto, H. Hakola, U. Makkonen, T. Ruuskanen, R.L. Mauldin, J. Duplissy, H. Vehkamäki, J. Bäck, A. Kortelainen, I. Riipinen, T. Kurtén, M.V. Johnston, J.N. Smith, M. Ehn, T.F. Mentel, K.E.J. Lehtinen, A. Laaksonen, V.-M. Kerminen, D.R. Worsnop, Direct Observations of Atmospheric Aerosol Nucleation, *Science*, 339 (2013) 943-946.
- [35] L.A. Sgro, A.C. Barone, M. Commodo, A. D'Alessio, A. De Filippo, G. Lanzuolo, P. Minutolo, Measurement of nanoparticles of organic carbon in non-sooting flame conditions, *Proceedings of the Combustion Institute*, 32 (2009) 689-696.
- [36] M. Attoui, M. Paragano, J. Cuevas, J.F. de la Mora, Tandem DMA Generation of Strictly Monomobile 1-3.5 nm Particle Standards, *Aerosol Science and Technology*, 47 (2013) 499-511.
- [37] E. Criado-Hidalgo, J. Fernández-García, J. Fernández de la Mora, Mass and Charge Distribution Analysis in Negative Electrosprays of Large Polyethylene Glycol Chains by Ion Mobility Mass Spectrometry, *Analytical Chemistry*, 85 (2013) 2710-2716.
- [38] J.F. de la Mora, J. Kozlowski, Hand-held differential mobility analyzers of high resolution for 1-30 nm particles: Design and fabrication considerations, *Journal of Aerosol Science*, 57 (2013) 45-53.
- [39] R. Vijayakumar, K.T. Whitby, Flat Flame Ultrafine Aerosol Generator, *Aerosol Science and Technology*, 3 (1984) 17-24.
- [40] K. Siefert, G. Griffin, Growth kinetics of CVD TiO₂: influence of carrier gas, *Journal of The Electrochemical Society*, 137 (1990) 1206-1208.

- [41] H.D. Jang, Generation of Silica Nanoparticles from Tetraethylorthosilicate (TEOS) Vapor in a Diffusion Flame, *Aerosol Science and Technology*, 30 (1999) 477-488.
- [42] S. Ude, J.F. de la Mora, Molecular monodisperse mobility and mass standards from electrosprays of tetra-alkyl ammonium halides, *Journal of Aerosol Science*, 36 (2005) 1224-1237.
- [43] H. Tammet, Size and Mobility of Nanometer particles, clusters, and Ions, *Journal of Aerosol Science*, 26 (1995) 459-475.
- [44] M.F. Mesleh, J.M. Hunter, A.A. Shvartsburg, G.C. Schatz, M.F. Jarrold, Structural Information from Ion Mobility Measurements: Effects of the Long-Range Potential, *The Journal of Physical Chemistry*, 100 (1996) 16082-16086.
- [45] J.M. Mäkelä, M. Riihelä, A. Ukkonen, V. Jokinen, J. Keskinen, Comparison of mobility equivalent diameter with Kelvin-Thomson diameter using ion mobility data, *The Journal of Chemical Physics*, 105 (1996) 1562.
- [46] J.M. Mäkelä, V. Jokinen, T. Mattila, A. Ukkonen, J. Keskinen, Mobility distribution of acetone cluster ions, *Journal of Aerosol Science*, 27 (1996) 175-190.
- [47] J.L. Katz, J.A. Fisk, V.M. Chakarov, Condensation of a supersaturated vapor IX. Nucleation on ions, *The Journal of Chemical Physics*, 101 (1994) 2309-2318.
- [48] J. Jiang, M.H. Lee, P. Biswas, Model for nanoparticle charging by diffusion, direct photoionization, and thermionization mechanisms, *J. Electrostat.*, 65 (2007) 209-220.
- [49] M. Sahu, J. Park, P. Biswas, In Situ Charge Characterization of TiO₂ and Cu-TiO₂ Nanoparticles in a Flame Aerosol Reactor, *J. Nanopart. Res.*, 14 (2012).
- [50] S. Shekar, M. Sander, R.C. Riehl, A.J. Smith, A. Braumann, M. Kraft, Modelling the flame synthesis of silica nanoparticles from tetraethoxysilane, *Chemical Engineering Science*, 70 (2012) 54-66.
- [51] K. Babcock, C. Prater, Phase imaging: beyond topography, *Digital Instruments*, Santa Barbara, CA, (1995).
- [52] K. Okuyama, R. Ushio, Y. Kousaka, R.C. Flagan, J.H. Seinfeld, Particle generation in a chemical vapor deposition process with seed particles, *AIChE journal*, 36 (1990) 409-419.

[53] S.H. Ehrman, S.K. Friedlander, M.R. Zachariah, Characteristics of SiO₂/TiO₂ nanocomposite particles formed in a premixed flat flame, *J. Aerosol. Sci.*, 29 (1998) 687-706.

[54] S.H. Ehrman, S.K. Friedlander, M.R. Zachariah, Phase segregation in binary SiO₂/TiO₂ and SiO₂/Fe₂O₃ nanoparticle aerosols formed in a premixed flame, *Journal of Materials Research*, 14 (1999) 4551-4561.

3. Cluster Formation Mechanisms of Titanium Dioxide During Combustion Synthesis

3.1 Abstract

To investigate cluster formation pathways of TiO_2 during combustion synthesis we measured natively charged ions in an atmospheric pressure interface time-of-flight (APi-TOF) mass spectrometer. Titanium tetraisopropoxide (TTIP) precursor was added to a premixed methane air flat flame aerosol reactor to synthesize TiO_2 nanoparticles. Clusters formed in the flame were extracted by a Venturi dilution probe and injected into the inlet of the APi-TOF. Previous studies have assumed a conversion from TTIP to TiO_2 monomers through thermal decomposition, hydrolysis, or high temperature oxidation reactions. More recent studies have been able to identify stable intermediates of Ti-containing monomers, most commonly $\text{Ti}(\text{OH})_4$. However, no larger Ti cluster formation mechanisms or interactions between these monomers have been tracked. Results from measured mass spectra and mass defect plots show that for positively charged clusters, oxidation of higher molecular weight metalorganic species occurs during clustering of larger intermediate organometallic species. For negatively charged ions, NO_x formation pathways plays an important mechanism for the formation of TiO_2 .

3.2 Introduction

We poorly understand the mechanisms of initial particle growth as gaseous precursors convert to stable clusters. These mechanisms are especially important for the combustion synthesis of nanoparticles such as TiO_2 , which is most commonly manufactured through this route for use as a photocatalyst, semiconductor, or pigment. Although significant work has focused on atmospheric nucleation mechanisms, aerosol nucleation and growth in flames occurs at high temperatures (up to 2400K) and has extremely high rates of production making it difficult to control. Early stage mechanisms are critical in accurately modeling overall particle growth, especially for multicomponent systems where such mechanisms remain largely a mystery. It is well understood that particle growth beyond 2 nm in flames occurs through coagulation, condensation, and sintering. Applications of combustion synthesis to novel materials, such as battery anodes, catalysts, and solar cells have been difficult to scale up since we still cannot accurately model particle growth from first principles and must rely on empirical approaches. In the case of combustion synthesis of metal oxides, calculations based on classical nucleation theory predict that the critical monomer size is a single monomer of TiO_2 [1]. The validity of this assumption has yet to be thoroughly tested.

Various approaches have been developed to track particle formation and growth in flames. For example, laser-induced breakdown spectroscopy (LIBS) is a non-invasive method for *in situ* diagnostics both for undoped [2] and doped metal oxide nanomaterials in flames [3] which can differentiate between particle and gas phase atoms. Fourier transform infrared spectroscopy (FTIR) has been successfully applied to premixed flames to study the synthesis of iron oxide-silica composites and compared to aerosol growth models [4, 5]. However, these techniques do not provide sufficient detail regarding the chemistry of particle formation. Molecular beam mass

spectrometry (MBMS) is the most widely used direct sampling technique for mapping the chemistry and kinetics of hydrocarbon combustion [6] and titanium (IV) isopropoxide (TTIP) decomposition in hydrogen flames [7], but this technique is unable to provide size resolved chemistry or track larger cluster formation mechanisms.

Electrical mobility measurements, a well-established method of measuring particle size distributions, have allowed detailed measurements of particle growth and coagulation. However, resolution limitations and diffusion losses below 2 nm make the technique unsuitable for tracking smaller clusters [8]. Significant advances in high resolution (HR) differential mobility analyzers (DMAs) have allowed measuring and tracking cluster growth during the combustion synthesis of TiO_2 for the first time [9]. HR DMAs have been applied to studying mass-mobility relationships below 3nm experimentally [10] along with direct comparisons to computational predictions of electrical mobility [11]. These techniques can now provide insights into cluster formation mechanisms in flames. Advancements in atmospheric pressure interface time of flight mass spectrometers (APi-TOF) have allowed for high resolution identification and detection of ions directly at atmospheric pressure [12], with applications in areas such as the study of studying sulfuric acid interactions with large oxidized organic molecules [13].

This paper is devoted to understanding the initial stages of metal oxide particle formation in a flat flame aerosol reactor (FFAR), as measured by an APi-TOF. Measurements are taken through a venturi dilution probe which draws a sample of charged clusters of metal oxides into the APi-TOF. Hypothesized pathways and cluster formation mechanisms are presented for the first time on the initial stages of particle formation in the combustion synthesis of TiO_2 .

3.3 Material and Methods

3.3.1 Flame aerosol reactor

A premixed flat flame aerosol reactor (FFAR) generated clusters of TiO₂ (Figure 3.1). Details of the FFAR are described in previous work [9]. Briefly, a radially symmetric flat flame was stabilized over a 1.91 cm diameter honeycomb burner head inside a concentric 2.54 cm diameter tube which provided a sheath flow of N₂ gas (>99.95%, Linde AG). Gas flow rates for methane (>99.95%, Linde AG), oxygen (>99.95%, Linde AG), nitrogen carrier gas and TTIP precursor (Sigma Aldrich Inc., >97%) were metered by mass flow controllers (MKS Instruments). A stainless steel feed tube from the precursor bubbler was heated to prevent precursor wall condensation. A sealed glass bubbler (MDC Vacuum Products, LLC) supplied TTIP precursor to the premixed flame using nitrogen as the carrier gas. The loading rate was calculated based on relationships from Siefert and Griffin [14]. The precursor molar feed rate ranged from 0.06 mmol/hr to 0.30 mmol/hr. Flow conditions for the FFAR are listed in Table 3.1. All of the gases were premixed prior to entering the burner head creating a stable flame sheet at the burner-head.

Table 3.1: Properties of the methane-air flat flame aerosol reactor

Property	Value
Methane flow rate	1.0 lpm
Oxygen flow rate	2.85 lpm
Nitrogen flow rate	8.0 lpm
Dilution ratio	120:1
Precursor loading rates	0.07- 0.22 mmol/hr
Flame diameter	19.05 cm

3.3.2 API-TOF MS measurements of sub 2nm clusters in a flame aerosol reactor

To quench further chemical reactions and particle growth in the flame, a venture dilution probe using nitrogen as a dilution gas at a dilution ratio of 120:1 (dilution sample flow:sample flow) was used. Flame-generated clusters were sampled 5mm above the burner head. The dilution flow rate was maintained at 50 lpm by a mass flow controller (MKS Instruments). Natively charged flame ions and clusters were injected into an API-TOF mass spectrometer (Tofwerk AG, Thun) where the inlet flow rate was 0.81 lpm and the excess flow was exhausted. The API-TOF did not supply any additional charging, so only natively charged clusters were sampled into the mass analyzer. This system has very high sensitivity and can measure both positive and negative ions. The resolving power is 3000 Da/Da ($M/\Delta M$), with mass accuracy better than 20 ppm with a detection range of up to 2500 Da. Further details of this instrument can be found in previous publications [15, 16]. Calibration was performed using NO_3^- (61.9884 Da), $\text{HNO}_3 \text{NO}_3^-$ (124.9835 Da) and $\text{TiO}_2 (\text{NO}_3)_3^-$ (265.9012 Da) for negative clusters. Positively charged clusters were calibrated using NH_4^+ (18.0344 Da) and $\text{Ti}(\text{OH})_4\text{H}^+$ (116.9662 Da). Data processing was done using a MATLAB program developed by Junninen et al. [15].

3.3.3 Experimental plan

Table 3.2 presents the experimental plan. Four different tests were performed, starting with the measurement of background ions in the methane-air flat flame without any precursor (Test 1). Following Test 1, TTIP precursor was added to the flat flame to measure Ti clusters for both positively charged ions (Test 2) and negatively charged ions (Test 3). Finally, the effect of loading rate was studied by adjusting the feed rate of the precursor (Test 4).

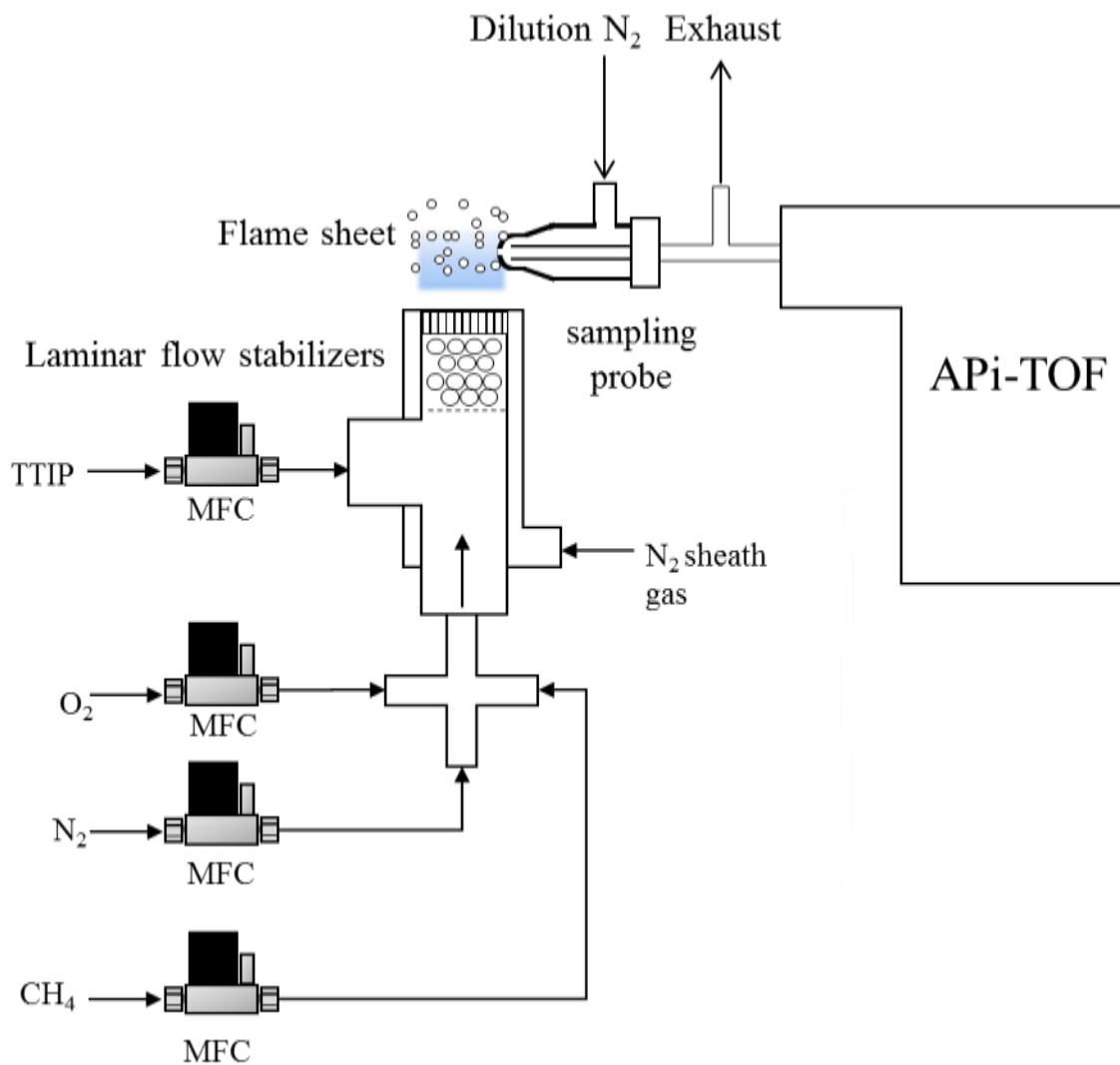


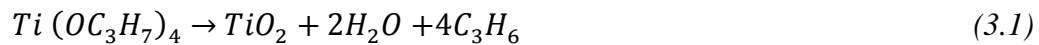
Figure 3.1: Experimental set-up of the flat flame aerosol reactor for measurement of natively charged clusters in an atmospheric-pressure-interface time-of-flight mass spectrometer

Table 3.2: Experimental plan for measuring cluster formation pathways

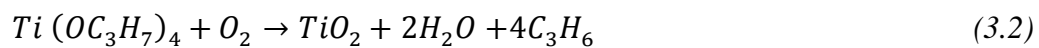
Test #	Objective
1	Measure background natively charged ions in the flame
2	Measure positive mass spectra for TTIP
3	Measure negative mass spectra for TTIP
4	Test the effect of loading rate on mass spectra

3.3.4 Reaction mechanisms of TiO₂ in flames

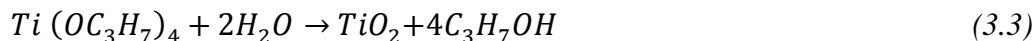
Particle formation of TiO₂ from the decomposition of TTIP is assumed to occur through three possible mechanisms: thermal decomposition, hydrolysis, or oxidation. Although TTIP is a commonly used precursor for the study of TiO₂ combustion synthesis, detailed chemical mechanisms of conversion have only recently been explored [7]. The kinetics of thermal decomposition of TTIP have been measured by Okuyama et al [17]. by assuming the following first order reaction mechanism:



By measuring sub 2nm cluster size distributions with a Half-Mini DMA, revised first order reaction rates were derived assuming the same mechanism [18]. Due to oxygen in methane or hydrogen flames, TTIP oxidation has also been shown:



Finally, water in flames results in rapid hydrolysis of TTIP. Hydrolysis has been hypothesized to be the dominant pathway of TTIP conversion to TiO_2 :



Molecular beam mass spectrometry (MBMS) in a hydrogen flat flame with TTIP precursor addition has provided a more detailed conversion mechanism for the hydrolysis of TTIP to TiO_2 . $Ti(OH)_4$ has been shown to be the most stable intermediate byproduct of hydrolysis [19].

3.4 Results and discussion

3.4.1 Background ions measured in methane air premixed combustion

To study background ions in the flame, positively and negatively charged ions were measured in a premixed fuel lean methane-air flat flame without any precursor addition. The results are displayed in Figure 3.2. Previous studies of ions in flames have focused on lower molecular weight species which have undergone further ionization steps (e.g., electron ionization or vacuum ultraviolet ionization). Recently, HR-DMA's have been used to measure the mobility spectra for natively charged flame ions in a fuel-lean methane-air flat flame, however further steps need to be taken to measure the exact mass of ions [9]. The mass spectra in Figure 3.2 represent natively charged ions sampled from the flame. The peaks from the positively charged mass spectrum are mostly organic radicals commonly measured during methane air combustion, for example, the most prominent peak was measured with an m/z of 124 with probable molecular composition of $C_4H_{14}O_3N^+$. In the case of negatively charged species, the ions were identified as nitrate radicals and nitric acid clusters of NO_3^- , HNO_3^- , NO_3^- , and $H_2NO_3(NO_3^-)_2$, which are all generated through the combustion pathways of NO_x . NO_x is long established as a combustion pollutant playing an important role in emissions from hydrocarbon flames. Three main pathways

of combustion induced formation of NO_x include fuel- NO_x , thermal NO_x and prompt NO_x [20]. Since the fuel and precursor do not contain any nitrogen species and the flame temperature is on the order of 1400-1700K, prompt NO_x is hypothesized likely the primary mechanism of NO_x formation from collisions of N_2 gas molecules with the high concentration of radicals in the flame. Similarly, significant concentrations of NO_x has also been detected in previous studies for premixed $\text{CH}_4/\text{O}_2/\text{N}_2$ flames [21].

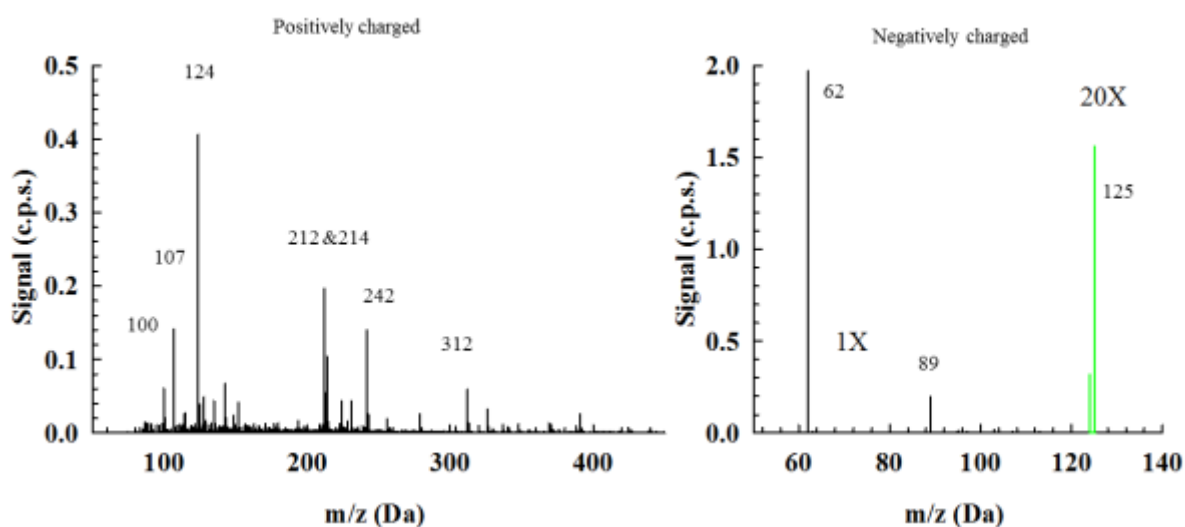


Figure 3.2: Background ions measured in a flame aerosol reactor for naturally charged positive (left) and negative (right) ions, with nominal masses of major peaks labeled. For negatively charged flame clusters, larger peaks were scaled at by multiplying the signal intensity by 20 (20X).

The presence of diverse ion species in flames complicates charging mechanisms as Previous work in studying ions and particle charging mechanisms in flames has relied on Fuch's charging theory [22] or Boltzmann's charging theory [23], which may be too simplified for combustion environments. For example, Fuch's theory assumes a stationary charge state generated

from ions of a single ion mass and mobility. The assumed equilibrium charge fraction in Boltzmann's theory is also not appropriate for small clusters since it fails to consider the difference between the positive and negative ions. Both theories also fail to account for further ionization mechanisms such as chemi-ionization, thus understanding the role of various charging mechanisms will be important for understanding clustering interactions in flames.

3.4.2 Titanium dioxide particle formation during combustion synthesis

The addition of TTIP precursor in the flame resulted in the generation of charged titanium species providing insight into the initial stages of particle formation for TiO_2 during combustion synthesis. Figure 3.3 displays the mass spectra for negatively charged ions, while Figure 3.4 displays the positive ion spectra. Ti contains five naturally occurring stable isotopes: ^{46}Ti (10.8%), ^{47}Ti (9.9%), ^{48}Ti (73.8%), ^{49}Ti (7.5%), ^{50}Ti (7.3%), allowing for the identification of Ti-containing clusters through this isotopic pattern. For the negative ion mass spectra, distinct monomer ions with Ti could be identified as $\text{TiO}_2(\text{NO}_3)_3$ at m/z 266. Additional peaks of TiO_2 with multiple NO_3 species attached were also present in the mass spectra, while Ti species with varying levels of oxidation were also measured in the form of $\text{Ti}_n\text{O}_x\text{N}_y$. Peak assignments for negatively charged Ti clusters, listed in Table 3.3, are a clear indication that flame ions participate in the conversion reactions from TTIP to TiO_2 , with NO_x playing an important role. Here we have provided evidence for the first time that NO_x and Ti species participate in chemical-ionization reactions to form clusters of TiO_2 .

Table 3.3: Proposed molecular compositions for identified peaks in a negative mass spectrum

Negatively Charged Clusters			
Molecular Formula	Exact Mass	Measured Mass	ppm
TiO ₈ N ₂	203.9140	203.914	-1.67
TiO ₉ N ₂	219.9089	219.908	3.78
TiO ₁₀ N ₂	235.9038	235.903	3.31
Ti ₂ O ₈ H ₂ N	239.8745	239.873	2.45
TiO ₂ (NO ₃) ₃	265.9012	265.901	0.88
Ti ₂ O ₁₁ N	285.8430	285.843	1.89
Ti ₂ O ₁₁ CHN	298.8509	298.851	-1.14
Ti ₂ O ₁₂ N ₂	315.8410	315.838	10.60
Ti ₂ O ₁₃ N	317.8329	317.830	9.12
Ti ₃ O ₉ C ₂ H ₅ N	330.8403	330.838	6.95
Ti ₃ O ₁₁ H ₄ C ₂	347.8192	347.819	9.28

For positively charged ions, protonated clusters in the form of Ti(OH)₄H⁺ and Ti(OH)₃H⁺ were identified in addition to TiO(OH)₄⁺ (Figure 3.4). These were the most prominent monomer Ti-containing species in the positive mass spectra, which is in agreement with previous literature, showing titanium hydroxide to be the most stable intermediate from TTIP hydrolysis [19, 24]. Larger peaks could not be identified due to significant isotope overlap and multiple possible molecular compositions at higher masses. The peak assignments contained many possible organic species, thus complicating the positive mass spectra and indicating the incomplete decomposition of TTIP. Furthermore, these intermediates may have interacted with organic radicals and flame ions. Previous studies on flame ions have concluded that chemical ionization mechanisms are important in hydrocarbon flames near the flame sheet and many unburnt hydrocarbons can also contribute to ionization and charging mechanisms [25].

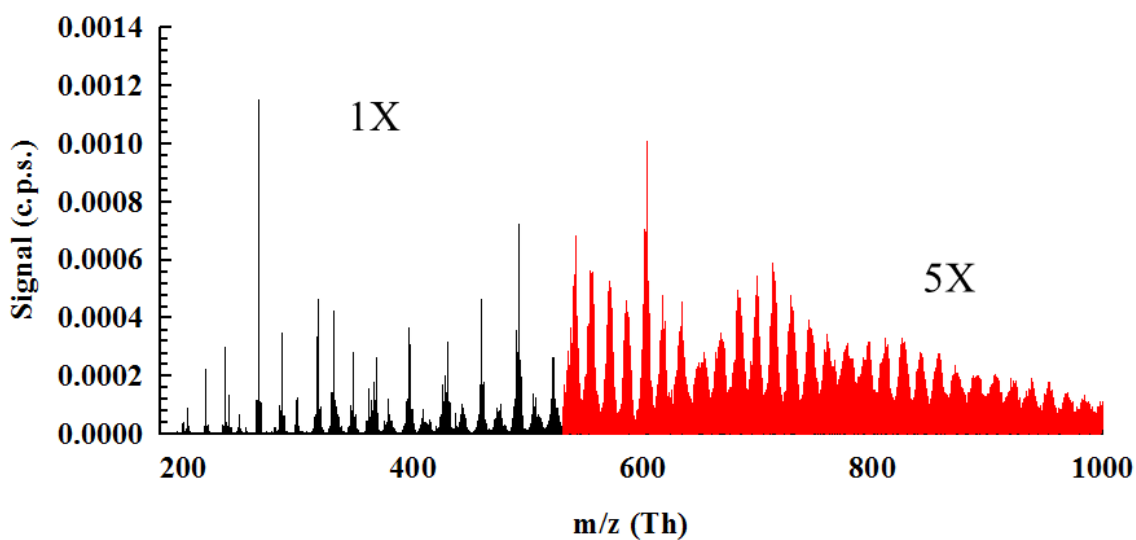
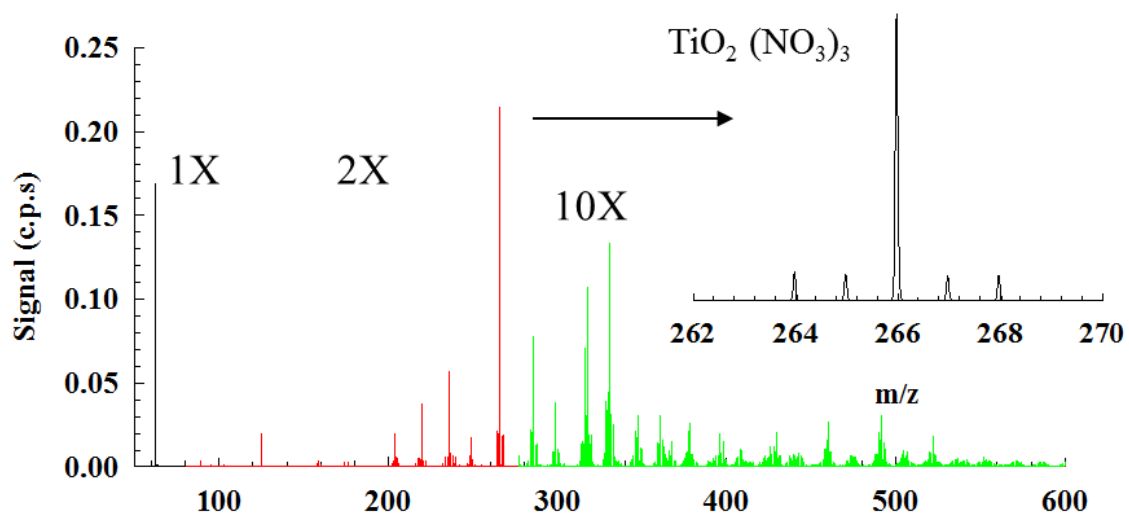


Figure 3.3: Negative TTIP spectra at two different precursor feed rates of 0.07 mmol/hr (top) and 0.15 mmol/hr (bottom). Colored spectra refer to portions of the mass spectra where Signal intensities were multiplied by 2 (2X), 5 (5X) and 10 (X).

Beyond 300 Da, periodic humps with distinct cluster isotope patterns become increasingly prevalent with increasing precursor concentration (Figure 3.4). In this size range, isotopic patterns characteristic of titanium clusters ions begin to overlap, making the spectra complicated to interpret. Previous studies using TOF mass analyzers studying pure TiO₂ nanoparticles have experienced similar issues with peak assignments [26]. Cluster peaks can be grouped together by their isotope patterns. Each cluster is separated by 14 Da, indicating the abstraction of alkyl groups. These periodic peak patterns also show that intermediates from TTIP decomposition may also polymerize or aggregate into larger clusters prior to conversion to pure TiO₂. In Figure 3.4c, beyond 300 Da, these patterns resemble organic cluster formation as observed in previous atmospheric nucleation studies. Organic molecule attachment on the larger Ti clusters further complicates the assignment of mass spectral peaks. There are two potential sources of such organics: Methane combustion has the potential to generate a high concentration of organic radicals, and TTIP is an organometallic precursor with 4 propyl groups attached which can be removed during incomplete decomposition. Due to the high frequency of collisions with other ions in the flame region, clustering interactions between Ti-containing intermediates can result in the larger complex structures in the mass spectrum. Based on the ratios of isotopic peaks to the main peak, we can hypothesize that the clusters contain multiple titanium atoms. Due to isotope peak overlap and the multiple combinations of potential compounds at high mass ranges, exact peak assignments could not be performed, thus mass defect techniques were used to provide further insight into the mass spectra.

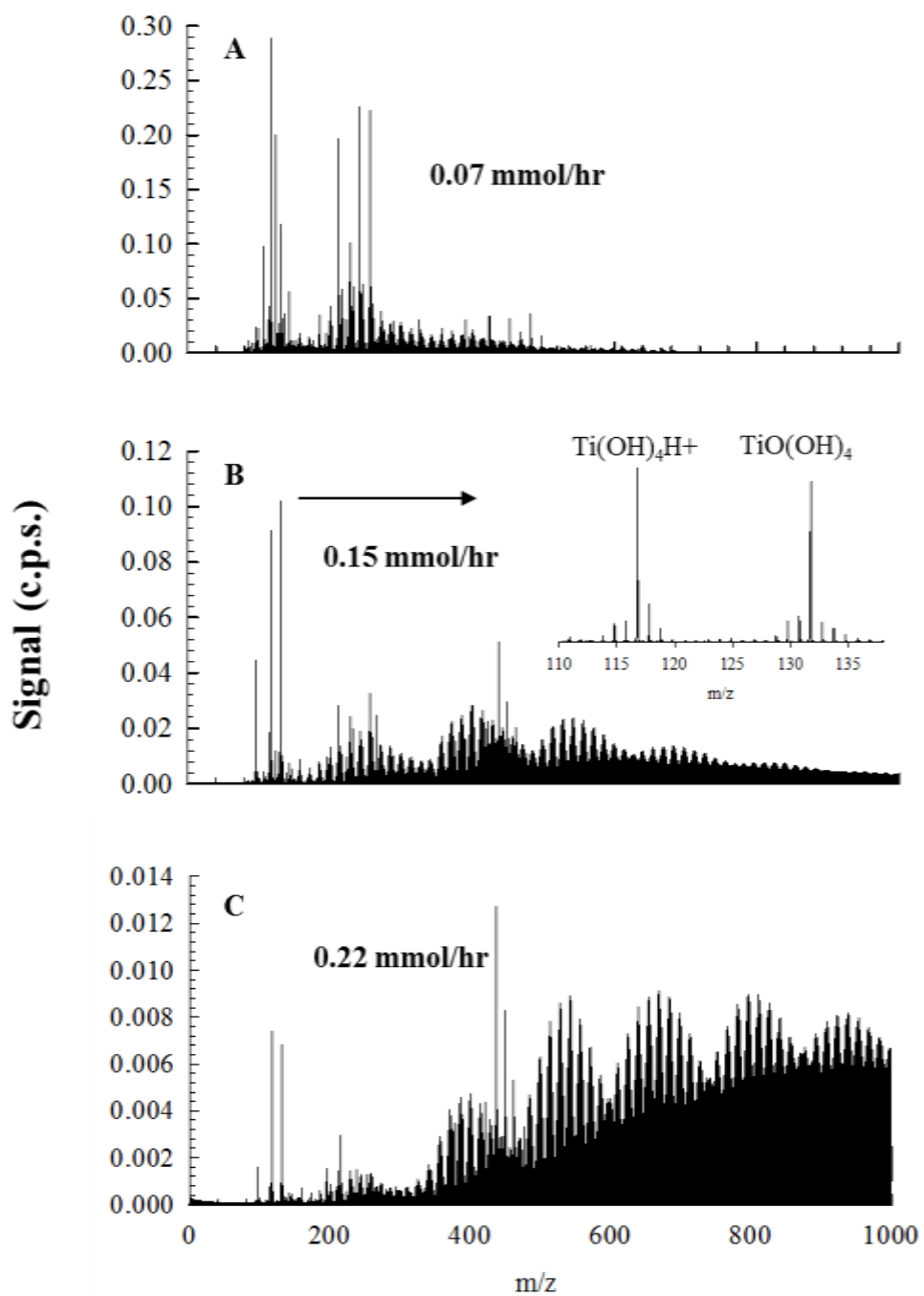


Figure 3.4: Positively charged clusters during the combustion synthesis of TiO₂ at three different loading rates

3.4.3 Mass defect plots

Mass defect plots from the positive and negative mass spectra were constructed from Figure 3.3b and 3.4c to provide another visual basis for analyzing the complex mass spectrum (Figure 3.5). Here a peaks with a signal higher than 0.25 cps were each assigned a calculated mass defect and plotted with the mass defect on the y-axis and isotope mass on the x-axis. A mass defect is defined as the difference between a compound's exact mass and nominal mass. Plotting the mass defect allows for visualization of complex mass spectra and has been successfully applied towards analyzing mass spectra from crude oil [27] and atmospheric organic molecules [13], where similar repeating peak patterns have been observed. In the case of combustion synthesis of TTIP, the mass defect plot spans from positive to negative mass defect ranges, which helps identify the class of compounds in the spectrum. Positive mass defects indicate the presence of organics (e.g. CH₂ has a mass defect of +0.0156), and negative mass defects indicate oxidized species of titanium clusters (e.g., TiO₂ has a mass defect of -0.062).

Figure 3.5a displays several distinct bands for positively charged ions, beginning with a distinct band of ions with positive mass defects. This class of molecules is most likely organic ions which have been formed either through fragmentation of TTIP or from intermediate generated by hydrocarbon combustion. The peak spacing in this band is 14 Da, indicating alkylation chemistry occurring with these organic species. For the first negative defect band, labeled 'Cluster 1', these species are most likely intermediate organometallic dimers, since eight distinct bands ranging from m/z 300-450 and spaced by m/z 16 alludes to oxidation processes.

Furthermore, the overall upward slope of this cluster is characteristic of OH⁻ radical participation. As new band patterns emerge with increasing mass, we hypothesize that each band represents a new group of clusters with an added titanium core. It should be noted that at higher

masses, the mass defect plot distorts to progressively more negative slopes, indicating that the TOF calibration has drifted in this mass range. Further studies will require more sophisticated calibration procedures to ensure accurate peak identification at higher masses. For the negative

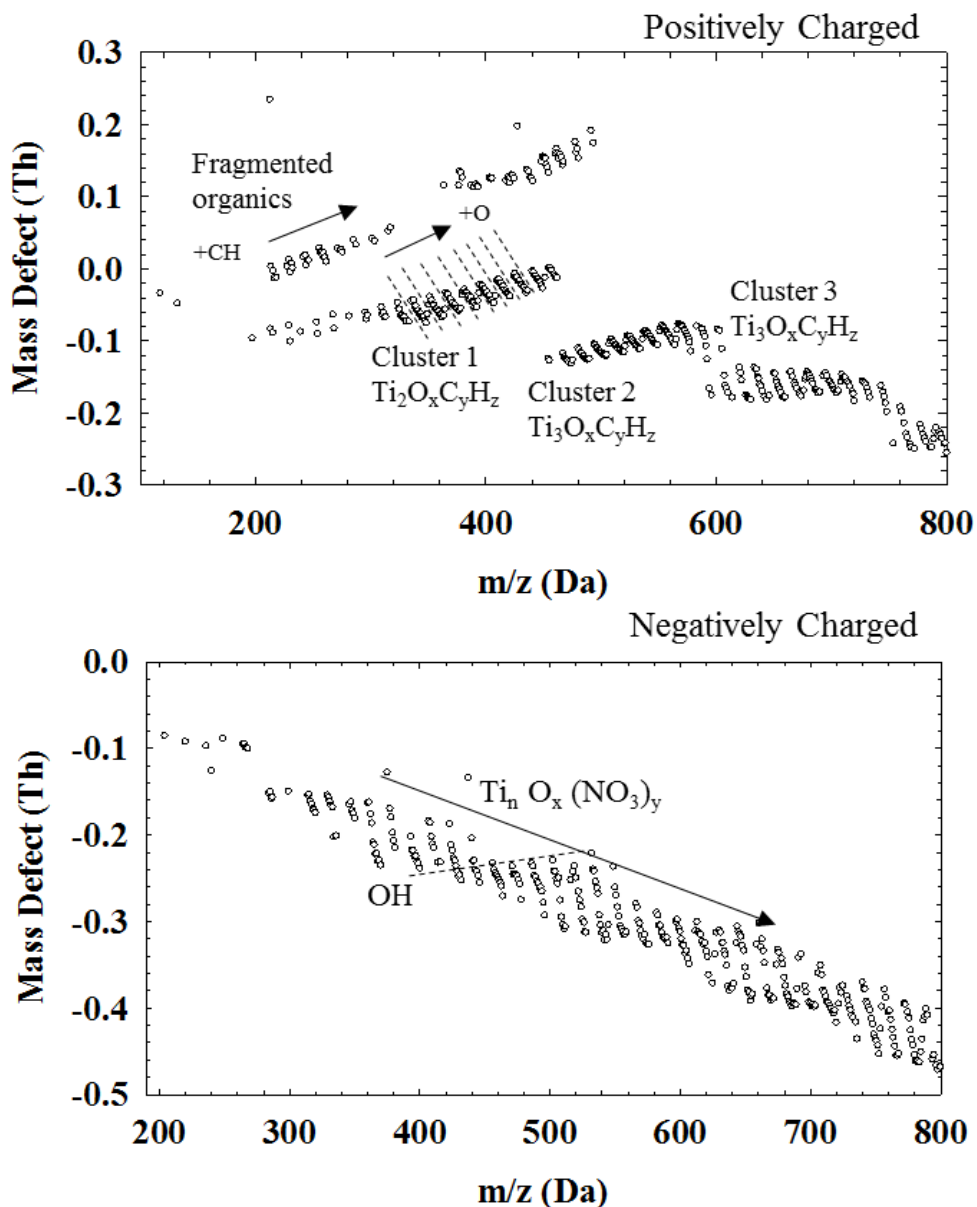


Figure 3.5: Mass defect plots for (a) positively charged ions and (b) negatively charged ions during the combustion synthesis of TiO_2 .

mass defect plot (Figure 3.5b), the spectrum does not have the same distinct groupings of clusters, but the overall negative slope indicates strong clustering interactions of $(\text{TiO}_2)_x (\text{NO}_3)_y$. Identifiable peaks in Figure 3.4 are mostly a class of negatively charged $\text{Ti}_n\text{O}_x\text{N}_y$ clusters. Due to the different possible oxidation states of Ti, the assignment of oxygens to either Ti or N left is ambiguous. However, the band structure spacing as seen in the positive mass defect plot with spacing's of 16 Da also indicate the addition of O to $\text{Ti}_n\text{O}_x\text{N}_y$ complexes, providing further evidence for strong clustering interactions between NO_x and Ti species. This finding is the first clear indication of TTIP chemical ionization occurring in flames through NO_x interactions, whereas previous studies have mostly assumed diffusion charging and thermionic ionization to be the principle mechanisms of charging. A dashed line with a slight upward slope also highlights that OH radical-driven interactions participated in the growth of Ti clusters. Further studies are needed to fully understand the contribution of chemi-ionization pathways during combustion synthesis.

Based on the data presented in Figures 3.3-3.5, we can see that collisional growth of TiO_2 clusters at the initial stages of particle formation may not be a suitable assumption to capture the growth mechanisms. Previous studies have concluded that $\text{Ti}(\text{OH})_4$ is the most thermodynamically stable monomer. Based on positive mass spectra we can draw similar conclusions since $\text{Ti}(\text{OH})_4$ and $\text{TiO}(\text{OH})_4$ had the highest intensities. Negative mass spectra revealed the presence of $\text{Ti}_n\text{O}_x\text{N}_y$ species demonstrating the importance of chemical ionization. For example single monomer ions of Ti contained varying number of O atoms. Even for dimers and trimers of Ti, the ratio of Ti to O varied. Nevertheless many other stable intermediates were also measured, and clusters containing more than a single Ti atom were detected in significant concentrations. Thus there is a need to further understand how these larger clusters form and how they affect downstream

pathways. It should be noted that sampled clusters may undergo collisions with the dilution gas, thus charge transfer interactions may also occur during the sampling process. Great effort was made to minimize this effect by keeping very high dilution ratios and short residence times. Future studies should also focus on system specific pathways by studying the effect of different flame structures, fuel types, and carrier gases.

3.5 Conclusions

Through the measurement of natively charged clusters during the combustion synthesis of TiO_2 we have studied the clustering interactions between intermediate species of TTIP decomposition in a methane-air flat flame towards the formation of TiO_2 nanoparticles. Measurements were made using an atmospheric pressure interface-time of flight mass spectrometer. Results show newly detected negatively charged species which include NO_x species attached to titanium species with different oxidation states and stable positive monomers of $\text{Ti}(\text{OH})_4$ and $\text{TiO}(\text{OH})_4$. Evidence from these measurements indicate the importance for intermediate clustering interactions which may be specific to precursor chemistry of flame condition. Through these series of measurements we have observed several new phenomena: 1) NO_x plays a strong role in clustering interactions with Ti species of varying oxidation states; 2) Intermediate organic species in the form of $\text{Ti}_n\text{O}_x\text{C}_y\text{H}_z$ may form larger complexes prior to complete conversion to TTIP; 3) $\text{Ti}(\text{OH})_4$, $\text{TiO}(\text{OH})_4$, and $\text{TiO}_2(\text{NO}_3)_3^-$ are the most stable monomeric Ti species that are natively charged; 4) Chemi-ionization can play a principle role in the initial stages of particle formation.

3.6 References

- [1] G.D. Ulrich, Theory of particle formation and growth in oxide synthesis flames, *Combustion Science and Technology*, 4 (1971) 47-57.
- [2] Y.Y. Zhang, G. Xiong, S.Q. Li, Z.Z. Dong, S.G. Buckley, S.D. Tse, Novel low-intensity phase-selective laser-induced breakdown spectroscopy of TiO₂ nanoparticle aerosols during flame synthesis, *Combustion and Flame*, 160 (2013) 725-733.
- [3] Y. Ren, Y. Zhang, S. Li, C.K. Law, Doping mechanism of Vanadia/Titania nanoparticles in flame synthesis by a novel optical spectroscopy technique, *Proceedings of the Combustion Institute*, 35 (2015) 2283-2289.
- [4] P. Biswas, C.Y. Wu, M.R. Zachariah, B. McMillin, Characterization of iron oxide-silica nanocomposites in flames .2. Comparison of discrete-sectional model predictions to experimental data, *Journal of Materials Research*, 12 (1997) 714-723.
- [5] B.K. McMillin, P. Biswas, M.R. Zachariah, In situ characterization of vapor phase growth of iron oxide-silica nanocomposites .1. 2-D planar laser-induced fluorescence and Mie imaging, *Journal of Materials Research*, 11 (1996) 1552-1561.
- [6] N. Hansen, T.A. Cool, P.R. Westmoreland, K. Kohse-Höinghaus, Recent contributions of flame-sampling molecular-beam mass spectrometry to a fundamental understanding of combustion chemistry, *Progress in Energy and Combustion Science*, 35 (2009) 168-191.
- [7] A.G. Shmakov, O.P. Korobeinichev, D.A. Knyazkov, A.A. Paletsky, R.A. Maksutov, I.E. Gerasimov, T.A. Bolshova, V.G. Kiselev, N.P. Gritsan, Combustion chemistry of Ti(OC₃H₇)₄ in premixed flat burner-stabilized H₂/O₂/Ar flame at 1 atm, *Proceedings of the Combustion Institute*, 34 (2013) 1143-1149.
- [8] Y. Wang, J. Fang, M. Attoui, T.S. Chadha, W.-N. Wang, P. Biswas, Application of Half Mini DMA for sub 2 nm particle size distribution measurement in an electrospray and a flame aerosol reactor, *J. Aerosol. Sci.*, 71 (2014) 52-64.
- [9] J.X. Fang, Y. Wang, M. Attoui, T.S. Chadha, J.R. Ray, W.N. Wang, Y.S. Jun, P. Biswas, Measurement of Sub-2 nm Clusters of Pristine and Composite Metal Oxides during Nanomaterial Synthesis in Flame Aerosol Reactors, *Anal. Chem.*, 86 (2014) 7523-7529.
- [10] C. Larriba, C.J. Hogan Jr, M. Attoui, R. Borrajo, J.F. Garcia, J.F. de la Mora, The mobility-volume relationship below 3.0 nm examined by tandem mobility-mass measurement, *Aerosol Sci. Technol.*, 45 (2011) 453-467.

- [11] C. Larriba, C.J. Hogan Jr, Ion mobilities in diatomic gases: measurement versus prediction with non-specular scattering models, *The Journal of Physical Chemistry A*, 117 (2013) 3887-3901.
- [12] H. Junninen, M. Ehn, T. Petäjä, L. Luosujärvi, T. Kotiaho, R. Kostianen, U. Rohner, M. Gonin, K. Fuhrer, M. Kulmala, D.R. Worsnop, A high-resolution mass spectrometer to measure atmospheric ion composition, *Atmos. Meas. Tech.*, 3 (2010) 1039-1053.
- [13] S. Schobesberger, H. Junninen, F. Bianchi, G. Lönn, M. Ehn, K. Lehtipalo, J. Dommen, S. Ehrhart, I.K. Ortega, A. Franchin, Molecular understanding of atmospheric particle formation from sulfuric acid and large oxidized organic molecules, *Proceedings of the National Academy of Sciences*, 110 (2013) 17223-17228.
- [14] K. Siefert, G. Griffin, Growth kinetics of CVD TiO₂: influence of carrier gas, *Journal of The Electrochemical Society*, 137 (1990) 1206-1208.
- [15] H. Junninen, M. Ehn, T. Petäjä, L. Luosujärvi, T. Kotiaho, R. Kostianen, U. Rohner, M. Gonin, K. Fuhrer, M. Kulmala, A high-resolution mass spectrometer to measure atmospheric ion composition, *Atmospheric Measurement Techniques*, 3 (2010) 1039-1053.
- [16] M. Ehn, J.A. Thornton, E. Kleist, M. Sipila, H. Junninen, I. Pullinen, M. Springer, F. Rubach, R. Tillmann, B. Lee, F. Lopez-Hilfiker, S. Andres, I.-H. Acir, M. Rissanen, T. Jokinen, S. Schobesberger, J. Kangasluoma, J. Kontkanen, T. Nieminen, T. Kurten, L.B. Nielsen, S. Jorgensen, H.G. Kjaergaard, M. Canagaratna, M.D. Maso, T. Berndt, T. Petaja, A. Wahner, V.-M. Kerminen, M. Kulmala, D.R. Worsnop, J. Wildt, T.F. Mentel, A large source of low-volatility secondary organic aerosol, *Nature*, 506 (2014) 476-479.
- [17] K. Okuyama, R. Ushio, Y. Kousaka, R.C. Flagan, J.H. Seinfeld, Particle generation in a chemical vapor deposition process with seed particles, *AIChE journal*, 36 (1990) 409-419.
- [18] Y. Wang, P. Liu, J. Fang, W.-N. Wang, P. Biswas, Kinetics of sub-2 nm TiO₂ particle formation in an aerosol reactor during thermal decomposition of titanium tetraisopropoxide, *J Nanopart Res*, 17 (2015) 1-13.
- [19] A. Shmakov, O. Korobeinichev, D. Knyazkov, A. Paletsky, R. Maksutov, I. Gerasimov, T. Bolshova, V. Kiselev, N. Gritsan, Combustion chemistry of Ti (OC₃H₇)₄ in premixed flat burner-stabilized H₂/O₂/Ar flame at 1atm, *Proceedings of the Combustion Institute*, 34 (2013) 1143-1149.
- [20] D.G. Nicol, R.C. Steele, N.M. Marinov, P.C. Malte, The Importance of the Nitrous Oxide Pathway to NO_x in Lean-Premixed Combustion, *Journal of Engineering for Gas Turbines and Power*, 117 (1995) 100-111.
- [21] G.B. Debrou, J.M. Goodings, D.K. Bohme, Flame-ion Probe Intermediates Leading to NO_x in CH₄-O₂-N₂ Flames, *Combustion and Flame*, 39 (1980) 1-19.

- [22] J. Jiang, M.H. Lee, P. Biswas, Model for nanoparticle charging by diffusion, direct photoionization, and thermionization mechanisms, *J. Electrostat.*, 65 (2007) 209-220.
- [23] D. Keefe, P.J. Nolan, T.A. Rich, Charge Equilibrium in Aerosols According to the Boltzmann Law, *Proceedings of the Royal Irish Academy. Section A: Mathematical and Physical Sciences*, 60 (1959) 27-45.
- [24] P. Buerger, D. Nurkowski, J. Akroyd, S. Mosbach, M. Kraft, First-Principles Thermochemistry for the Thermal Decomposition of Titanium Tetraisopropoxide, *The Journal of Physical Chemistry A*, 119 (2015) 8376-8387.
- [25] A.B. Fialkov, Investigations on ions in flames, *Progress in Energy and Combustion Science*, 23 (1997) 399-528.
- [26] B. Guan, W. Lu, J. Fang, R.B. Cole, Characterization of synthesized titanium oxide nanoclusters by MALDI-TOF mass spectrometry, *Journal of the American Society for Mass Spectrometry*, 18 (2007) 517-524.
- [27] C.A. Hughey, C.L. Hendrickson, R.P. Rodgers, A.G. Marshall, K. Qian, Kendrick Mass Defect Spectrum: A Compact Visual Analysis for Ultrahigh-Resolution Broadband Mass Spectra, *Anal. Chem.*, 73 (2001) 4676-4681.

4. The Initial Stages of Multicomponent Particle Formation During the Combustion Synthesis of Mixed SiO₂/TiO₂

4.1 Abstract

The ability to properly scale the synthesis of advanced materials through combustion synthesis routes is limited by our lack of knowledge regarding the initial stages of particle formation. In flame aerosol reactors, the high temperatures, fast reaction rates, and flame chemistry can all play a critical role in determining the properties of the resulting nanomaterials. In particular, multicomponent systems pose a unique challenge as most studies rely on empirical approaches towards designing advanced composite materials. The lack of predictive capabilities can be attributed to a lack of data on particle inception and growth below 2nm. Here we present measurements for the initial stages of particle formation during the combustion synthesis of SiO₂ and composite SiO₂/TiO₂ using an atmospheric pressure inlet time-of-flight mass spectrometer. Both positively and negatively charged clusters can be measured and results show the presence of silicic acid species which grow through dehydration, hydrogen abstraction, and interactions with hydroxyl radicals. In the case of composite SiO₂/TiO₂ particle formation, new molecular species containing Ti atoms emerge. Tandem ion mobility mass spectrometry provided further insight into the size resolved chemistry of particle formation to reveal that at each cluster size, further hydroxyl driven reactions take place. From this we can conclude that previous assumptions on collisional growth from simple monomer species of SiO₂ and TiO₂ does not sufficiently describe the collisional growth mechanisms for particle growth below 2 nm.

4.2 Introduction

Combustion synthesis is a versatile technique for making advanced nanomaterials such as alumina, silica, titania, and other metal oxides. At industrial scales, utilization of combustion synthesis poses the advantages of large production rates, high purity, and low waste generation. More specifically, silica and titania nanoparticles synthesized through this route have found applications for use as hydrophobic coatings, pigments, and catalysts. Further interest towards functional materials have resulted in a pushed towards medical applications, but require the ability to carefully control the size, shape, and surface properties[1]. Thus successful application of this technology requires an adequate degree of tailoring and control in regards to nanoparticle properties which often requires doping. Doping during combustion synthesis has been limited in scalability due to difficulties in preventing phase segregation and controlling material properties such as crystal structure and particle size. A more detailed understanding of particle formation pathways, beginning with the initial stages, for composite nanoparticles synthesized via combustion synthesis will be critical in the successful application of this technology.

Previous studies on doped systems have been able to successfully synthesize composite silica-titania nanomaterials. For example, Ehrman et al. examined the properties of binary $\text{TiO}_2/\text{SiO}_2$ systems while carefully studying the conditions for phase segregation [2]. In addition, the prevention of phase segregation could be achieved by carefully controlling the downstream conditions of the flame through dilution quenching [3]. More advanced nanostructures of TiO_2 nanoparticles have been able to add coatings of silica [4], noble metal decorations [5] and doping with copper [6]. Rapid coating of paper board with binary $\text{TiO}_2\text{-SiO}_2$ has been demonstrated through roll to roll processing to achieve water resistance [7].

Metal oxide nanomaterials exhibit many useful photocatalytic properties allowing for their application in a number of areas. With proper control, the addition of dopants can result in enhanced performance for catalysis [8] and bacterial inactivation [9]. Challenges for achieving scalability for these applications include the ability to control new nanoparticle formation in flame aerosol reactors. This stems from a lack of understanding for the initial stages of particle formation. Despite the significant effort placed on properly designing doped nanomaterials, successful industrial production is limited by a lack of predictive capabilities for modeling flame aerosol reactors for scale up.

Titania and silica particle formation mechanisms have been studied independently using the precursors of titanium tetraisopropoxide (TTIP) and tetraethylorthosilane (TEOS). These precursors are commonly used to for the combustion synthesis of nanoparticles. In the case of silica, conversion from precursor molecules to silica nanoparticles has often assumed simplified global mechanisms through the decomposition of gaseous precursors to stable SiO_2 monomers.



Under classical nucleation theory, the critical particle size for a stable metal oxide seed particle is below the mass based particle diameter of a single metal oxide molecule. Thus studies have assumed that the critical cluster size for a stable monomer is a single metal oxide molecule while further growth is assumed to occur through collisions of these monomers. Recently, theoretical modeling has yielded more detailed pathways of TEOS decomposition to silica, and have demonstrated the importance of intermediate species towards the conversion of TEOS to SiO_2 . Such intermediate are formed through de-methylation, de-ethylation, demethylation and

disproportionation, and de-ethylation and dehydration pathways [10]. Similar studies have examined TTIP decomposition using statistical thermodynamics, quantum chemistry, and equilibrium composition analysis with agreement with experimental results [11]. Although recent work has mapped out such pathways in great detail, there is a lack of experimental validation at the molecular level for cluster growth.

The goal of this study is to measure cluster formation mechanisms for multicomponent systems of TiO_2 and SiO_2 in a flame aerosol reactor. The chemistry of decomposition for both of these precursors has been well studied thus providing a good basis for understanding the initial stages of mixed oxide particle formation. Previous studies have only focused on conversion mechanism from precursors to stable monomers but have failed to take into account how these byproducts may interact with one another to grow into stable nanoparticles. By using an atmospheric pressure interface time-of-flight (APi-TOF) mass spectrometer, we measure natively charged clusters to infer their chemical composition and track their growth mechanisms.

4.3 Material and Methods

Single component SiO_2 and multicomponent $\text{SiO}_2/\text{TiO}_2$ clusters were generated using a premixed methane air flat flame aerosol reactor [12]. Figure 4.1 displays the experimental setup where the methane fuel (>99.95%, Linde AG), Oxygen (>99.95%, Linde AG), and nitrogen carrier gas (>99.95%, Linde AG), and gaseous precursor were premixed and stabilized over a 1.91 cm diameter flat flame burner head. A sheath flow of nitrogen (>99.95%, Linde AG) gas was also provided with a concentric outer tube of 2.54 cm to shield the flame from entraining excess air. Titanium (IV) isopropoxide (TTIP, >97%, Sigma Aldrich) and tetraethylorthosilicate (TEOS, >97%, Sigma Aldrich) precursors were delivered using a glass sealed bubbler (MDC Vacuum Products, LLC) while nitrogen (>99.95%, Linde AG) was used as the carrier gas. All gas flow

rates were controlled by mass flow controllers (MKS Instruments). Precursor loading rates were calculated using vapor pressure data available for TTIP [13] and TEOS [14]. Details on flow conditions are provided in Table 4.1.

Table 4.1: Premixed flame aerosol reactor parameters and operating conditions

Property	Value
Methane flow rate	1.0 lpm
Oxygen flow rate	2.85 lpm
Nitrogen flow rate	8.0 lpm
Sampling probe dilution ratio	120:1
Flame diameter	19.05 cm
TEOS precursor feed rates	0.08-1.97 mmol/hr
TTIP precursor feed rate	0-0.86 mmol/hr

The initial stages of nanoparticle formation during combustion synthesis were measured by an atmospheric-pressure interface time-of-flight (APi-TOF) mass-spectrometer (TOFWERK AG, Thun). Flame generated clusters were sampled using a venturi dilution probe to rapidly quench further collisional growth and chemical reactions. The gas dilution ratio was 120:1 with a dilution flow of 50 lpm. Excess flow was exhausted while a portion of the diluted sample was directly injected into the entrance of the APi-TOF mass spectrometer with an inlet flow rate of 0.81 lpm, only natively charged clusters were measured and no additional ionization was added to the system. The APi-TOF had a resolution of 3000 Da/Da ($M/\Delta M$) with a mass accuracy of 20 ppm and a detection range of up to 2500 Da. Calibration of mass spectra for negatively charged clusters was performed using nitrate radical and nitric acid clusters of NO_3^- (61.9883 Da), $\text{HNO}_3\text{NO}_3^-$

(124.9835 Da), and $(\text{HNO}_3)_2\text{NO}_3^-$. Positive clusters were calibrated using $\text{Si}(\text{OH})_4\text{H}^+$ ($m/z=96.9957$) and $\text{C}_8\text{H}_{12}\text{O}^+$ ($m/z=124.1803$). Mass spectra was analyzed using a MATLAB program previously developed for high resolution mass spectrometers [15].

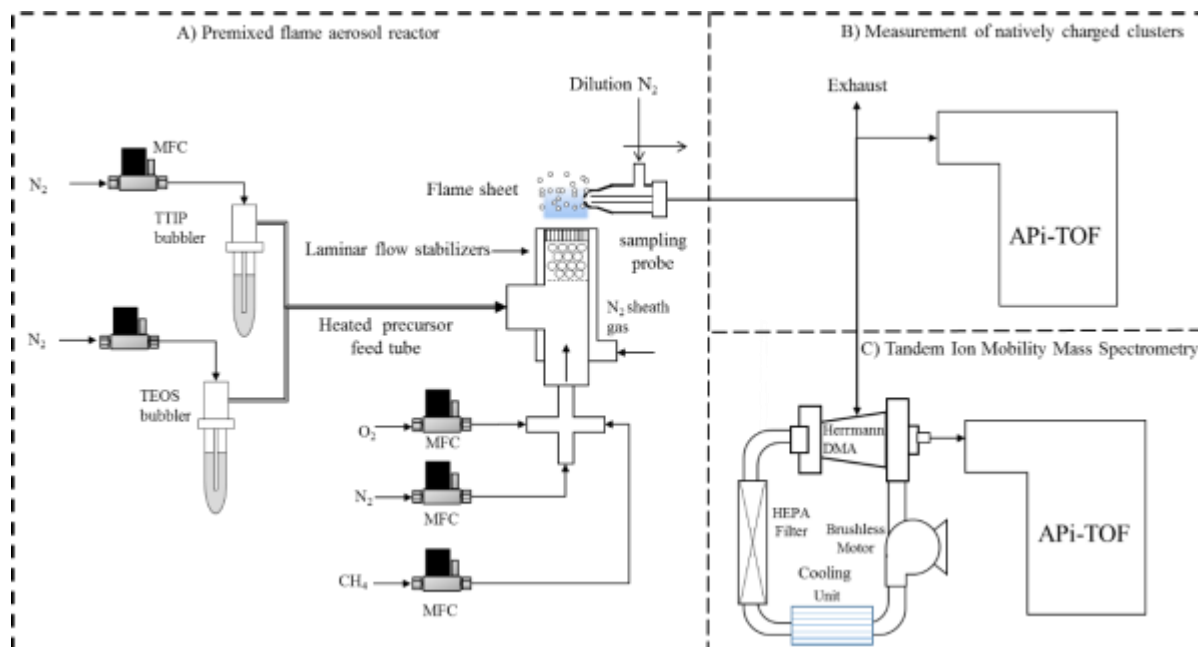


Figure 4.1: Experimental setup for the combustion synthesis of SiO_2 and TiO_2 in a premixed flat flame aerosol reactor along with the measurement of charged clusters using an atmospheric-pressure-inlet time-of-flight (APi-TOF) mass spectrometer.

4.3.1 Size resolved chemistry with tandem ion mobility spectrometry – mass spectrometry (IMS-MS)

Tandem ion mobility mass spectrometry was implemented to classify sub 2 nm particles with high resolution by adding a Herrmann-type Differential Mobility Analyzer (DMA) upstream of

the API-TOF [16]. The DMA allows for the classification of clusters based on their electrical mobility (Z) ranging from 7.5-0.1Vs/cm². A closed loop configuration for the DMA was used to maintain a balanced flow rate of 10 lpm for the inlet and outlet of the DMA. Recirculating room air was used while the flow rate for the DMA was maintained by an inline DC brushless blower (DOMEL Inc.) operated with a flow rate above 500 lpm. The precise flow rate was obtained through calibration by electrospraying a mobility standard of 200 μ M tetraheptylammonium bromide solution (99.9%, Sigma-Aldrich) diluted in methanol [17]. In order to remove any excess nanoparticles and contaminants, an in line HEPA filter was added to the recirculating sheath flow. The mobility spectra was obtained by scanning the DMA voltage using a high voltage source (Spellman Inc.) which was controlled using LabView with a voltage step of 3V with a 1s step time. The signal was measured both by a faraday-cage electrometer (Model 3068B, TSI Inc.) and by injecting the classified ions into the inlet of the API-TOF mass spectrometer allowing for the measurement of the molecular mass for the classified ions.

4.3.2 Experimental plan

A test plan is presented in Table 4.2 for examining multicomponent cluster formation mechanisms. Test 1 will measure the mass spectra for natively charged single component SiO₂ clusters by only adding a TEOS precursor into the FLAR. Test 2 will examine multicomponent systems with the addition of both TTIP and TEOS precursor for TiO₂/SiO₂ nanoparticle synthesis. Finally test 3 will examine the size resolved chemistry of cluster formation during the initial stages of nanoparticle formation with tandem ion mobility mass spectrometry.

Table 4.2: Experimental plan

Test #	Objective	APi-TOF mass spectrometer	Differential Mobility Analyzer	TEOS precursor addition	TTIP precursor addition
1	Measure natively charged clusters for pure SiO ₂ particle formation	✓	✗	✓	✗
2	Measure mixed TiO ₂ /SiO ₂ composite nanoparticle formation at a precursor ratio of 1:1	✓	✗	✓	✓
3	Examine size resolved chemistry in a tandem DMA-MS system	✓	✓	✓	✓

4.4 Results and discussion

4.4.1 Single component particle growth mechanisms.

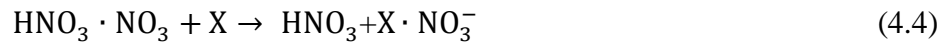
Molecular species of natively charged clusters generated during the combustion synthesis of SiO₂ were measured in an APi-TOF Mass spectrometer. Measuring natively charged clusters allows for the direct observation of new particle formation during combustion synthesis. Figure 4.2 shows representative mass spectra for both positively and negatively charged clusters from the particle formation of SiO₂. Si species could be identified based upon three naturally occurring isotopes of Silicon: ²⁸Si (92.2%), ²⁹Si (4.6%), and ³⁰Si (3.1%). By examining the charged cluster mass and their isotope patterns, we can begin to study new particle inception and how these particles grow beyond monomeric species. There are noticeable difference in spectra patters for positively (Figure 4.2a) and negatively charged (Figure 4.2b) clusters. Certain peaks could be identified and their proposed molecular composition and their molecular weight is listed in Table 4.3.

In the case of positively charged clusters, the highest intensity peaks in the positive mass spectra are protonated silicic acid ($\text{Si}(\text{OH})_4\text{H}^+$, $m/z=96.9957$ Da), protonated TEOS monomers ($\text{Si}(\text{OC}_2\text{H}_5)_4\text{H}^+$ $m/z=209.1204$ Da), and protonated TEOS dimers ($\text{Si}_2(\text{OC}_2\text{H}_5)_8\text{H}^+$, $m/z=417.2340$ Da). The high signal intensity suggests that these three peaks represent some of the more stable compounds present in the flame. The detection of high concentrations of $\text{Si}(\text{OH})_4$ is in agreement with previous studies, where $\text{Si}(\text{OH})_4$ is the main product of TEOS decomposition and is the most stable product of TEOS decomposition in the temperature range of 800-2200 K based on thermodynamic equilibrium calculations [10]. Positively charged clusters are proposed to be formed through the protonation of silicates from collisions with hydronium ions and hydroxyl radicals in the flame



where X represents possible silicate species. The presence of TEOS monomers and dimers implies incomplete decomposition of precursor molecules, thus further decomposition is expected to take place downstream leading to potential surface growth mechanisms. In addition intermediate hydrocarbon species from TEOS decomposition were detected in lower concentrations in the form of ethoxy and methoxy silanes including $\text{Si}(\text{OCH}_2)(\text{OC}_2\text{H}_5)_3$, $\text{Si}(\text{OH})_2(\text{OC}_2\text{H}_5)_2$, and $\text{Si}(\text{OCH}_3)_2(\text{OC}_2\text{H}_5)_2$. These species have been previously established as important intermediates in the decomposition of TEOS through various pathways such as ethylene elimination and radical additions [18].

The representative mass spectra for negatively charged species from Figure 2b yielded a wider variety of silicate peaks throughout the mass spectra. Most of the negatively charged silicate ions were in the form of $\text{Si}_n\text{O}_x(\text{OH})_y$ with an attached nitrate ion or nitric acid cluster, where the size of a cluster, n , represents the number of Si atoms within the oxide complex. The attachment of nitrate ions and nitric acid clusters to most of the negatively charged clusters demonstrates the presence of chemical ionization in the flame. The formation of negatively charged species is hypothesized to form through charge exchange and proton transfer between nitrate ions and silicate species (X)



The high concentration of silicic acid clusters agrees well with previous theoretical studies which have hypothesized particle growth to begin with a $\text{Si}(\text{OH})_4$ seed particle with successive growth occurring through $\text{Si}(\text{OH})_4$ addition and dehydration reaction pathways [19].

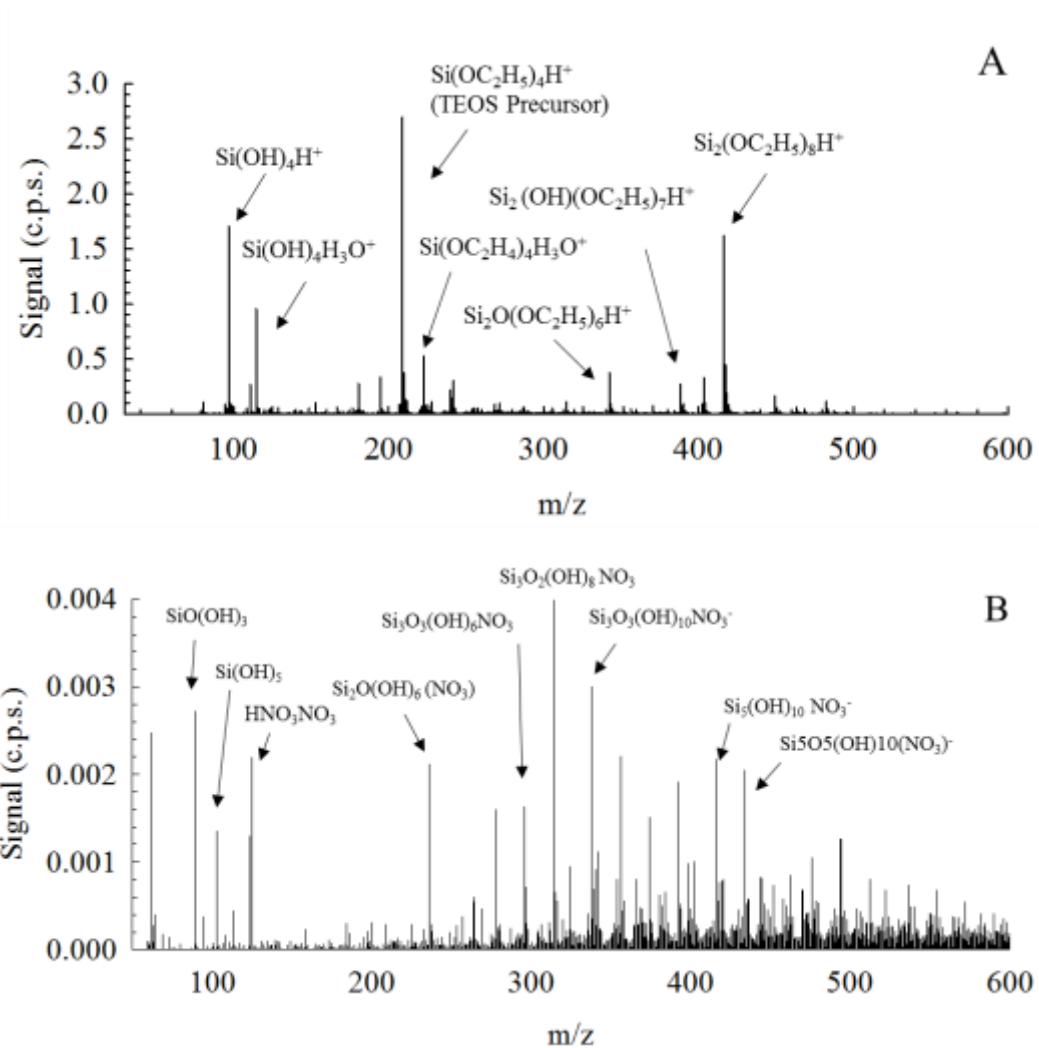
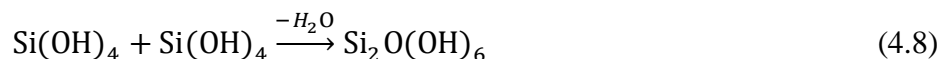
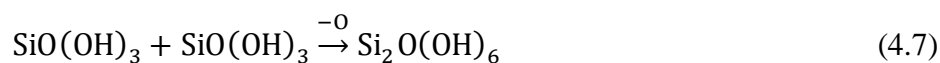
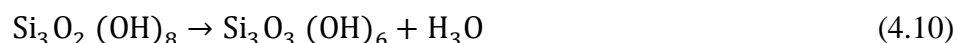
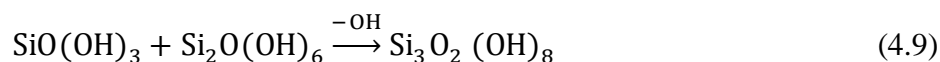


Figure 4.2: Natively charged clusters of measured for SiO_2 nanoparticle formation in a flame aerosol reactor for positively (A) and negatively (B) charged clusters.

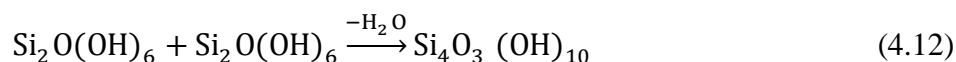
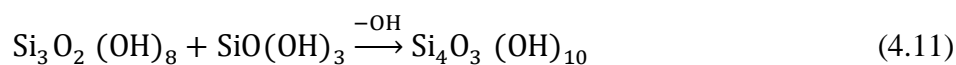
From Figure 4.2a and Table 4.3, various silicate monomer species were measured, thus demonstrating the possibility that additional hydrogen abstraction and oxidation reactions are taking place in the flame. Various monomers may participate in cluster growth, which begins with the formation of dimers through hydrogen abstraction and collisional growth of $\text{SiO}(\text{OH})_3$ and dehydration reactions from $\text{Si}(\text{OH})_4$ to form Si-O-Si ligands.



Furthermore, collisions between monomers and dimers will yield trimers of silicic acid species with hydroxyl groups attached with siloxane bond linking Si atoms:



At higher cluster masses, collisions can occur between a monomer and trimer or 2 dimers to form a cluster size of 4 Si atoms.



Clusters with up to 5 Si atoms could be identified, and proceeded to have similar collisional growth pathways through the formation of siloxane bonds. Beyond 450 Da, the molecular composition of peaks could not be assigned due to the high number of possible compounds and drift in calibration. Nonetheless, here we have presented the first measurements for the formation pathways of silicic acid clusters during combustion synthesis of SiO₂.

Table 4.3: Identified positive and negative ions measured by an API-TOF mass spectrometer

Molecular Composition	Mass	Molecular composition	Mass
Si(OH) ₂ •H ₃ O ⁺	81.001	SiO ₂ (OH) ₃ ⁻	110.975
Si(OH) ₄ H ⁺	96.996	Si(OH) ₅ ⁻	112.991
Si(OH) ₄ •H ₃ O ⁺	115.006	Si(OH) ₆ H ₂ ⁻	132.009
Si(OCH ₂)(OC ₂ H ₅) ₃ ⁺	193.290	Si(OH) ₄ •NO ₃ ⁻	157.976
Si(OH) ₂ (OC ₂ H ₅) ₂ ⁺	153.058	Si(OH) ₃ •NO ₃ ⁻	140.973
Si(OCH ₃) ₂ (OC ₂ H ₅) ₂ H ⁺	181.090	Si ₂ (OH) ₆ •H ₂ O ⁻	175.981
SiO ₅ C ₆ H ₁₅ ⁺	195.070	Si ₂ O(OH) ₆ •NO ₃ ⁻	235.953
Si(OC ₂ H ₅) ₄ H ⁺	209.121	Si ₂ (OH) ₆ O ₃ •NO ₃ ⁻	295.920
Si(OC ₂ H ₄) ₄ •H ₃ O ⁺	223.100	Si ₃ (OH) ₈ O ₂ •NO ₃ ⁻	313.930
Si ₂ O(OC ₂ H ₅) ₆ H ⁺	343.161	Si ₄ (OH) ₇ •NO ₃ HNO ₃ ⁻	355.910
Si ₂ (OH)(OC ₂ H ₅) ₇ H ⁺	389.203	Si ₄ (OH) ₈ O ₄ •NO ₃ ⁻	373.897
Si ₂ (OC ₂ H ₅) ₈ H ⁺	417.234	Si ₄ O ₃ (OH) ₁₀ •(NO ₃) ⁻	391.908
		Si ₄ O(OH) ₈ (NO ₃) ₃ ⁻	401.903
		Si ₅ (OH) ₈ (HNO ₃) ₂ ⁻	401.898
		Si ₅ (OH) ₁₀ (NO ₃) ₂ ⁻	433.893
		Si ₅ O ₁₁ (OH) ₈ ⁻	451.851
		SiO(OH) ₁₈ ⁻	461.914

4.4.2 Multicomponent new particle formation

The next step towards understanding composite nanoparticle formation was to add TTIP TEOS precursor to the flame aerosol reactor to study $\text{TiO}_2/\text{SiO}_2$ composite particle formation. The intent is to study whether SiO_2 clusters and TiO_2 clusters form independently from each other or initially interact to form mixed oxides. Figure 4.3 displays the negative mass spectra for the resulting clusters with the single component spectra and multicomponent spectra plotted together. It can be seen that many of the peaks for the multicomponent mass spectra overlap with that of the single component mass spectra, showing that products from pure SiO_2 particle formation are still present. Based on the distinct isotopic pattern of Ti atoms, we can easily distinguish between Ti

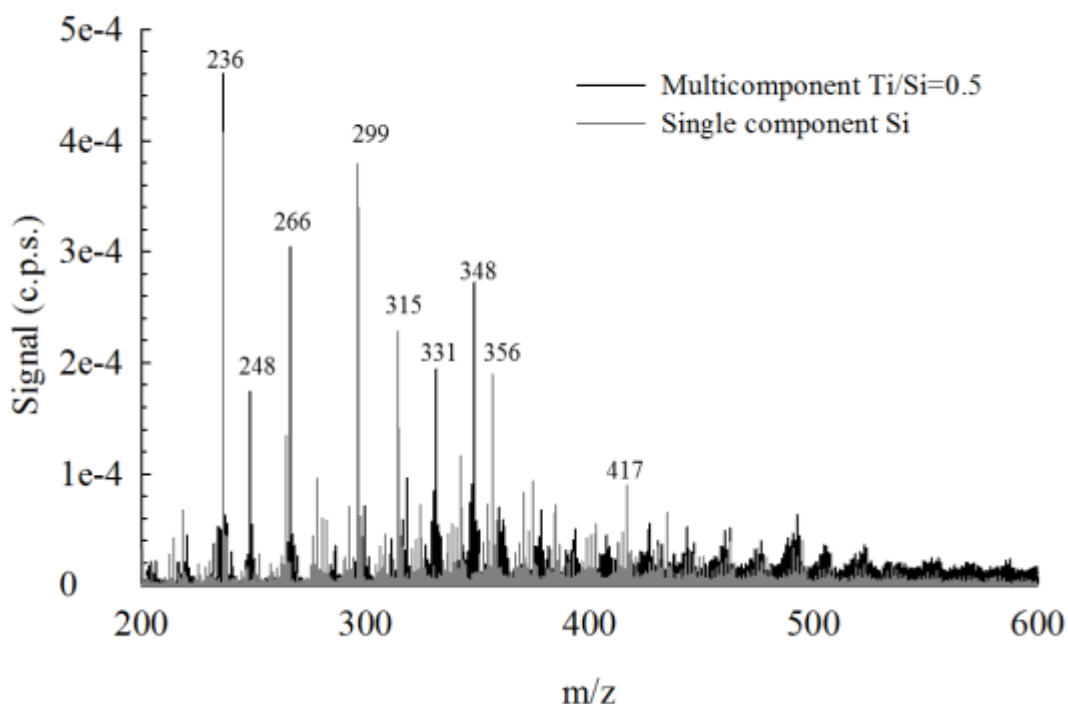


Figure 4.3: Direct comparison of resulting mass spectra of natively charged clusters for composite $\text{TiO}_2/\text{SiO}_2$ (black) and single component SiO_2 (gray) nanoparticle formation in a flame aerosol reactor.

containing species and pure Si species. The emergence of new peaks can also be seen beginning with an integer m/z of 236 Da. At this mass, two possible species exist: $\text{TiO}_4(\text{NO}_3)^-$ ($m/z=235.903$ Da), and $\text{Si}_2\text{O}(\text{OH})_6\text{NO}_3^-$ ($m/z=235.954$ Da). However, the distinct isotope pattern of a Ti containing cluster indicates the presence of titanium at this peak. Furthermore, larger Ti containing molecules with various Ti:O ratios could be identified such as

$\text{TiO}_2(\text{NO}_3)_3^-$ ($m/z = 265.901$ Da) and $\text{Ti}_3(\text{OH})_{11}^-$ ($m/z=330.874$). In the earlier stages of particle inception, each component will form smaller clusters independently. This supports previous work which has studied the vapor phase growth of iron oxide-silica nanocomposites in flames. These studies concluded that particle nucleation begins independently for each component [20, 21]. For larger cluster masses beyond 400 Da in Figure 4.3, previously prominent Si peaks are no longer present, providing evidence for the formation of multicomponent clusters due to the inevitable collisional growth between Si and Ti clusters. In multicomponent systems, the decomposition of precursors and formation of clusters most likely occurs independently, however beyond a critical cluster size, composite clusters will form beyond cluster sizes of 5. In larger size ranges however, we cannot identify the exact molecular composition of these species due to limitations in resolution and complexity of the spectra from overlapping isotope peaks. Future studies should aim to identify the size at which independent cluster formation transitions towards the formation of composite clusters.

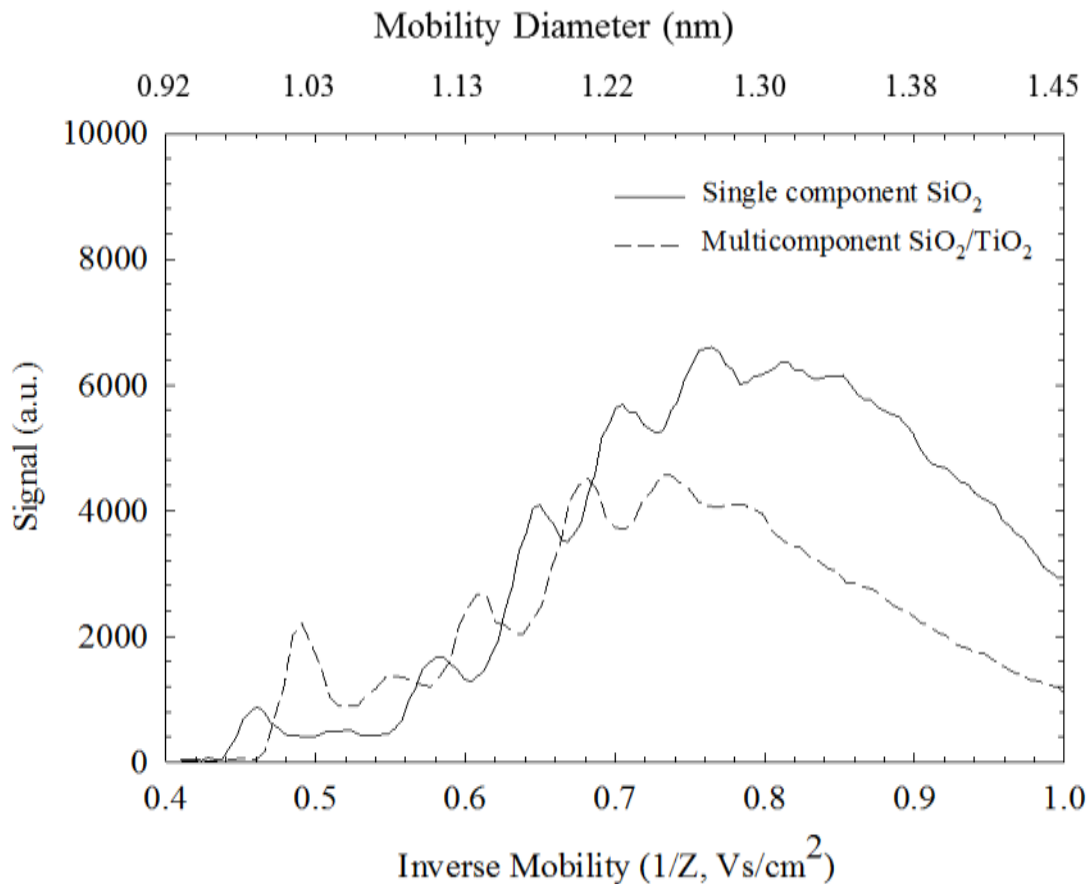


Figure 4.4: DMA mobility scans comparing mobility spectra for negatively charged pure SiO₂ (solid) and composite SiO₂/TiO₂ nanoparticle formation

4.4.3 Tandem Ion Mobility Spectrometry-Mass spectrometry

In order to gain more insight into the size resolved chemistry of new particle formation, tandem ion-mobility spectrometry – mass spectrometry was used to measure the mass of ions with respect to their electrical mobility. Although high resolution DMAs are very effective at classifying ions based on their size, electrical mobility alone is not sufficient for characterizing the initial stages of particle formation since they cannot provide information on molecular composition. Using a tandem DMA-MS can overcome these limitations while further providing insight into the size resolved chemistry for clusters below 2nm ($1/Z=1.897$ Vs/cm²). Figure 4.4a

displays a resulting mobility scan for ions as measured by a high resolution DMA for both single component and multicomponent cases. For the synthesis of pure SiO₂, several distinct ion peaks can be observed ranging from 0.46 Vs/cm² to 0.81 Vs/cm² (mobility diameter of 0.99-1.31 nm). In the case of multicomponent TiO₂/SiO₂ nanoparticle formation, the peaks shifted to the right indicating the formation of larger clusters and potential monomer scavenging.

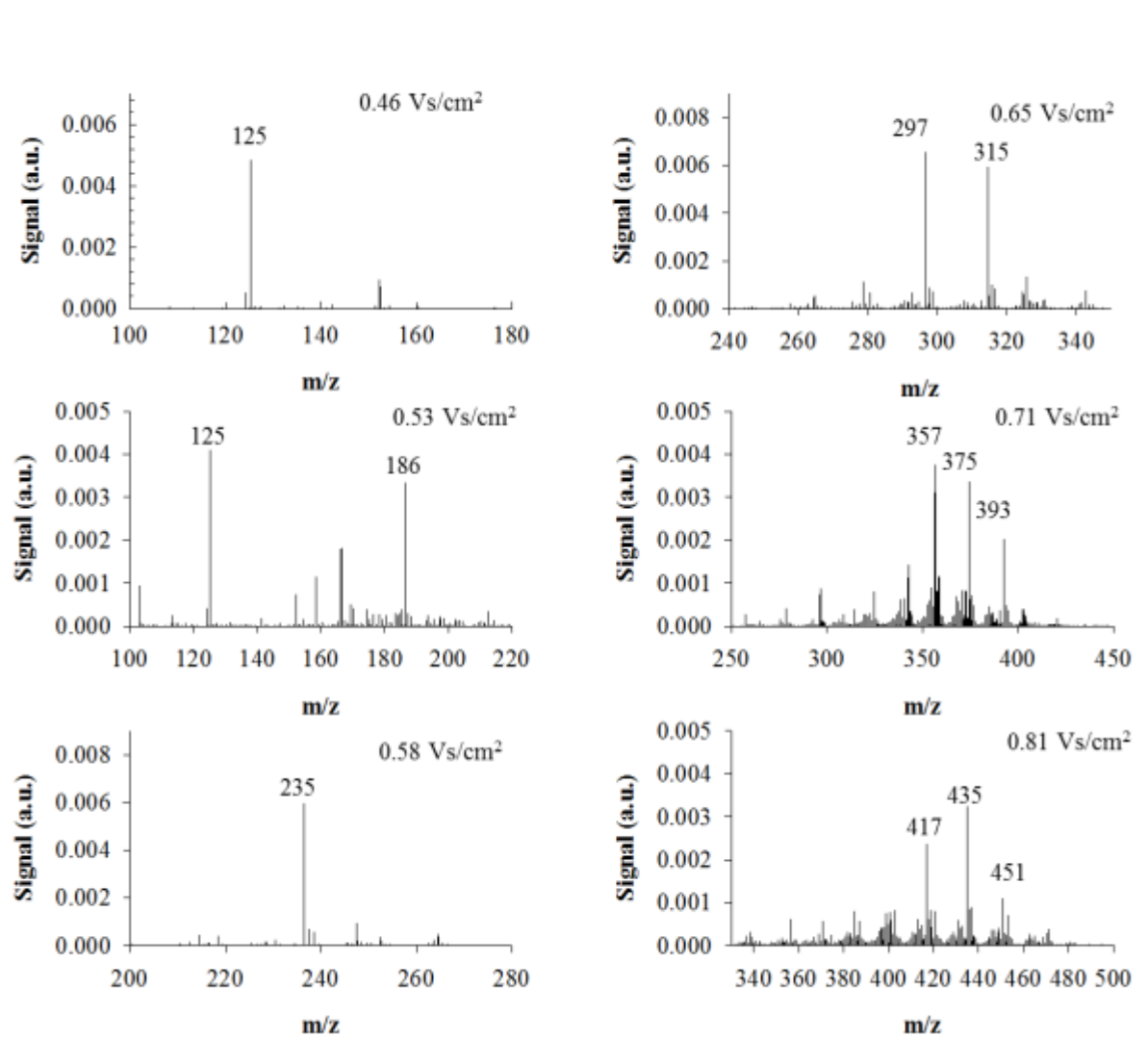


Figure 4.5: Negative mass spectra at a fixed electrical mobility for pure SiO₂ nanoparticle synthesis

The composition of the classified ions at each mobility were measured by maintaining a fixed voltage across the DMA at each of the ion peaks from the mobility spectra while mass spectra was collected and averaged over 2 minutes using the APi-TOF mass spectrometer. Figure 4.5 displays resulting mass spectra at fixed electrical mobilities where a series of ions classified by their electrical mobility is displayed. It can be seen that for each growing cluster size, multiple stable molecular species are present with various degrees of oxidation. For example, cluster sizes with $n=4$ Si atoms are measured at an electrical mobility of 0.71 Vs/cm^2 where 4 stable species including $\text{Si}_4(\text{OH})_7$, $\text{Si}_4(\text{OH})_8\text{O}_4$, $\text{Si}_4\text{O}_3(\text{OH})_{10}$, and $\text{Si}_4\text{O}(\text{OH})_8$ can be detected at this electrical mobility. From the presence of these species, we can see that adjacent hydroxyl sites may react to reduce the oxidation state of Si towards the steady state form of SiO_2 . Previous attempts to model cluster growth have assumed that for each discrete size, a uniform molecular composition exists. These results show that for the growth of oxide nanoparticles, significant reactions such as hydrogen abstraction, and dehydration reactions can occur even within a discrete cluster size. Most likely, due interactions with attached hydroxyl groups, hydrogen abstraction and dehydration are occurring within cluster sizes.

Similarly, for multicomponent systems, IMS-MS revealed the presence of multiple ion peaks at a fixed electrical mobility (Figure 4.6). The first peak, measured at 0.49 Vs/cm^2 was not displayed as it was a single cluster of HNO_3NO_3 . At the subsequent peaks, species of Ti monomers emerge at both 0.56 Vs/cm^2 and 0.59 Vs/cm^2 . Three main peaks at 236 Da, 248 Da, and 265 Da emerge at different intensities and could be identified as oxidized Ti monomers with nitrate radicals attached. Thus the shift in the mobility peak can be attributed to the higher mass of Ti clusters being measured by the DMA. For the first two peaks at 0.56 Vs/cm^2 and 0.59 Vs/cm^2 , due to the lower resolving power, the DMA was unable to completely resolve the monomer Ti peaks

at 236 Da and 265 Da. At higher inverse mobilities, previously detected Si peaks are no longer present in high concentrations, most likely due to scavenging.

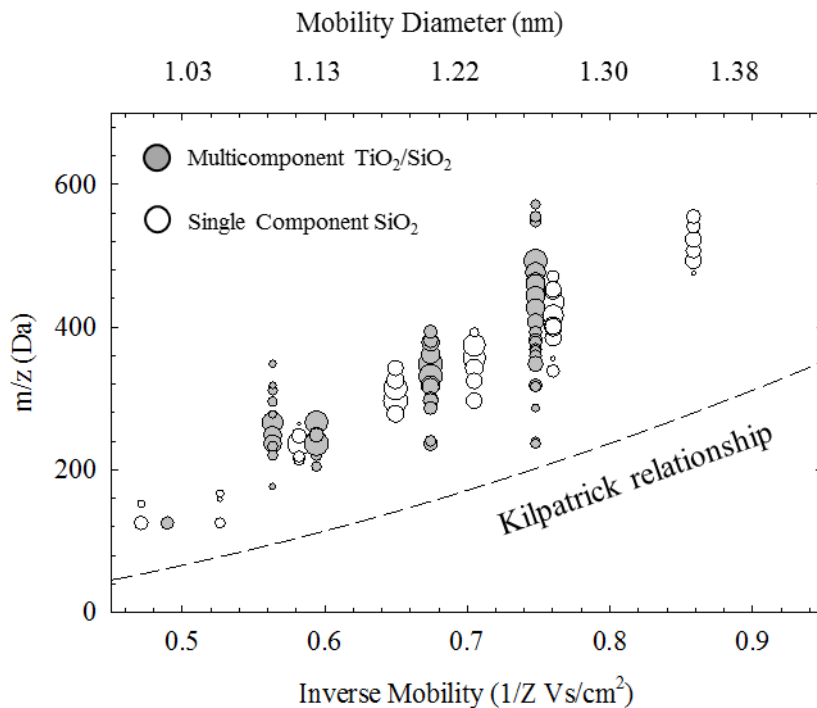


Figure 4.6: Comparison of the mass-mobility relationship for clusters of SiO₂ and composite

The relationship between mass and mobility in the free molecular regime is not well understood and can depend significantly on material properties. Figure 4.7 maps the inverse mobility with respect to the measured mass from tandem IMS-MS measurements. A dashed line in the plot indicates the Kilpatrick relationship [22], which is a commonly utilized relationship for estimating cluster mass with respect to electrical mobility in this size range. Clearly all of the measured clusters are well above the Kilpatrick relationship indicating that clusters of Si and Ti are much denser. Future studies relying on high resolution DMAs in this size range should have a clearer understanding of the measured ions chemical composition.

4.5 Conclusions

This work presents the first measurements of the new nanoparticle formation during the combustion synthesis of silica and composite silica/titania clusters. Using an atmospheric pressure inlet time-of-flight mass spectrometer, the cluster growth mechanisms, starting from monomers, for positively and negatively charged species in the flame are studied. Cluster growth mechanisms can be seen for silica as collisional growth between small clusters yield the presence of silicic acid units linked by siloxane bonds. The addition of TTIP precursor results in scavenging of silicate species to form larger clusters. By applying tandem ion mobility mass spectrometry, we examined the size resolved chemistry of cluster growth mechanisms. Results indicate significant chemistry occurring between clusters as silicate species of various Si:O ratio are present at the same Si cluster size, thus accurate modeling of collisional growth must account for interactions with OH- groups. In the case of multicomponent systems, Ti containing species appear to dominate the mass spectra as Si species can no longer be measured in high concentrations indicating the possible formation of mixed clusters.

4.7 References

- [1] L. Tang, J. Cheng, Nonporous silica nanoparticles for nanomedicine application, *Nano today*, 8 (2013) 290-312.
- [2] S.H. Ehrman, S.K. Friedlander, M.R. Zachariah, Phase segregation in binary SiO₂/TiO₂ and SiO₂/Fe₂O₃ nanoparticle aerosols formed in a premixed flame, *Journal of Materials Research*, 14 (1999) 4551-4561.
- [3] P. Worathanakul, J. Jiang, P. Biswas, P. Kongkachuichay, Quench-ring assisted flame synthesis of SiO₂-TiO₂ nanostructured composite, *Journal of nanoscience and nanotechnology*, 8 (2008) 6253-6259.
- [4] A. Teleki, S. Pratsinis, K. Wegner, R. Jossen, F. Krumeich, Flame-coating of titania particles with silica, *Journal of Materials Research*, 20 (2005) 1336-1347.
- [5] V. Tiwari, J. Jiang, V. Sethi, P. Biswas, One-step synthesis of noble metal-titanium dioxide nanocomposites in a flame aerosol reactor, *Applied Catalysis A: General*, 345 (2008) 241-246.
- [6] M. Sahu, K. Suttiponparnit, S. Suvachittanont, T. Charinpanitkul, P. Biswas, Characterization of doped TiO₂ nanoparticle dispersions, *Chemical Engineering Science*, 66 (2011) 3482-3490.
- [7] J. Haapanen, M. Aromaa, H. Teisala, M. Tuominen, M. Stepien, J. Saarinen, M. Heikkilä, M. Toivakka, J. Kuusipalo, J. Mäkelä, Binary TiO₂/SiO₂ nanoparticle coating for controlling the wetting properties of paperboard, *Materials Chemistry and Physics*, 149 (2015) 230-237.
- [8] E. Thimsen, S. Biswas, C.S. Lo, P. Biswas, Predicting the Band Structure of Mixed Transition Metal Oxides: Theory and Experiment, *The Journal of Physical Chemistry C*, 113 (2009) 2014-2021.
- [9] M. Sahu, B. Wu, L. Zhu, C. Jacobson, W.-N. Wang, K. Jones, Y. Goyal, Y.J. Tang, P. Biswas, Role of dopant concentration, crystal phase and particle size on microbial inactivation of Cu-doped TiO₂ nanoparticles, *Nanotechnology*, 22 (2011) 415704.
- [10] W. Phadungsukanan, S. Shekar, R. Shirley, M. Sander, R.H. West, M. Kraft, First-Principles Thermochemistry for Silicon Species in the Decomposition of Tetraethoxysilane, *The Journal of Physical Chemistry A*, 113 (2009) 9041-9049.
- [11] A. Shmakov, O. Korobeinichev, D. Knyazkov, A. Paletsky, R. Maksutov, I. Gerasimov, T. Bolshova, V. Kiselev, N. Gritsan, Combustion chemistry of Ti(OC₃H₇)₄ in premixed flat burner-stabilized H₂/O₂/Ar flame at 1atm, *Proceedings of the Combustion Institute*, 34 (2013) 1143-1149.
- [12] J.X. Fang, Y. Wang, M. Attoui, T.S. Chadha, J.R. Ray, W.N. Wang, Y.S. Jun, P. Biswas, Measurement of Sub-2 nm Clusters of Pristine and Composite Metal Oxides during Nanomaterial Synthesis in Flame Aerosol Reactors, *Anal. Chem.*, 86 (2014) 7523-7529.

- [13] K. Siefert, G. Griffin, Growth kinetics of CVD TiO₂: influence of carrier gas, *Journal of The Electrochemical Society*, 137 (1990) 1206-1208.
- [14] H.D. Jang, Generation of silica nanoparticles from tetraethylorthosilicate (TEOS) vapor in a diffusion flame, *Aerosol Science & Technology*, 30 (1999) 477-488.
- [15] H. Junninen, M. Ehn, T. Petäjä, L. Luosujärvi, T. Kotiaho, R. Kostianen, U. Rohner, M. Gonin, K. Fuhrer, M. Kulmala, A high-resolution mass spectrometer to measure atmospheric ion composition, *Atmospheric Measurement Techniques*, 3 (2010) 1039-1053.
- [16] T. Eichler, A Differential Mobility analyzer for ions and nanoparticles: Laminar flow at high Reynolds numbers, Senior Graduation Thesis presented to Fachhochschule Offenburg, Germany, (1997).
- [17] S. Ude, J.F. De la Mora, Molecular monodisperse mobility and mass standards from electrosprays of tetra-alkyl ammonium halides, *J. Aerosol. Sci.*, 36 (2005) 1224-1237.
- [18] D. Nurkowski, P. Buerger, J. Akroyd, M. Kraft, A detailed kinetic study of the thermal decomposition of tetraethoxysilane, *Proceedings of the Combustion Institute*, 35 (2015) 2291-2298.
- [19] S. Shekar, M. Sander, R.C. Riehl, A.J. Smith, A. Braumann, M. Kraft, Modelling the flame synthesis of silica nanoparticles from tetraethoxysilane, *Chemical Engineering Science*, 70 (2012) 54-66.
- [20] P. Biswas, C.Y. Wu, M.R. Zachariah, B. McMillin, Characterization of iron oxide-silica nanocomposites in flames: Part II. Comparison of discrete-sectional model predictions to experimental data, *Journal of Materials Research*, 12 (1997) 714-723.
- [21] B.K. McMillin, P. Biswas, M.R. Zachariah, In situ characterization of vapor phase growth of iron oxide-silica nanocomposites .1. 2-D planar laser-induced fluorescence and Mie imaging, *Journal of Materials Research*, 11 (1996) 1552-1561.
- [22] W. Kilpatrick, An experimental mass-mobility relation for ions in air at atmospheric pressure, in: *Proc. Annu. Conf. Mass. Spectrosc.* 19th, 1971, pp. 320-325.

5. Ions in Flames During Combustion Synthesis

5.1 Abstract

The ability to measure the particle size relies on charging capabilities and accurate knowledge of charge distributions. Below 2nm, charging efficiencies are extremely low while there has yet to be a consensus on mechanisms of charging below 2nm due to break downs in current charging theories in this size range. These are due to emerging complexities associated with changes in aerosol physics and material dependent properties. The first experiments in studying charge fraction below 10 nm is presented for the combustion synthesis of metal oxides for providing new insights into the charging mechanisms in flames. Furthermore, the role of ions in flames is examined through characterization of the electrical properties in flames for flame aerosol reactors.

5.1 Introduction

Combustion is a complex self-sustaining process which involves a large concentration of ions and radicals generated from a high temperature reacting flow. The presence of these ions in flames will affect how particles are charged during the initial stages of particle growth. Difficulties in understanding the role of ions during combustion result from the dynamic nature of combustion due to high temperatures, rapid reaction rates, and low charge fraction making charge fraction measurements difficult due to the short characteristic times of charging and ion recombination. Significant effort has been placed on studying ions in flames for various combustion systems [1], however the role of ions during the initial stages of particle formation during the combustion synthesis of metal oxides has yet to be studied in detail.

Previous studies regarding the electrical properties in flames began with efforts to understand the effects of sampling on flames for molecular beam mass spectrometry (MBMS), where flame ions are sampled through a metallic conical nozzle into a mass spectrometer [2]. MBMS is the most widely used technique for studying flame chemistry and structure due to its ability to resolve individual chemical species. Flame sampling through a direct nozzle can result in significant sample distortion in the flame due to aerodynamic disturbances [3], temperature gradients [4], concentration gradients [5], and potential gradients [6]. The presence of an electric field prompted many studies on this matter both for positively charged and negatively charged ions [7]. However, this has yet to be studied in the context of combustion synthesis of metal oxide nanoparticles.

Charging in flames can occur through several processes including diffusion charging, thermionization, chemical ionization, and photoionization [8]. Charging processes during

combustion are important both for understanding particle growth pathways and for the measurement of particle size distributions. For particle growth, the formation and recombination of ions may affect the growth rates and mechanisms of nanoparticles in flames [1]. Charging is particularly crucial for the accurate determination of particle size distributions through data inversion for electrical mobility based measurements. Currently, a size dependent charge fraction is assumed based on the Wiedensohler approximation [9] which was developed based on an equilibrium charge state of nanoparticles predicted through Fuch's charging theory [10]. Yet, many experimental observations of charging in flames have relied on the Boltzmann charge distribution, which is based on the kinetic theory of gases and free molecular charging [11, 12]. Below 10nm, charging efficiencies are extremely low and can be system dependent. Fuch's theory assumes that diffusion charging occurs through Brownian collisions of ions with a single mass and mobility. This assumption may break down in flames due to the complex environment and presence of various ion species. Thus it is critical to examine how a flame aerosol reactor's electrical properties may relate to the overall charging mechanisms during the initial stages of particle growth.

The goal of this section is to study the electrical characteristics of flames as it relates to the charging of nanoparticles during the initial stages of combustion synthesis. This will first be done by measuring the size distribution of naturally charged, neutral, and charged conditioned aerosols from a flame aerosol reactor. Furthermore ions in the flame aerosol reactor will be measured in response to an electric field through current-voltages measurements. Finally, a boosted condensation particle counter will be used to measure the charge fraction of sub 2nm clusters.

5.2 Experimental Methods

An experimental plan for the different types of measurements taken is presented in Table 5.1. Both a methane-oxygen and hydrogen oxygen premixed flat flame aerosol reactor (F-FAR) was used. Further details on the operation of this system using methane as a fuel has been described in chapters 2-5. The nitrogen, methane, and oxygen flow rates were 9.3, 0.89, 2.34, and 2.34 lpm respectively. TTIP and TEOS precursor flow rates were controlled to 0.72 mmol/hr and 0.53 mmol/hr respectively. In the case of hydrogen (test 3c), the nitrogen carrier gas flow rates were further increased 13 lpm while the hydrogen and oxygen flow rates were 2.47 and 1.0 lpm ensure proper matching of the hydrogen flame speed while precursors were fed at the same molar flow rates. All flow rates were controlled using mass flow controllers (MKS Instruments, Andover MA).

Table 5.1: Experimental plan for the study of charging and the role of ions during combustion synthesis

Purpose	Test	Charge conditioning	Fuel	Material
Compare natively charged and charge conditioned size distributions	1a	Kr-85 diffusion charger	CH ₄	TiO ₂
	1b	Inactive neutralizer replacement	CH ₄	TiO ₂
Compare the neutral fraction with the charged fraction of flame generated nanoparticles	2a	Charged particle remover operated at 1KV	CH ₄	TiO ₂
	2b	Charged particle remover operated at 3.4 KV	CH ₄	TiO ₂
	2c	Charged Particle Remover and Kr-85 neutralizer	CH ₄	TiO ₂
Measure IV curves to study the electrical characteristics during combustion synthesis for various materials and fuels	3a	In Situ Charged Particle remover and electrometer	CH ₄	-
	3b	In Situ Charged Particle remover and electrometer	CH ₄	TiO ₂ /SiO ₂
	3c	In Situ Charged Particle remover and electrometer	H ₂	TiO ₂ /SiO ₂

5.2.1 Size distribution measurements

Comparisons of natively charged and charge conditioned size distributions for flame generated nanoparticles were measured using two different test conditions. Standard size distributions were measured using a scanning mobility particle sizer (SMPS) with a TSI 3085 DMA and 3081 classifier. Since no charging efficiency is assumed, all data presented will be in the form of raw counts (#/cc), which is the concentration detected by the CPC. Natively charged size distributions were measured by replacing a Kr-85 neutralizer with an inactive neutralizer (no diffusion charging), this would only ensure that natively charged nanoparticles would be classified. The molar flow rate of TTIP was controlled to 2.88 mmol/hr while the nitrogen, oxygen, and methane flow were metered at 8.21 lpm, 2.85 lpm, and 0.99 lpm respectively. Size distributions were measured at a 1cm height above the burnerhead.

5.2.2 Neutral fraction particle size distributions

A charged particle remover (CPR) was added in line to the dilution sampling flow to remove natively charged particles. The neutral fraction of the particles were then charged downstream of the CPR using a Kr-85 neutralizer to enable the measurement of the neutral fraction of the overall particle size distribution. Differences between the charged and neutral fraction were studied to provide insight into the differences between charged and neutral particle size distributions generated in a flame aerosol reactor. Figure 5.1 displays a schematic diagram of the experimental setup.

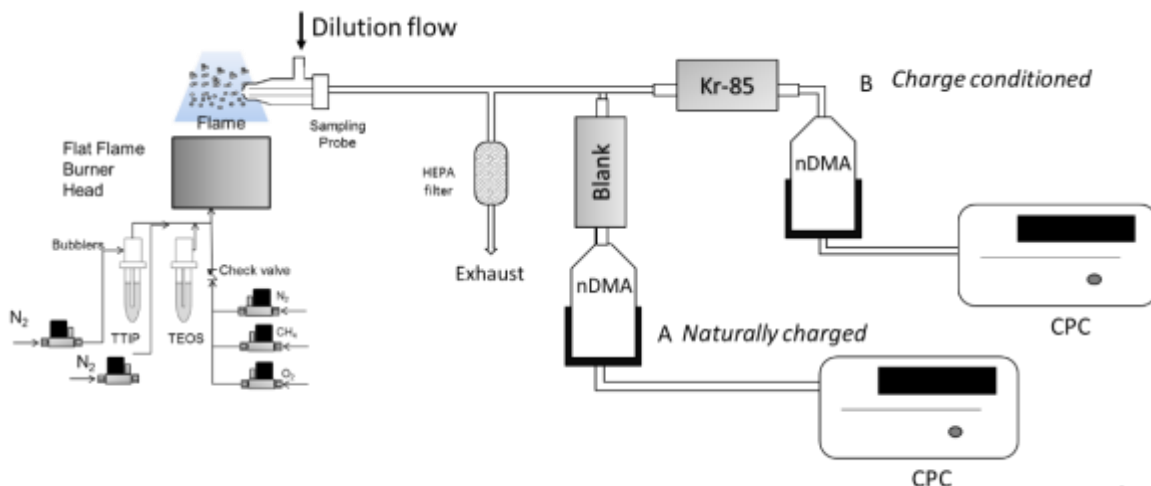


Figure 5.1: Experimental setup for measuring natively and charge conditioned particle size distributions

5.2.3 In situ charged particle removers and electrical properties of flames during combustion synthesis.

Using a radial aluminum plate located 1 inch from the burner head in a parallel configuration, a DC voltage was applied to induce a uniform electric field in the flame allowing for a current-voltage scan to characterize the electrical properties during combustion synthesis allowing for the measurement of IV curves. IV curves were measured with and without precursor addition while using hydrogen and methane fuels. The current and voltages were controlled and measured using a Keithley 2400 electrometer where the burner head acted as the charged electrode while the parallel plate with the sampling nozzle was grounded. The term ion collector plate will be used to represent the grounded parallel conductive metal plate and sampling nozzle assembly. The gap between the burner and ion collector plate was 2.54 cm above the flame and had a radius of 3.81 cm to provide sufficient coverage of the diameter of the flat flame, which has a cross

sectional surface area of 5.07cm^2 . The potential difference ($\Delta\phi$) can be determined as the difference between the burner head potential (V_B) and the ion collector plate potential (V_S) in the form of $\Delta\phi=(V_B- V_S)$. Voltage scans were performed in steps of 5 Volts with a time step of 0.5 seconds from -200 to 200 volts. The IV curves were measured both for methane and hydrogen flames with precursors for TiO_2 and SiO_2 .

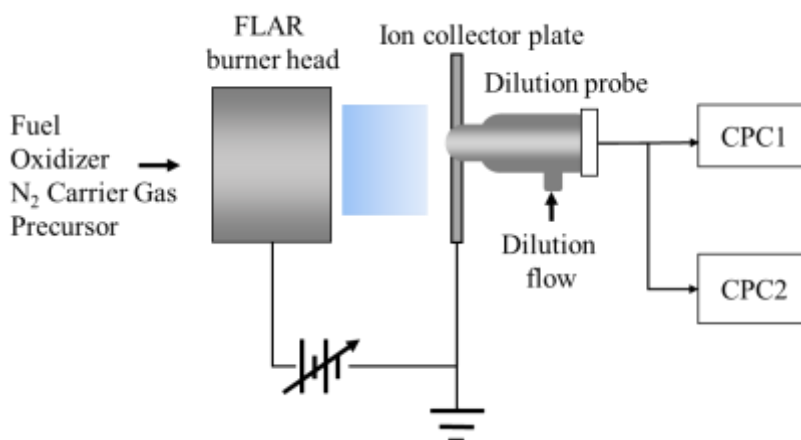


Figure 5.2: Measurement of IV curves in a flame aerosol reactor under a DC electric field along with measurement with a boosted CPC battery for measurement of sub 2nm cluster size distributions

5.2.1 Boosted CPC for measurement of sub 2nm size distributions

Condensation particle counters (CPC) are a robust and well established method for counting particles and measuring number concentrations. Current CPCs are typically designed to have a lower detection limit of about 2nm, however recent developments have enabled CPC detection limits below this range allowing for studies of particle formation below 2nm. One method is through the control of the CPC saturator and condenser temperature, which can increase the CPC

detection efficiency for lower size ranges. A commercial TSI 3025A Ultrafine CPC was used and modified for enhanced detection of sub 2nm charge fractions based on procedures from Kuang et al. [13].

5.3 Results and Discussion

5.3.1 Naturally charged versus charge conditioned size distributions

Results from measuring charge conditioned and naturally charged particle size distributions are displayed in Figure 5.3. These particle size distributions were measured by directly measuring size distributions from the dilution flow without any charging. This provides the size distributions from particles charged in the flame through high temperature diffusion charging, chemical ionization, and thermionization. Charge conditioned nanoparticle size distributions were measured by passing sampled aerosols through a Kr-85 neutralizer which is representative of an equilibrium charge state through diffusion charging. The size distribution for natively charged clusters exhibit a slightly higher geometric mean when compared to that of charge conditioned aerosols. This implies that there is a significant fraction of neutral particles below 10 nm which are naturally uncharged, and thus unclassified in the natively charged size distribution. Furthermore the native charge distribution may not be an equilibrium charge distribution which may further undergo recombination during the sampling procedure as dilute aerosols may have undergone continuous collisions with background gas molecules.

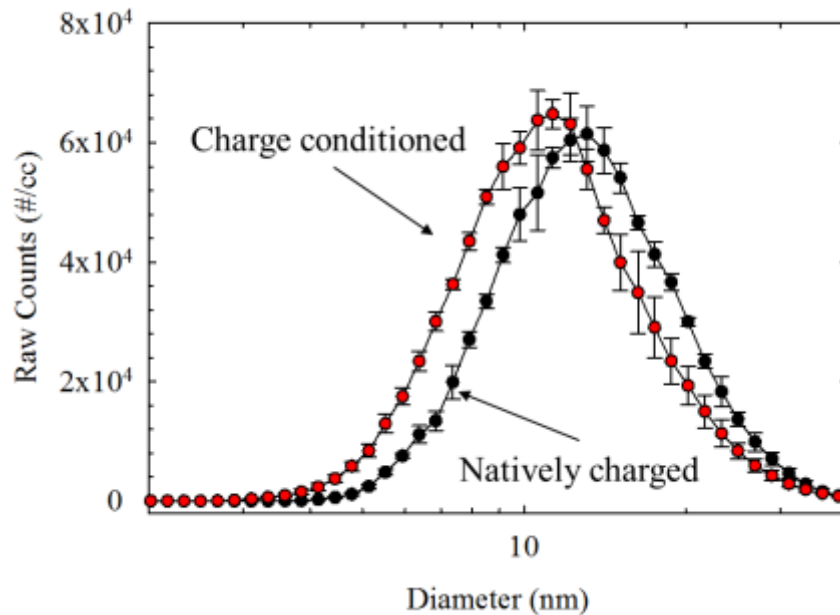


Figure 5.3: Comparison of natively charged and neutralized particle size distributions measured in a flame aerosol reactor as during the combustion synthesis of TiO_2

In order to measure the neutral fraction of aerosols generated during combustion synthesis, a charged particle remover was used (Figure 5.4). The naturally charged fraction was still measured by turning the CPR off and measuring the size distribution. With the CPR turned on, no aerosols could be measured confirming the removal efficiency of the CPR. Finally, by adding an additional charge conditioning step, after the CPR was turned on, the neutral fraction of aerosols was charge conditioned and the resulting size distributions were measured. The neutral fraction of aerosols showed a similar shift towards a lower size distribution, which confirms the hypothesis that the lower shift in size distribution in Figure 5.3 was due to a large fraction of neutral aerosols which were not charged during combustion.

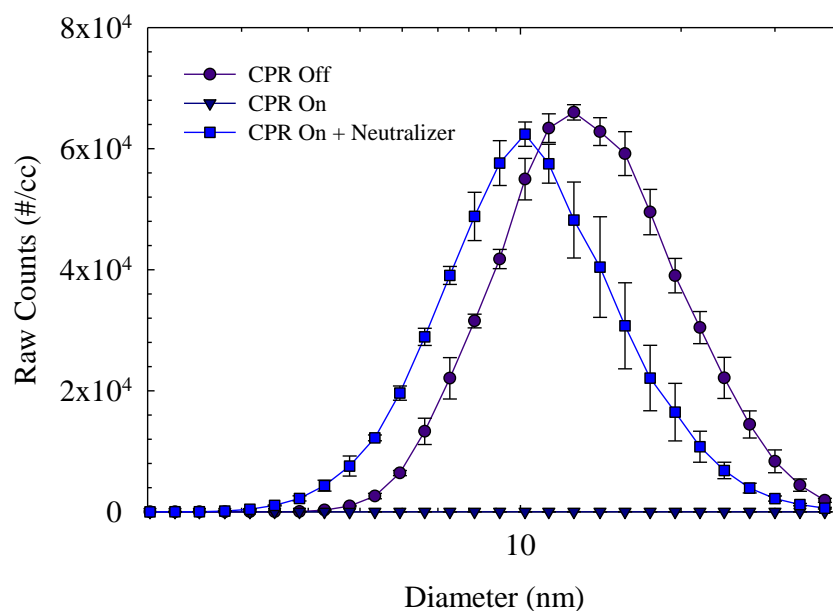


Figure 5.4: Particle Size distributions for the natively charged fraction (CPR-OFF), and neutral fraction (CPR-ON+Neutralizer) of particle. The effectiveness of the charged particle remover was confirmed as no particles were measured with the charged particle remover turned on without a neutralizer.

5.3.2 IV curves for measuring electrical properties in flames

The electrical properties of a premixed flat flame during the combustion synthesis of metal oxides was studied by applying a DC electric field across the flat flame while measuring the IV characteristics (Figure 5.5). Previous studies of the effect of electric fields on flames and mass spectrometric sampling have been performed for similar geometries but only with simplified systems of simple ions such as Cs^+ and Cl^- [6, 7, 14]. The flux of ions to the ion collection plate is a combination of convection, electrical migration due to the electric field, and diffusion. Diffusion

has been shown to be unimportant while mobility and convective forces dominate depending on the conditions. The potential gradient between the grounded sampling plate and burner head ($\Delta\phi$) allows for the ability to control the electric field across the flame. Since the flame has a radial geometry with a fixed surface area and the ion collection plate is parallel to the flame, the electric field for a given height (h) can be calculated as $(V_B - V_S)/h$ where V_B and V_S is the potential of the burner head and ion collection plate, respectively. When $\Delta\phi < 0$, then the burner is at a lower potential than the ion collection plate, thus the ion collection plate. In the opposite case where the burner head has a lower potential than the ion collector plate ($\Delta\phi > 0$), a positive current will be measured since the burner head will have a higher potential than the ion collection plate.

Beginning from figure 5.5a, the characteristic IV curves for a methane flame can be observed. Key differences in methane and hydrogen combustion result in different IV characteristics for blank flames (without precursor addition). From Figure 5.5, the blank methane flame has much current and ion concentration than hydrogen flame. Methane flames have higher ion concentrations than hydrogen flames due to the contribution of radical hydrocarbon species present during methane combustion, whereas hydrogen flames primarily have hydronium, hydroxide, oxygen radicals, and free electrons. With the addition of precursor for methane flames, there is negligible enhancement of current for the positive potential while the negative potential has a higher current and lower impedance across the bulk flame. Silica is known to be a radical scavenger due to significant hydroxide radical attachment, thus ion concentrations may be significantly lower in the case of TEOS precursor addition in the case of methane flames.

Hydrogen flames ($H_2 + O_2 + N_2$) exhibit different characteristics due to the lower ion concentrations (Figure 5.5 B). The current is already saturated within +/- 5 V with a saturation

current of $\sim 0.01 \mu\text{A}$. The addition of precursors results in new IV curve behavior with implications. Under both positive and negative potential, the saturation current is higher with the addition of TEOS precursor ($\sim 0.053 \mu\text{A}$). This higher saturation current is caused by the formation of charged clusters generated from the particle formation process for SiO_2 . This has implications both sampling flame clusters since at this point, charged clusters and ions will not be able to overcome the potential gradient caused by the high electric field to penetrate through the sampling nozzle, thus no charge clusters can be measured through the sampler. Furthermore, this demonstrates the ability to use the ion collector plate as an *in situ* charged particle remover.

Prior to reaching the saturation current, two distinct regions of linear current increase can be seen for positive currents. In order to understand this phenomena, we must understand the potential field across the burner head and the ion collection probe. At 0V potential difference, the current is measured at $0.0055 \mu\text{A}$. Free electrons have a tendency to attach to metal surfaces thus there exists a sheath of free electrons attached to the burner head and ion collector plate. This results in an increased potential across the bulk flame which attracts a small amount of positive ions to the ion collector plate. As the potential is increased. The current rapidly increases at a linear rate up until about 4 volts. Beyond this region a separate linear region with a lower slope can be seen (4-100V). These two regions exist due to the presence of negative ion and positive ion sheaths. Previous studies have established that resistance due to the bulk flame is negligible, however, the formation of ion sheaths results at the nozzle and burner interface results in higher potential gradients. Under negative potential, the second linear increase below 100 V does not exist indicating that in this region negative ion and free electron flux due to mobility dominates.

Figure 5.5b also displays the effect of adding TTIP precursor. The IV curve is remarkably different and has a shape more indicative of an ohmic potential gradient which can be caused either by a much higher concentration of ions being generated (even at similar concentrations) or significantly different ion mobility in the flame. Furthermore it should be noted that TiO_2 may not scavenge radicals as heavily as SiO_2 .

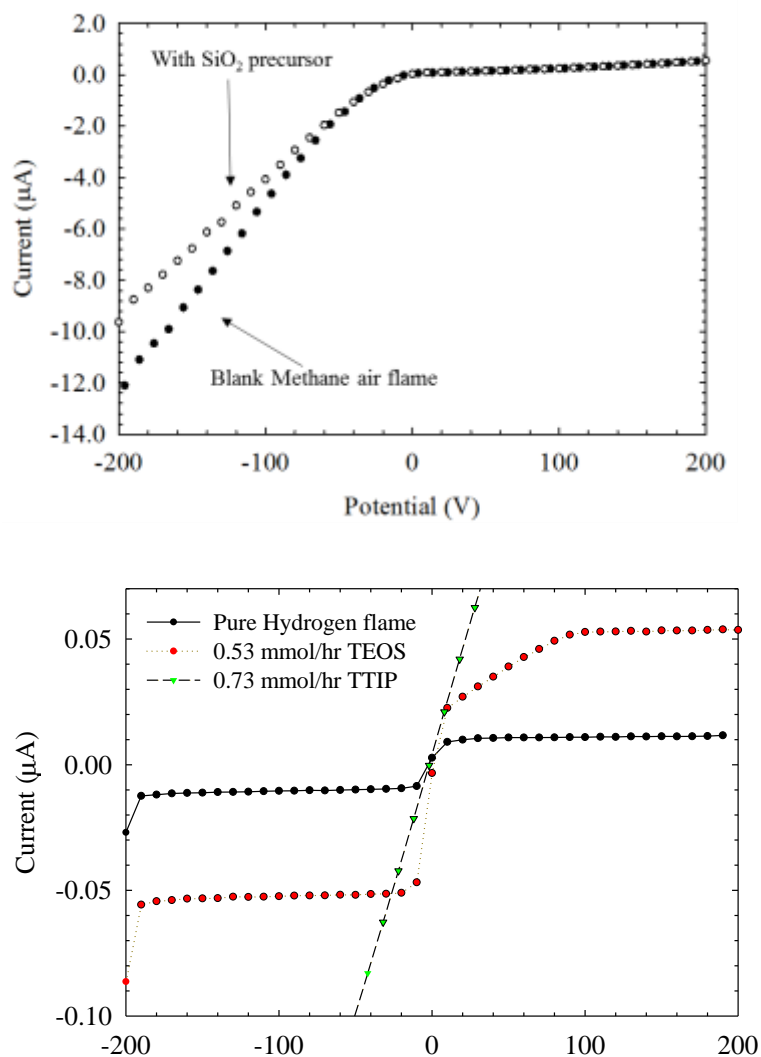


Figure 5.5: Current-voltage characteristics of a methane air flame (A) and a hydrogen flame (B) as measured by a parallel ion collector plate

5.3.3 Boosted CPC battery for charge fraction measurements of sub 2nm clusters.

The measurement of particle size distributions and clusters below 500 nm typically must rely on the ability to charge these particles, typically through an aerosol charge conditioner. However, current charging efficiency curves predict extremely low charging efficiencies below 2nm. A CPC allow for the detection of all nanoparticles, including neutrals, which make it an attractive method of measuring total particle concentration. With the use of a CPC battery, we measured the total number concentrations aerosols with a conventional 3025A CPC and a

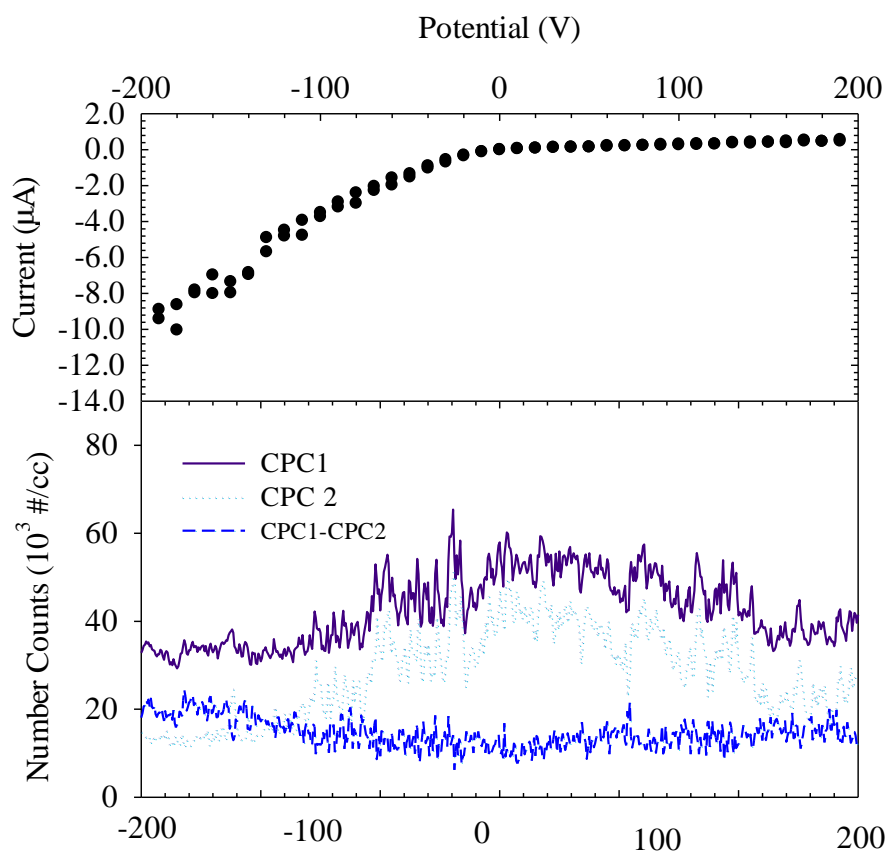


Figure 5.6: IV characteristics (a) and corresponding CPC battery measurements of clusters sampled in a flame aerosol reactor.

boosted 3025A CPC. This allows for a comparison of the number size distribution ranging from 1.48nm to 2 nm. This size range is previously neglected since it is too small for a nano-DMA to classify and it is too large for mass spectrometric sampling. Recently, several groups have been able to achieve size distribution measurement down to 1nm [15], but have yet to study flame environments in detail. Figure 5.6 shows results from CPC battery measurements downstream of the ion collector plate at various potentials.

5.4 Conclusions

Here we present measurements of charging characteristics and ions in a flame aerosol reactor to study the role of ions in flames using various techniques. By comparing the difference between naturally charged, charge conditioned aerosols, and neutral aerosols below 10nm, we see that there may be a significant fraction of neutral nanoparticles present in the size distribution. By applying electric fields in a flat flame, we can further measure current-voltage characteristics of premixed flat flames during the combustion synthesis of metal oxide nanoparticles. With the addition of precursor, a significantly higher ion concentration can be measured which may be due to charged ions during the particle growth process while different materials yield different current voltage characteristics in the flame. Finally using a boosted CPC battery we are able to measure particles below 2nm. Using an in situ CPR, very minor changes could be detected between 1.5 and 2nm indicating that the neutral fraction dominates below 2nm.

5.5 References

- [1] L.A. Sgro, A. D'Anna, P. Minutolo, Charge fraction distribution of nucleation mode particles: New insight on the particle formation mechanism, *Combustion and Flame*, 158 (2011) 1418-1425.
- [2] N. Hansen, T.A. Cool, P.R. Westmoreland, K. Kohse-Höinghaus, Recent contributions of flame-sampling molecular-beam mass spectrometry to a fundamental understanding of combustion chemistry, *Progress in Energy and Combustion Science*, 35 (2009) 168-191.
- [3] A.N. Hayhurst, D.B. Kittelson, N.R. Telford, Mass spectrometric sampling of ions from atmospheric pressure flames—II: Aerodynamic disturbance of a flame by the sampling system, *Combustion and Flame*, 28 (1977) 123-135.
- [4] A.N. Hayhurst, D.B. Kittelson, Mass spectrometric sampling of ions from atmospheric pressure flames—III: Boundary layer and other cooling of the sample, *Combustion and Flame*, 28 (1977) 137-143.
- [5] J.A. Miller, C.T. Bowman, Mechanism and modeling of nitrogen chemistry in combustion, *Progress in Energy and Combustion Science*, 15 (1989) 287-338.
- [6] S.D.T. Axford, J.M. Goodings, A.N. Hayhurst, Mass-Spectrometric Sampling of Ions from Flames at Atmospheric Pressure: The Effects of Applied Electric Fields and the Variation of Electric Potential in a Flame, *Combustion and Flame*, 114 (1998) 294-302.
- [7] A.N. Hayhurst, J.M. Goodings, S.G. Taylor, The effects of applying electric fields on the mass spectrometric sampling of positive and negative ions from a flame at atmospheric pressure, *Combustion and Flame*, 161 (2014) 3249-3262.
- [8] J. Jiang, M.H. Lee, P. Biswas, Model for nanoparticle charging by diffusion, direct photoionization, and thermionization mechanisms, *J. Electrostat.*, 65 (2007) 209-220.
- [9] A. Wiedensohler, An approximation of the bipolar charge distribution for particles in the submicron size range, *J. Aerosol. Sci.*, 19 (1988) 387-389.
- [10] N. Fuchs, On the stationary charge distribution on aerosol particles in a bipolar ionic atmosphere, *Geofisica Pura e Applicata*, 56 (1963) 185-193.
- [11] S. Kim, K. Woo, B. Liu, M. Zachariah, Method of measuring charge distribution of nanosized aerosols, *Journal of colloid and interface science*, 282 (2005) 46-57.
- [12] M.M. Maricq, The dynamics of electrically charged soot particles in a premixed ethylene flame, *Combustion and Flame*, 141 (2005) 406-416.
- [13] C. Kuang, M. Chen, P.H. McMurry, J. Wang, Modification of laminar flow ultrafine condensation particle counters for the enhanced detection of 1 nm condensation nuclei, *Aerosol Sci. Technol.*, 46 (2012) 309-315.

[14] J.M. Goodings, J. Guo, A.N. Hayhurst, S.G. Taylor, Current–voltage characteristics in a flame plasma: analysis for positive and negative ions, with applications, *International Journal of Mass Spectrometry*, 206 (2001) 137-151.

[15] J. Jiang, M. Chen, C. Kuang, M. Attoui, P.H. McMurry, Electrical mobility spectrometer using a diethylene glycol condensation particle counter for measurement of aerosol size distributions down to 1 nm, *Aerosol Sci. Technol.*, 45 (2011) 510-521.

6. Characterization of Nanostructured Niobium Doped TiO₂ Thin Films Synthesized in a Flame Aerosol Reactor

6.1 Abstract

Here we demonstrate the ability to synthesize transparent conducting nanostructured thin films of niobium-doped TiO₂ (NTO) using a flame aerosol reactor. Previous methods of synthesis have primarily relied on vacuum deposition techniques such as sputter coating, atomic layer deposition, and chemical vapor deposition. Combustion synthesis serves as a scalable method for depositing nanostructured films in an atmospheric environment with high growth rates while being able to control morphology. Ultrafine clusters of NTO are generated in an inverted premixed hydrogen flame directly facing a water cooled substrate holder. Nanoparticles deposited onto a glass substrate through thermophoresis then sinter into a nanostructured columnar morphology with a growth rate of approximately 40 nm/min. NTO nanostructured thin films with a thickness of approximately 200 nm were deposited at various niobium doping rates ranging from 0-28%. Based on conductivity and Hall measurements the lowest resistivity achieved was 0.04 Ohm cm with a carrier density of $5.06 \times 10^{16} \text{ cm}^{-3}$ and mobility of 8.17 cm²/Vs. Further characterization using XRD revealed polycrystalline anatase films while XPS revealed that Ti⁴⁺ and Nb⁵⁺ were primary oxidation states. A high transparency in the visible region was also measured ranging from 60-90%.

6.2 Introduction

Niobium doped titanium dioxide has attracted significant attention as an alternative transparent conducting oxide material due to its promising electrical and optical properties. Transparent conducting oxides are a class of metal oxides which combine electrical conductivity and optical transparency (primarily in the visible range) which allows for their application in solar energy conversion, light emitting diodes, and flat panel displays [1]. Currently tin-doped indium oxide (ITO) is the most widely adopted TCO on a commercial scale with resistivities on the order of $1-2 \times 10^{-4}$ Ohm cm. Fluorine doped tin oxide is also commonly used at an industrial scale for thin film solar cells with resistivities of 5×10^{-4} Ohm cm. These materials have large bandgap energies of $> 3\text{eV}$ allowing for their high transmittance in the visible and near-ultraviolet region. Over the past several decades, much effort has been focused on finding alternatives to TCOs due to increasing prices of indium and the exponential rise of flat panel displays and solar cells [2]. Niobium doped TiO_2 was first proposed by Furubayashi et al. [3] as an alternative to ITO and has gained significant attention over the past decade due to its stability, promising performance, and non-toxicity.

Pure anatase TiO_2 is a wide bandgap n-type semiconductor with bandgap of 3.2 eV. Doping TiO_2 with pentavalent niobium atoms results in increased conductivity performance since Nb^{5+} ions will occupy Ti^{4+} sites through interstitial doping, resulting in charge compensation by increasing the electron concentration in the conduction band. Upon increasing the niobium doping concentration above 10%, the conductivity will decrease due to the formation of competing point defects to maintain charge neutrality. Further doping beyond 20% approaches

the solubility limits of niobium, thus phase segregation will occur through the formation of niobium pentoxide.

Current methods of synthesizing NTO have relied primarily upon low pressure technique such as DC magnetron sputtering [4], atomic layer deposition [5], pulsed laser deposition [6], and chemical vapor deposition [7]. Deposition must often occur through epitaxial growth to achieve resistivities below 10^{-3} Ohm cm, thus much effort has focused on finding scalable routes of synthesis. More recently combinatorial atmospheric pressure chemical vapor deposition[7] and aerosol assisted vapor deposition[8] has been explored, although these techniques were performed at atmospheric pressure, the bulk resistivity values were still high while the overall growth rates were low.

A promising technique for scaling up the production of advanced nanomaterials is through combustion synthesis, which already has industrial application areas for the synthesis of commodity powders such as pure titania, carbon black, silica, and alumina powders. Combustion synthesis allows for the rapid synthesis of nanomaterials at high production rates while allowing for precise control of the thin film morphology [9]. Although extensive work as demonstrated promising applications for single component systems, recent focus has emphasized the ability to achieve precise control for multicomponent systems. For example, using this technique, Fe doped TiO_2 thin films with a tunable band structure could be synthesized for water splitting applications while Cu doped TiO_2 could also be used for microbial inactivation [10].

Here we present the synthesis of niobium doped TiO_2 (Nb-TiO_2) thin films through a scalable combustion synthesis technique. Combustion synthesis assisted aerosol vapor deposition in a flame aerosol reactor was used to deposit thin films of NTO with niobium percentages ranging

from 0-12%. In order to achieve different niobium doping ranges, the precursor feed rates of niobium were metered using a mass flow controller with nitrogen as a carrier gas. This synthesis technique provides a scalable technique with advantages of high growth rates, uniform thin film composition and morphology at atmospheric processing conditions. This work shows the first case of using a scalable multicomponent combustion synthesis technique for synthesizing nanostructured thin films for TCO applications.

6.3 Experimental Methods

6.3.1 Flame Aerosol Reactor

A premixed flame aerosol reactor was used for the combustion synthesis of Nb-TiO₂ (NTO) nanostructured thin films. A schematic diagram of the flame aerosol reactor is presented in Figure 6.1. A premixed hydrogen-oxygen flame using nitrogen as the carrier gas was stabilized over a 3/8" diameter perforated tube. The face of the burner head was patterned with evenly distributed holes to promote mixing and stability prior to the flame front. In order to minimize oxygen entrainment into the flame, a concentric 1 inch diameter stainless steel tube was used to shield the flame and provide a surrounding nitrogen sheath flow. An additional 1.5 inch diameter quartz glass tube was added used to shield the flame from surrounding gas entrainment. The distance between the flame and glass substrate was kept at 3 inches while the deposition time for the thin films were 5 minutes. The hydrogen and oxygen flow rates were metered at 4.31 and 1.69 lpm, respectively, using mass flow controllers (MKS). The total nitrogen flow was maintained at 6.3 lpm where a fraction of the flow was from the carrier gas flows through each of the precursor bubblers. Precursor bubbler flow rates ranged from 0-3 lpm. Feed rates for precursors were calculated using vapor pressure data provided by Siefering an

Griffin[11] and Saulys et al [12]. The precursor feed lines were wrapped with heated tape maintaining to prevent precursor wall condensation.

Thin films were deposited on a glass substrate (Eagle XG, Delta Technologies), where the substrate was mounted on a water cooled copper substrate. The surface of the copper substrate holder was polished prior to deposition experiments to ensure a smooth surface and proper thermal contact between the substrate and the cooled copper surface. The temperature of the film measured by a type K thin wire thermocouple was 350-450 K. Prior to starting thin film deposition, the system was allowed to warm up for 30 minutes with precursor flow and the flame lit to allow the system to stabilize and equilibrate. Deposition was initiated by inserting glass substrates into the flame along a guided slot on the substrate holder, and lowering the glass shield to prevent oxygen entrainment. After the deposition period, the oxygen and precursor flows were turned off to cut the flame. Hydrogen flow was maintained to ensure that the thin films would cool to room temperature under reducing conditions.

Table 6.1: Flame parameters for the flame synthesis of NTO thin films

Parameter	Value/description
Flame configuration	3/8" premixed
Total Nitrogen flow (lpm)	6.5
Oxygen Flow rate (lpm)	1.69
Hydrogen flow rate (lpm)	4.3
TTIP precursor delivery rate (mmol/hr)	0.49
Nb(OEt) ₅ precursor delivery (mmol/hr)	0-0.1
TTIP precursor temperature (Celsius)	30
Nb(OEt) ₅ precursor temperature (Celsius)	95
Nitrogen sheath flow rate (lpm)	2
Height above the burner head (cm)	7.62
Substrate temperature (Celsius)	350-400

6.3.2 Chemicals

Precursors used for Niobium and TiO₂ were Niobium(V) Ethoxide (>99%, Sigma-Aldrich) and Titanium(IV) isopropoxide (>97%, Sigma Aldrich). Precursor was delivered to a premixed flame using glass sealed bubblers (MDC) where the bubbler temperature was controlled through immersion in a temperature controlled hot mineral oil bath. Precursor feed lines were wrapped with heated tape to prevent condensation. Precursor feed rates were controlled by adjusting the bubbler temperatures and carrier gas flow rates.

6.3.3 Characterization

The morphology of the films were imaged using scanning electron microscopy and EDS (Nova NanoSEM 230 Field Emission SEM) operated at 15kV. The thickness was measured by cleaving the thin films down the center and mounting the glass substrates onto an SEM stage to allow for side imaging. The crystal structure of the thin films were measured using X-Ray diffraction with Cu K α radiation (wavelength=1.5406 Å) at 35 kV and 35mA (Rigaku D-MAX/A diffractometer, Japan). The conductivity of the thin films and Hall Effect measurements were performed by cutting the coated glass substrates into a small square at the center of the substrate while placing indium contacts at the 4 corners to create a Van der Pauw structure. Van der Pauw structures were then used for conductivity characterization (Janis ST-500 probe system) and Hall measurements. Transmittance and absorbance were measured in a UV-vis spectrometer (Shimadzu 3100) in the range of 250-1000 nm. The composition and of the NTO thin films along with the valence and chemical states of Nb and Ti were measured with X-ray photoelectron spectroscopy (XPS, PHI 5000 VersaProbe II).

6.3.4 Experimental plan

The material properties of niobium doped TiO_2 thin films were studied through varying the effect of niobium doping in a range of 0-15% during combustion synthesis. Each film was deposited for a period of approximately 5 minutes while the concentration of niobium was controlled by modulating the precursor flow rate delivery to the flame aerosol reactor. Each of the films were characterized for electrical conductivity, composition, and structure.

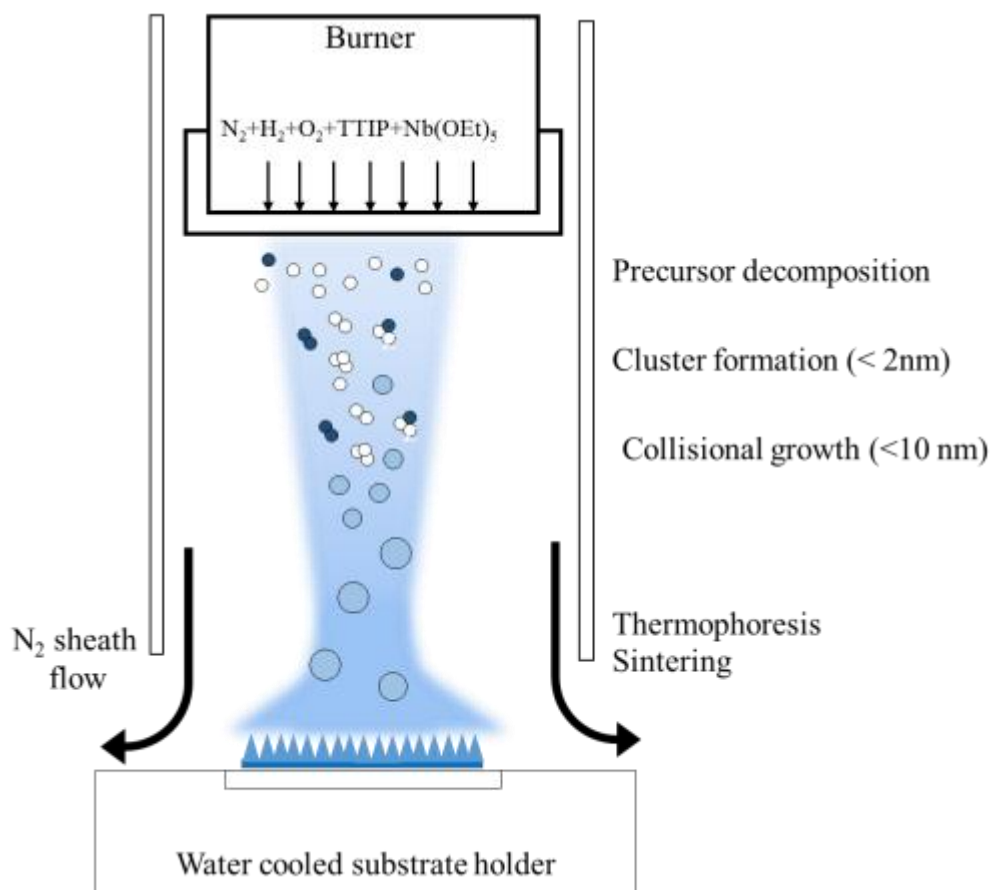


Figure 6.1: Schematic diagram of hydrogen fuel flame aerosol reactor used for the synthesis of niobium-doped TiO_2 nanostructured thin films.

6.4 Results and Discussion

Nanostructured thin films of niobium doped TiO_2 were synthesized using a flame aerosol reactor at various doping percentages by controlling the niobium precursor flow rate while maintaining a fixed titanium precursor flow rate. The relationship between precursor flow rate and film composition for doped nanostructured thin films is not clear. Several factors may affect the final thin films composition which include the decomposition kinetics, nucleation mechanisms, and deposition mechanisms. The mechanisms for the formation of NTO thin films can be described in the following steps: 1) precursor decomposition to form small clusters of NbTiO_2 , Nb_2O_5 , and TiO_2 , 2) collisional growth of stable clusters to form stable nanoparticles, 3) deposition for nanoparticles onto the substrate surface through thermophoresis through the boundary layer, and 4) sintering and crystallization into nanostructured thin films of $\text{Nb}_x\text{Ti}_{(1-x)}\text{O}_2$. It is assumed that particles are formed in the flame and deposit through thermophoresis. Below a particle size, the clusters behave like free molecules in the flame, thus thermophoresis is no longer dependent on particle size. Controlling various process parameters such as flame chemistry, precursor concentration, residence time, and substrate temperature will affect each of these steps and result in different thin film characteristics. A summary of the current flame conditions are provided in table 6.1.

6.4.1 Thin film composition and doping

The composition and morphology of NTO thin films were measured with SEM, EDAX, and XPS. A cross sectional SEM of a characteristic film is presented in Figure 6.2. It can be seen that the film exhibits a dense columnar nanostructured morphology, similar to that of pure TiO_2 nanostructured thin films in previous studies [9]. The thickness ranged from 180 nm to 220 nm yielding a growth rate of approximately 40 nm per minute. The column widths were

approximately 30-50 nm in diameter. This columnar morphology forms through several mechanisms including precursor decomposition, coagulation, condensation, and sintering. The addition of a dopants in the flame will further result in the formation of $Nb_xTi_{(1-x)}O_2$ nanoparticles in the flame, and due to the highly reducing environment, it is hypothesized that the formation of Nb_2O_5 is inhibited and that mixed oxides of $Nb_xTi_{1-x}O_2$ will form. The flame aerosol reactor enables the rapid decomposition of TTIP and $Nb(OEt)_5$ organometallic precursors which in turn results in the rapid formation of ultrafine nanoparticles. Based on previous measurements of particle size distributions in the flame aerosol reactor, the geometric mean diameter of particles arriving at the substrate is approximately 15-20 nm [9]. These ultrafine nanoparticles can then deposit onto the water cooled substrate (350 C-400 C) through thermophoretic deposition, upon which the particles will sinter into the nanostructured columns. For each of the samples, cross sectional area SEM measurements were used to determine the thickness of the thin film. Several measurements were taken across the film to ensure film uniformity.

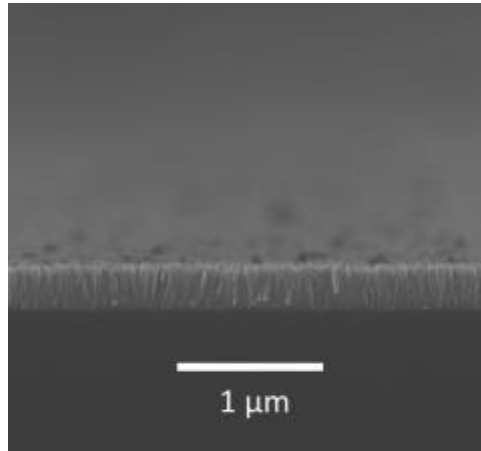


Figure 6.2: nanostructured morphology of NTO thin films synthesized through combustion synthesis.

The composition of thin films were measured using EDX and XPS. Resulting compositions of NTO thin films were characterized where x is the % of niobium doping in the thin film. The composition of the film measured by EDAX and XPS are listed in Table 6.2. Bubbler niobium % was calculated by $m_{Nb}/(m_{Nb} + m_{Ti})$, where m_{Nb} and m_{Ti} represent the molar flow rates of $Nb(OEt)_5$ and TTIP respectively, as calculated by the volumetric flow rate through the bubbler and the temperature dependent vapor pressure for each precursor [11, 12]. Comparisons of bubbler flow rate concentrations with EDAX indicates higher bulk composition of Nb in the thin films than what is predicted by bubbler mass flow rates. Thus there is a possible effect of different precursor decomposition rates, where $Nb(OEt)_5$ may have a higher decomposition rate than TTIP resulting in an increased fraction of niobium in the thin film than predicted by precursor delivery rates. These results were further confirmed with XPS by measuring the surface composition of the NTO thin films. XPS results show a higher composition of Nb when compared to bubbler concentrations, but lower when compared to

EDAX for samples 1-5 in the range of 0-10%. However at higher concentrations (sample 1), the XPS concentration is higher than both the EDAX concentration and the bubbler concentration indicating possible phase segregation and migration of niobium to the surface of the thin film, most likely due to the high temperature of synthesis. Similar discrepancies between surface and bulk composition measurements were also found with other synthesis techniques such as electron beam deposition [13].

Table 6.2: Thickness, composition, and performance of nanostructured thin films

Sample	Thickness (nm)	Niobium%			Performance		
		Bubbler	EDAX	XPS	E _g (eV)	T(%)	ρ (Ocm)
1	197	19.2	16.9	23	3.52	82.8	0.16
2	203	8.3	11.9	9.6	3.42	76.8	0.11
3	230	5.6	9.5	6.6	3.47	76.9	0.066
4	201	3.7	6.8	4.7	3.44	76.9	0.058
5	202	3.2	2.5	1.9	3.4	79.5	0.21
6	233	0	-	-	3.38	83.2	0.544

High-resolution XPS spectra for samples listed in Table 6.2 are shown in Figure 6.3. Binding energies for Ti 2p (Figure 6.6a) and the Nb 3d (Figure 6.6b) peaks were measured at around 458 eV and 207 eV respectively which matches well with literature values [7]. These values indicate primary oxidation states of Ti⁴⁺ and Nb⁵⁺. As the niobium doping rate is increased, the intensity of the Nb 3d peak (normalized with the intensity of the Ti 2p peak)

clearly also increases while the Nb 3d peak also shifts slightly to higher binding energies from 207.1eV to 207.2 eV from the lowest to the highest doping rates. The Ti 2p peak had a more significant shift from a binding energy of 458.4 eV at 0% Nb to 458.8 eV at 23% indicating increased charge compensation occurring with higher niobium percentages from the additions of electrons into the conduction band.

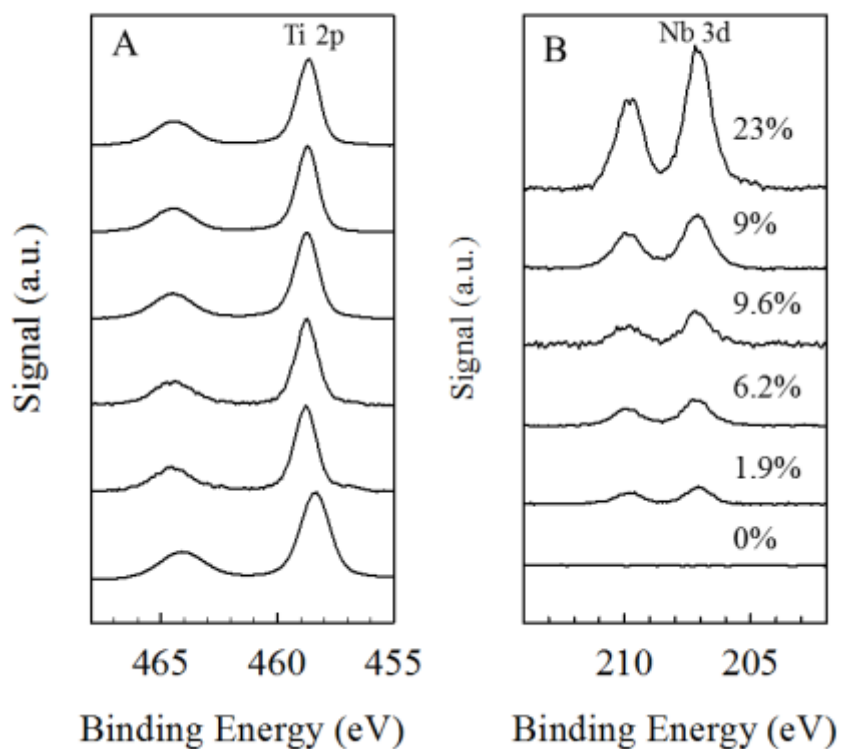


Figure 6.3: High resolution XPS spectra for (A) Ti 2p and (B) Nb 3d binding energies. The niobium percentages are labeled on the respective Nb peaks.

The crystal structure of the thin films as characterized by XRD is displayed in Figure 6.5. For all of the samples over the range of doping percentages, the film structure was anatase with 101 being the dominant peak. No rutile phase was detected with any of the samples further confirming that proper substrate temperatures were being achieved. As niobium concentration

increased, more growth in the (004) direction was also detected. With increasing doping %, 101 peak shifted to the left from 25.2 to 25.29 2θ demonstrating a shift in the crystal lattice due to niobium incorporation.

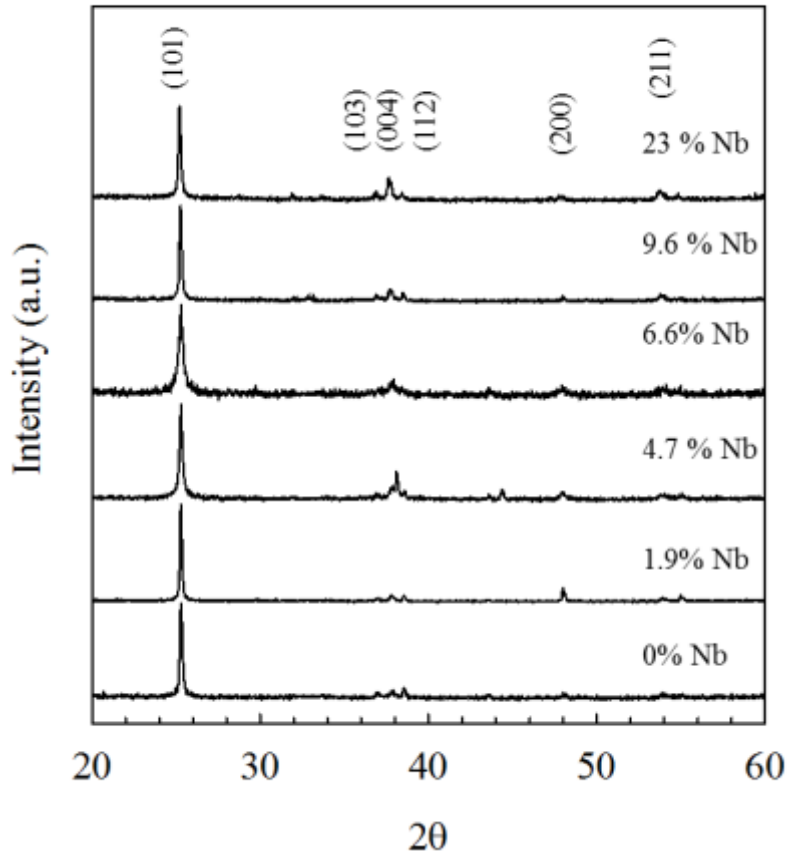


Figure 6.4: Normalized XRD spectra for NTO thin films synthesized through combustion synthesis.

6.4.2 Thin film Conductivity and performance

Figure 6.4 displays resulting conductivity measurements for each of the thin films while Table 6.2 displays the measured values for resistivity, transmittance, and bandgap. The effect of niobium doping concentration on conductivity, carrier concentration, and mobility was examined

for films of similar thickness and structure synthesized under the same conditions with the exception of varying niobium precursor feed rate. The niobium doping rate is reported based on XPS measured doping percentages. Pure TiO₂ thin films exhibited the highest resistivity values of 0.544 Ω cm. As niobium concentration increased to 4.7 %, the resistivity decreased by an order of magnitude to the lowest value of 0.0588 Ω cm along with a carrier concentration of 1.794 X 10¹⁹ cm⁻³ and a mobility of 8.17 cm²/Vs. As Nb doping further increased, the resistivity then reached a higher value of 0.158 Ω cm at 23% doping, however this was still much lower than that of pure TiO₂. The subsequent carrier density increased to 4.77 X 10¹⁸ cm⁻³ while the mobility increased to 119 cm²/Vs. Previous publications have also noted optimal niobium doping in ranges from 5-10% and experienced similar decreases in performance at higher doping rates due to the formation of competing defects and phase segregation.

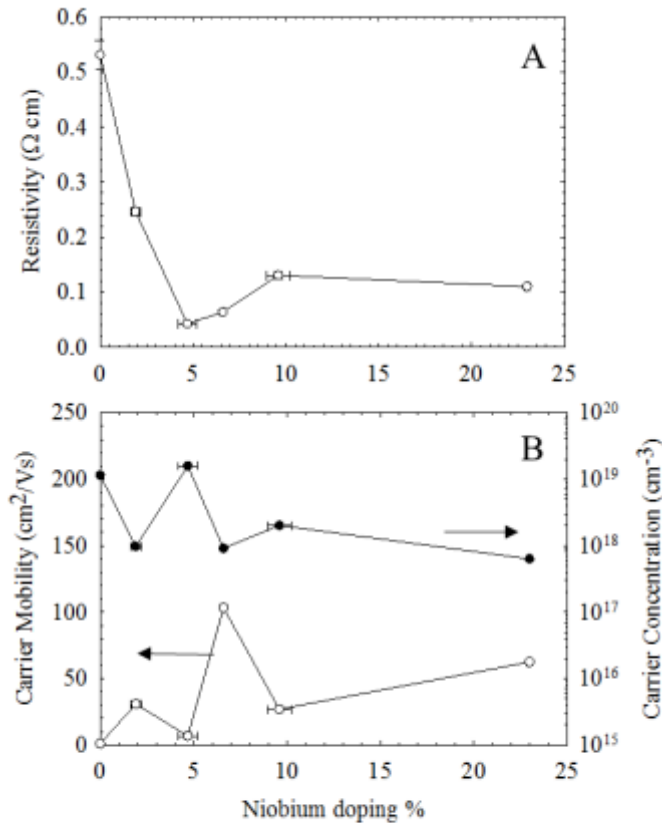


Figure 6.5: Conductivity characterization through measurements of (A) resistivity and (B) Hall mobility for NTO thin films synthesized in a flame aerosol reactor.

In order to investigate the optical properties of the NTO thin films, transmittance and absorbance measurements were taken in the range of 220 to 1000 nm. Figure 6.4a and Figure 6.4b displays the transmittance and absorbance spectra respectively. The transmittance in the visible range was 76.8-83%. Typically, 90% may be required for device use, thus these values are not as high as standard ITO, this has been attributed to the higher refractive index of NTO [4]. Figure 6.4b displays Tauc plots where the bandgap E_g could be extrapolated by scaling the absorbance with $(\alpha h\nu)^{1/2}$ and plotting it against the bandgap (E_g). As Niobium doping increases, a blue-shift to a higher bandgap from 3.38 eV to 3.52 eV can be observed resulting in a widening

of the bandgap. This is to be expected and has been observed frequently for NTO thin films and can be attributed to the Burstein-Moss effect [14].

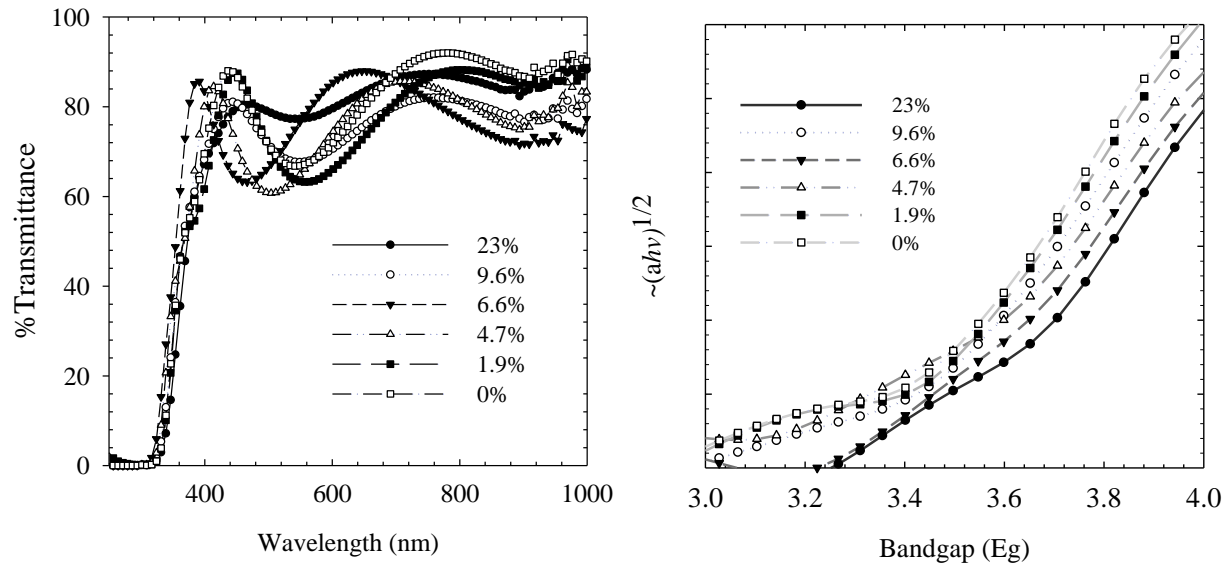


Figure 6.6: Optical characterization of thin films using (A) transmittance and (B) absorbance measurements for Tauc plots to measure the bandgap shift of thin films

6.5 Conclusion

Using a hydrogen fuel premixed flame aerosol reactor, transparent conducting nanostructured thin films of Nb-doped TiO_2 with an approximate thickness of 200 nm were deposited. The doping of niobium was controlled by adjusting the precursor flow rates allowing for Nb percentages from 0-23%. The lowest resistivity achieved was .0544 Ohm cm at a doping rate of 4.7%. Characterization using XRD confirmed anatase phase crystal structure and incorporation of niobium while XPS and EDAX confirmed the presence and composition of niobium. Optical

characterization revealed a transmittance of 60-90% in the visible regime. Future work should focus on understanding and controlling the dynamics of particle formation and deposition while further studying the mechanisms of deposition on the thin film. Optimizing this process is required to achieve more competitive performance.

6.6 References

- [1] K. Ellmer, Past achievements and future challenges in the development of optically transparent electrodes, *Nat Photon*, 6 (2012) 809-817.
- [2] A. Kumar, C. Zhou, The Race To Replace Tin-Doped Indium Oxide: Which Material Will Win?, *ACS Nano*, 4 (2010) 11-14.
- [3] Y. Furubayashi, T. Hitosugi, Y. Yamamoto, K. Inaba, G. Kinoda, Y. Hirose, T. Shimada, T. Hasegawa, A transparent metal: Nb-doped anatase TiO₂, *Applied Physics Letters*, 86 (2005) 2101.
- [4] Y. Sato, Y. Sanno, C. Tasaki, N. Oka, T. Kamiyama, Y. Shigesato, Electrical and optical properties of Nb-doped TiO₂ films deposited by dc magnetron sputtering using slightly reduced Nb-doped TiO₂-x ceramic targets, *J. Vac. Sci. Technol. A*, 28 (2010).
- [5] J.-P. Niemelä, Y. Hirose, T. Hasegawa, M. Karppinen, Transition in electron scattering mechanism in atomic layer deposited Nb:TiO₂ thin films, *Applied Physics Letters*, 106 (2015) 042101.
- [6] T. Hitosugi, A. Ueda, Y. Furubayashi, Y. Hirose, S. Konuma, T. Shimada, T. Hasegawa, Fabrication of TiO₂-based transparent conducting oxide films on glass by pulsed laser deposition, *Japanese journal of applied physics*, 46 (2007) L86.
- [7] A. Kafizas, C.W. Dunnill, I.P. Parkin, Combinatorial atmospheric pressure chemical vapour deposition (cAPCVD) of niobium doped anatase; effect of niobium on the conductivity and photocatalytic activity, *Journal of Materials Chemistry*, 20 (2010) 8336-8349.
- [8] D.S. Bhachu, S. Sathasivam, G. Sankar, D.O. Scanlon, G. Cibin, C.J. Carmalt, I.P. Parkin, G.W. Watson, S.M. Bawaked, A.Y. Obaid, S. Al-Thabaiti, S.N. Basahel, Solution Processing Route to Multifunctional Titania Thin Films: Highly Conductive and Photocatalytically Active Nb:TiO₂, *Advanced Functional Materials*, 24 (2014) 5075-5085.
- [9] E. Thimsen, P. Biswas, Nanostructured photoactive films synthesized by a flame aerosol reactor, *AIChE journal*, 53 (2007) 1727-1735.
- [10] M. Sahu, B. Wu, L. Zhu, C. Jacobson, W.-N. Wang, K. Jones, Y. Goyal, Y.J. Tang, P. Biswas, Role of dopant concentration, crystal phase and particle size on microbial inactivation of Cu-doped TiO₂ nanoparticles, *Nanotechnology*, 22 (2011) 415704.

- [11] K. Siefert, G. Griffin, Kinetics of Low-Pressure Chemical Vapor Deposition of TiO₂ from Titanium Tetraisopropoxide, *Journal of The Electrochemical Society*, 137 (1990) 814-818.
- [12] D. Saulys, V. Joshkin, M. Khoudiakov, T.F. Kuech, A.B. Ellis, S.R. Oktyabrsky, L. McCaughan, An examination of the surface decomposition chemistry of lithium niobate precursors under high vacuum conditions, *Journal of Crystal Growth*, 217 (2000) 287-301.
- [13] R.T. Tucker, N.A. Beckers, M.D. Fleischauer, M.J. Brett, Electron beam deposited Nb-doped TiO₂ toward nanostructured transparent conductive thin films, *Thin Solid Films*, 525 (2012) 28-34.
- [14] D. Kurita, S. Ohta, H. Ohta, K. Koumoto, Carrier generation and transport properties of heavily Nb-doped anatase TiO₂ epitaxial films at high temperatures, *Journal of Applied Physics*, 100 (2006) 096105-096101.

7. Conclusion

7.1 Summary

The initial stages of multicomponent particle growth during the combustion synthesis of nanomaterials were studied in this dissertation. Up until this point, gas to particle conversion mechanisms in combustion environments have remained largely a mystery due to limitations in instrumentation and challenges in measurement techniques. This dissertation presents the first set of studies focused on elucidating these mechanisms of cluster growth below 2nm for single and multicomponent systems in flame aerosol reactors.

Using a high resolution differential mobility analyzer, sub-2nm cluster size distributions during the combustion synthesis of single component TiO_2 and multicomponent $\text{TiO}_2/\text{SiO}_2$ were measured in a premixed flat flame aerosol reactor (F-FLAR). For the first time discrete clusters could be measured with high resolution in flame environments. Using the inverse mobility of these discrete clusters, the approximate mass of these clusters could be determined using existing mass-mobility relations. These clusters were hypothesized to be monomers, dimers, trimers and tetramers of TiO_2 while the addition of dopants revealed a shift in the cluster mobility providing evidence of mixed oxide formation at the initial stages. However electrical mobility based measurements alone were not sufficient to reveal the exact nature of these clusters.

To provide further insight into high resolution DMA measurements, the chemistry of gas to particle formation was further studied by using an atmospheric pressure inlet time-of-flight mass spectrometer to measure flame clusters during the combustion synthesis of TiO_2 . Resulting mass spectra revealed the presence of positively and negatively charged ions from the conversion of titanium (IV) isopropoxide (TTIP) towards TiO_2 . In the case of negatively mass spectra, by-products of chemical ionization were detected in the form of $\text{Ti}_n\text{O}_x\text{N}_y$, where nitrates played an

important role in the oxidation of TTIP to TiO_2 . Positively charged clusters yielded complex mass spectra ranging up to 1000 Da, thus mass defect plots were used to aid in interpretation. Based on Ti isotope patterns and mass defect plots, positive ions peaks were identified as intermediates of TTIP decomposition and oxidation. Thus prior to complete conversion to TiO_2 , partially oxidized TTIP intermediates would interact to form larger clusters of organometallic Ti.

Multicomponent clusters were further measured using both an API-TOF mass spectrometer and tandem ion mobility spectrometry-mass spectrometry to measure size resolved chemistry. During the conversion of TEOS to SiO_2 particles, $\text{Si}(\text{OH})_4$ and other intermediates of silica formation were measured, while identified ion peaks matched well with previous modeling studies on TEOS decomposition. It was also revealed that previous assumptions of a single monomer species being responsible for collisional growth are an oversimplification, and that for a single cluster size of Si_n , where n is the number of Si atoms in the cluster, multiple intermediate species can exist. In reality cluster growth is much more complex and needs to take into account the role of intermediate dimers, trimers tetramers, and so on. Extension of this towards multicomponent cluster formation demonstrated additional mixed oxide formation at the initial stages while experimental mass mobility plots further revealed that previous mass-mobility relations are under predicted the mass of metal oxide clusters at a given mobility.

One of the main challenges of studying the initial stages of cluster formation is the difficulty in charging clusters in this size range, and up to this point, only natively charged clusters and ions could be measured. By comparing naturally charged, charge conditioned, and neutral particle size distributions, it could be seen that charging below 10 nm is highly inefficient and that a large number of neutral particles are present in the flame. Current voltage

characteristics of the premixed F-FLAR during combustion synthesis showed that the ion concentration will change with the addition of precursor thus the charge fraction in flames may be higher than what was originally predicted by conventional charging theories.

Finally, insight into previous studies were applied towards making thin films of nanostructured niobium TiO₂ to demonstrate the feasibility of utilizing a flame aerosol reactor towards making transparent conducting oxides. An enhancement of conductivity could be measured by doping TiO₂ thin films using a premixed flame aerosol reactor to grow films. Doping was confirmed through further characterization of crystal structure, composition, and optical properties.

7.2 Future steps

Key findings from work performed in this thesis have set the foundation for developing a full mechanistic understanding of gas to particle conversion during combustion synthesis.

Further work in this area should focus on addressing the following gaps

- 1) *Mass-Mobility relationships below 2nm*: We do not have a complete understanding of the relationship between mobility and size in below 2nm for clusters of different composition. Although empirically measured relationships have been established, we still cannot accurately infer cluster mass or structure from electrical mobility measurements without specific knowledge on the cluster composition. Further work should focus on understanding how cluster properties for metal oxides such as effective density, and morphology can affect transport properties.

- 2) *Kinetics of cluster growth*: Predicting collisional growth rates relies on accurate collisional growth constants. To this date, very little work has been done to examine how cluster growth occurs at the initial stages. Now that we have identified pathways of formation at the initial stages, there is a need to examine accurate collisional growth kinetics for discrete clusters for both single component and multicomponent systems.
- 3) *Flame chemistry and flame structure*: Chemical ionization was shown to play a role in particle formation at the initial stages, thus flame chemistry may play an important role in resulting nanomaterial properties. The effect of flame chemistry and flame structure and its role on precursor decomposition, charging, and particle growth should be studied.
- 4) *Charging mechanisms below 2nm*: Current charging theories have not properly captured accurate charge distributions below 10nm. Difficulties stem from low charging efficiencies making a study of the neutral fraction extremely difficult. New techniques for studying charging and neutral particle growth should be developed.
- 5) *Sampling and measurement techniques*: More comprehensive measurements of flame cluster growth using tandem ion-mobility spectrometry-mass spectrometry should be implemented to minimize sampling effects while allowing for charging in the post sampling region. This will enable measurements of neutral clusters formed in the flame aerosol reactor.
- 6) *Optimization of niobium doped TiO₂ thin films*: the process of synthesizing NTO through combustion synthesis routes has yet to be optimized. Optimization will involve a more thorough understanding of the dynamics of particle formation and deposition which can occur either through boundary layer diffusion or thermophoresis. Predicting the final morphology will allow a more detailed study of the effect of the nanostructures on the

performance of the thin films. The ability to scale up this process will require better control of doping rates, particle formation kinetics, and deposition rates.

Appendix I:

Experimental Setup

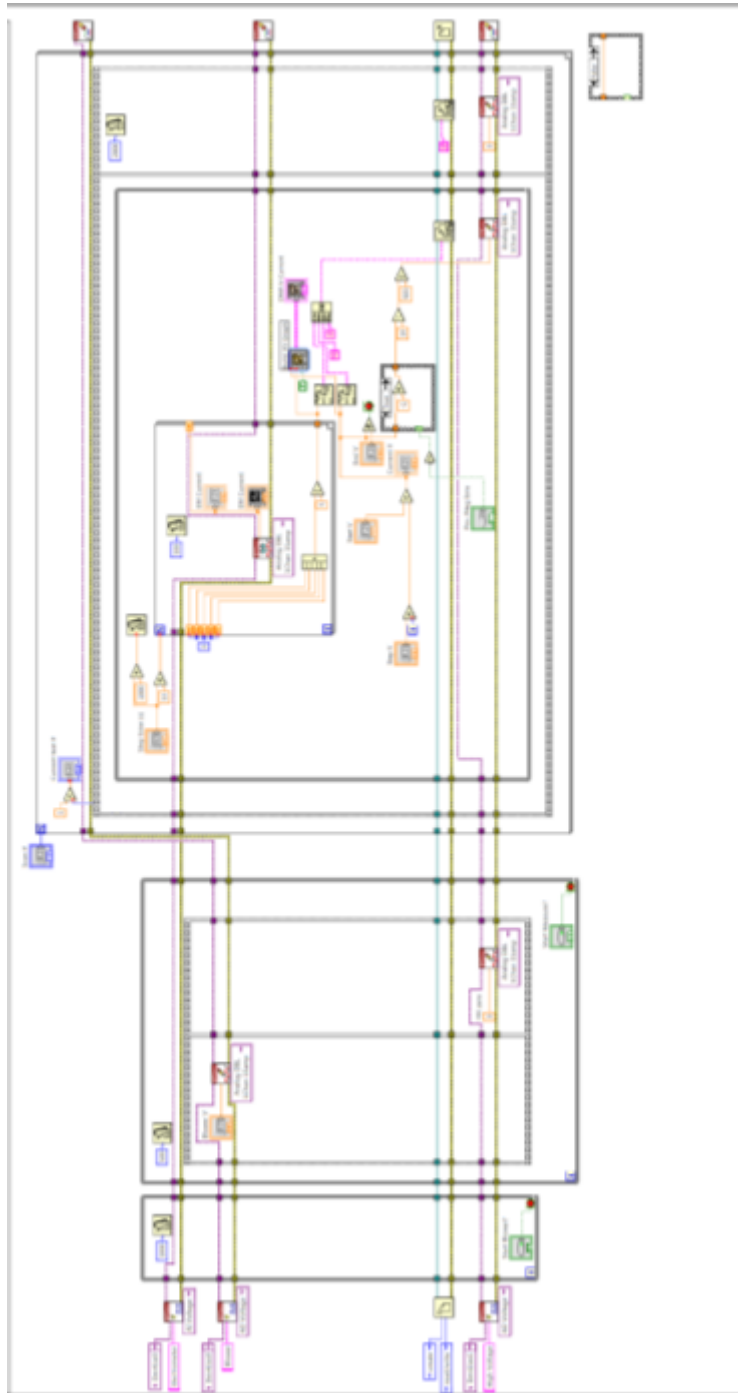


Figure I.1: Labview program for the control of the Half Mini DMA for measurement of sub 2m cluster size distributions

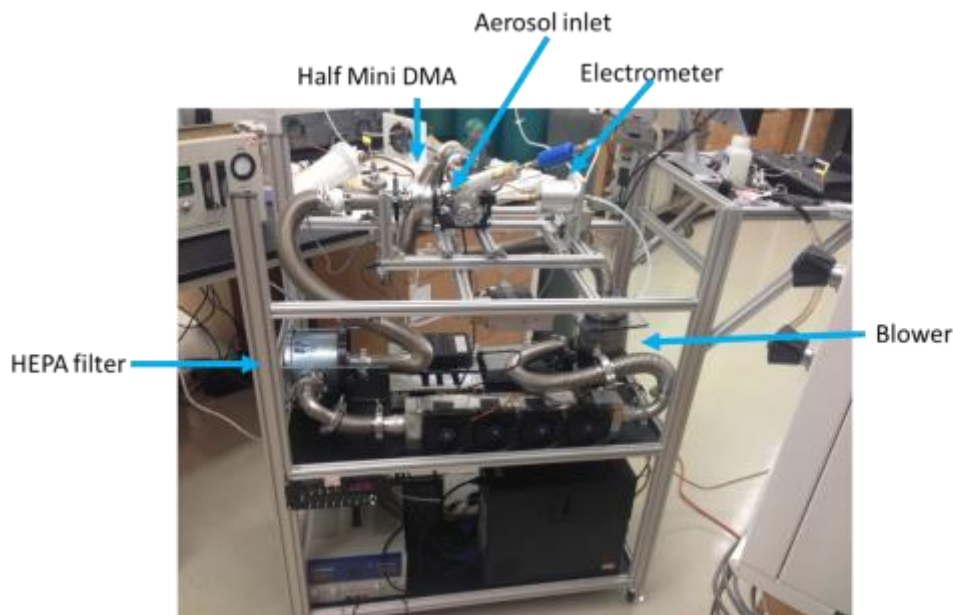
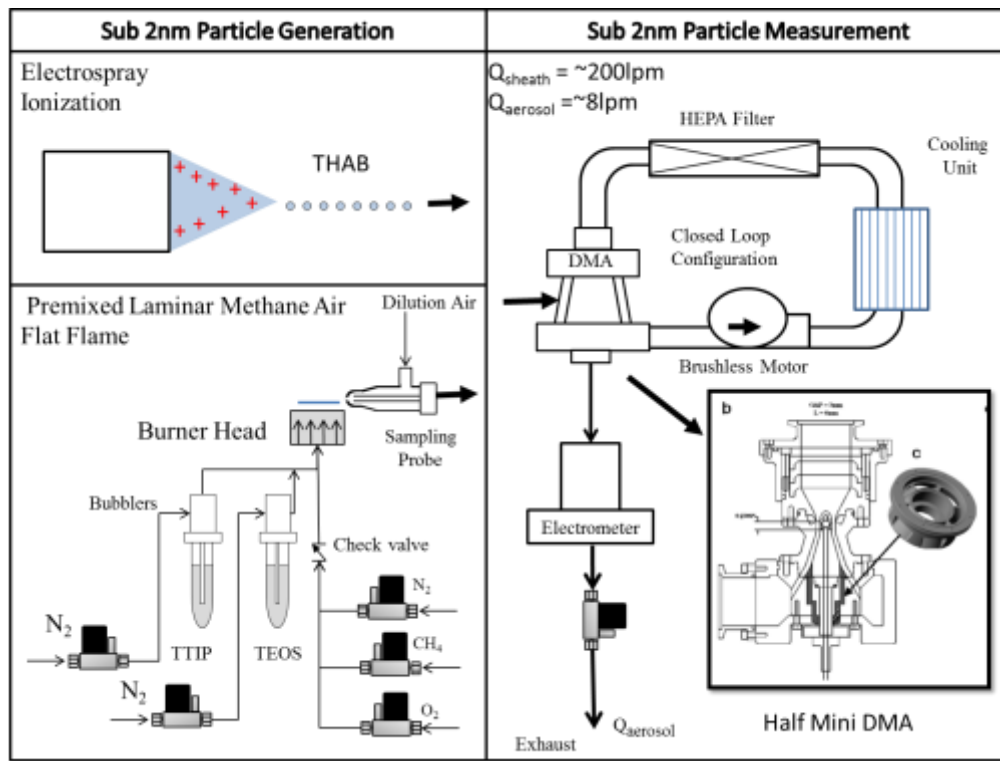
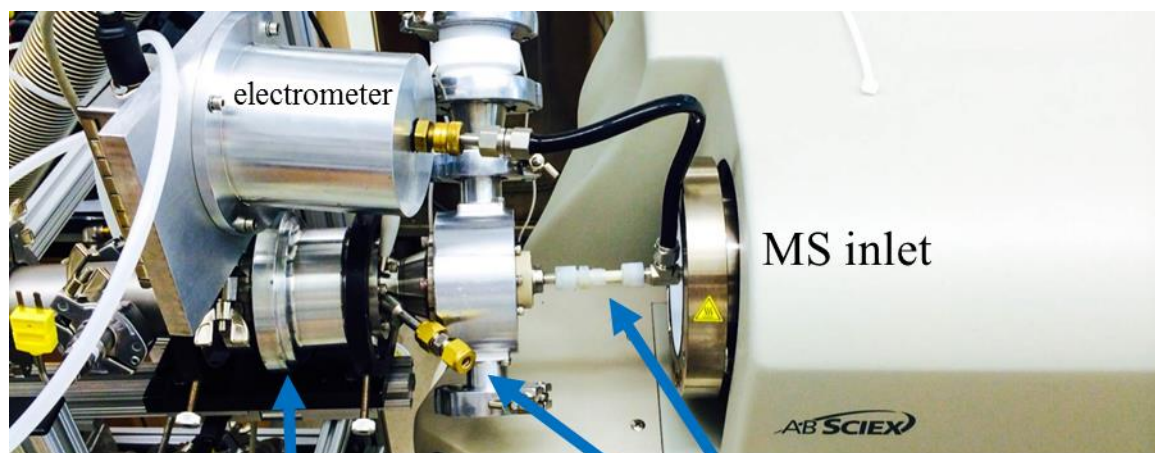


Figure I.2: Schematic diagram of flat flame aerosol reactor along with calibration and method of measuring sub 2nm cluster size distributions in a flame aerosol reactor (top). Photograph of half-mini DMA experimental setup (bottom).



Half Mini DMA Aerosol inlet (polydispersed) Aerosol outlet (monodispersed)

Figure I.3: Experimental Setup for coupling tandem ion mobility mass spectrometry using an API 2000 quadrupole mass spectrometer for measuring the size resolved chemistry of cluster formation.

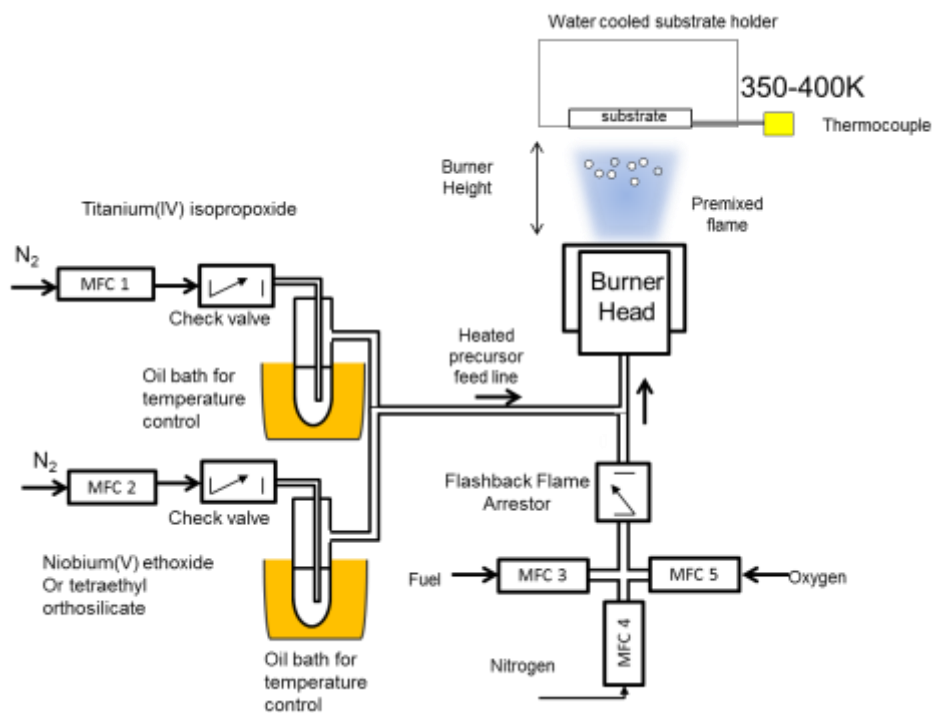


Figure I.4: Experimental set up of flame aerosol reactor used for synthesis of multicomponent niobium-doped TiO_2 thin films.

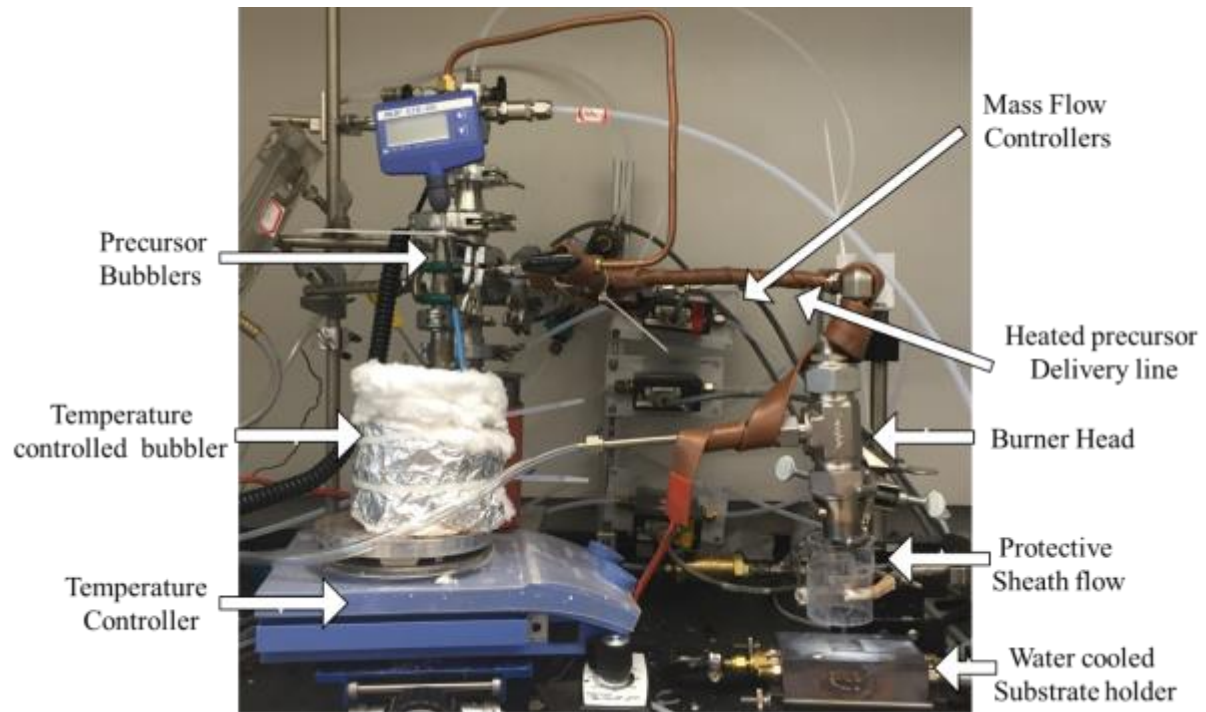


Figure I.5: Picture of premixed hydrogen flame aerosol reactor used for the combustion synthesis of niobium-doped TiO_2 thin films.

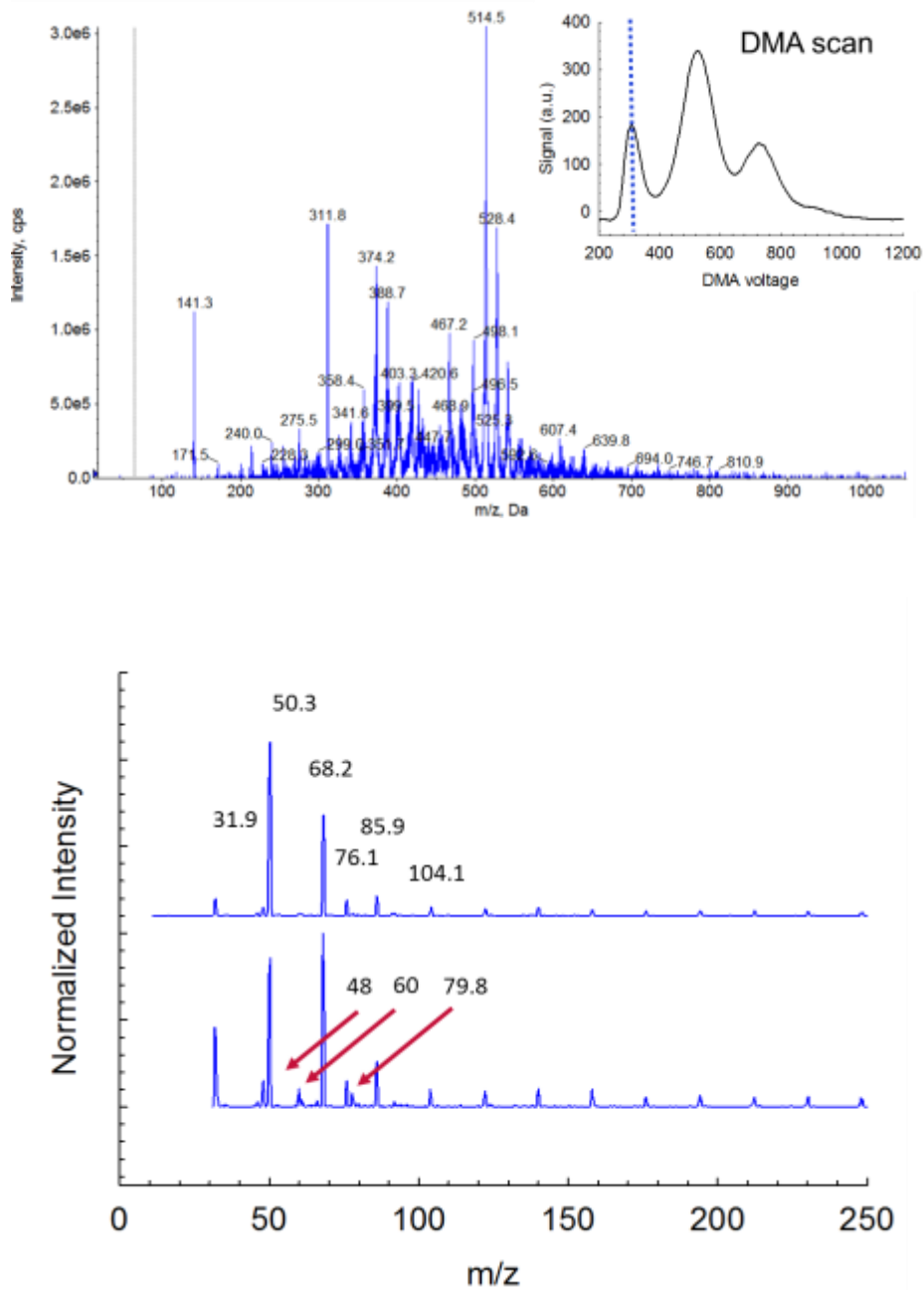


Figure I.6: Resulting mass spectra at a fixed mobility for positively charged (top) and negatively charged (bottom) ions in a flame aerosol reactor for TiO₂ cluster formation as measured through tandem ion mobility mass spectrometry using an API 2000 quadrupole mass spectrometer to obtain mass spectra.

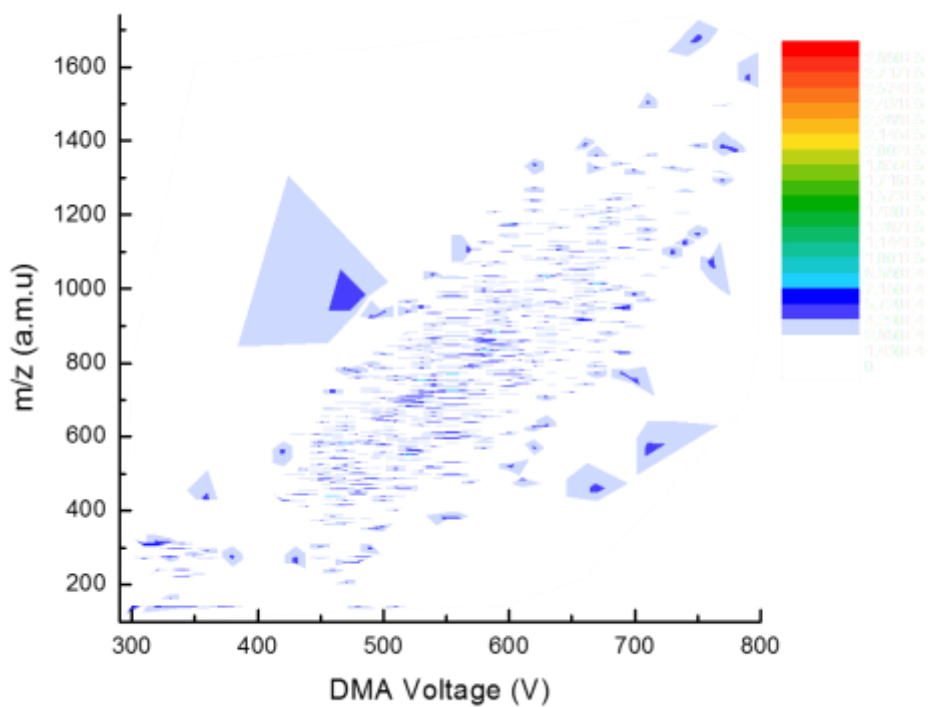


Figure I.7: Contour plot of mass spectra measured over a range of mobilities for clusters of TiO_2 as measured using tandem ion mobility mass spectrometry. Increased DMA voltage indicates larger clusters (based on mobility diameter).

Appendix II: Thermochemical Data

Enthalpy of formation data for precursor conversion of TTIP [1,2] and TEOS [3,4,5] obtained from previous literature is presented in table AII.1

Table AII.1: Enthalpy of formation for TTIP and TEOS intermediates

Species	$\Delta_f H_{298.15K}^o$ [Kj/mol]
Ti(OC ₃ H ₇) ₄	-1507.9
Ti(OC ₂ H ₅) ₄	-1363.50
Ti(OH) ₄	-1268.60
TiO ₂	-305.43
TiO	54.39
Ti(OH) ₃	-898.6
SiH ₃ (O)	20.08
SiH ₃ (OC ₂ H ₅)	-276.56
Si(O)(OH) ₃	-981.57
Si(OH) ₄	-1342.23
Si(OH)(OCH ₃) ₂	-706.68
Si(OH) ₂ (OCH ₃) ₂	-1259.38
Si(OH) ₃ (OC ₂ H ₅)	-1340.97

References:

- [1] Buerger, P. Nurkowski, D., Akroyd, J., Mosbach, S., Kraft, M., First principles thermochemistry for the thermal decomposition of titanium tetra-isopropoxide, ISSN 1473 – 4273, (2015) Cambridge
- [2] M. W. J. Chase. NIST-JANAF Thermochemical Tables, 4th Edition. American Institute of Physics, (1998) New York.
- [3] W. Phadungsukanan, S. Shekar, R. Shirley, M. Sander, RH. West, M Kraft. First-Principles Thermochemistry for Silicon Species in the Decomposition of Tetraethoxysilane, ISSN 1473 – 4273, (2009) Cambridge,
- [4] M. D. Allendorf, C. F. Melius, P. Ho, and M. R. Zachariah. Theoretical study of the thermochemistry of molecules in the Si-O-H system. *J. Phys. Chem.*, 99 (1995) 15285–15293.
- [5] P. Ho and C. F. Melius. Theoretical study of the thermochemistry of molecules in the Si-O-C-H system. *J. Phys. Chem.*, 99 (1995) 2166–2176.

Appendix III:

Controlled Studies on Aerosol Formation during Biomass Pyrolysis in a Flat Flame Reactor

Note: the results here were published in:

Fang, Jiayi, Anna Leavey, and Pratim Biswas. "Controlled studies on aerosol formation during biomass pyrolysis in a flat flame reactor." *Fuel* 116 (2014): 350-357

III. 1 Abstract

A methane-air flat flame reactor was designed to study the initial stages of combustion through flash pyrolysis of biomass and factors contributing to particulate emissions were examined. Six different types of biomass, *Prosopis juliflora*, cotton stalk, poplar, applewood, oak, and cherry wood were pyrolyzed in a methane-air flat flame at various moisture contents. Particulate matter formed was characterized through measuring mass, and particle number size distributions. The moisture content of biomass feed stock was varied from 0%-20% , while the particle feed sizes were maintained at 105 μm or below, to limit heat transfer effects in the particle. Thermo-gravimetric Analysis was also conducted on the biomass to obtain mass fraction data (% volatiles, moisture content) along with kinetic data. Results indicated that the presence of moisture causes a delay in devolatilization thus decreasing the overall efficiency in combustion. The results from this study can be used to optimize biomass combustion for use as fuel in household settings to minimize negative impacts due to poor air quality.

III.2 Introduction

There has been renewed interest in recent decades over the role that biomass will play in enabling us to meet our growing energy demands while at the same time facilitating our carbon reduction and renewable energy targets. In fact, biomass is considered to be the renewable energy source with the highest future energy potential [1]. Biomass is a renewable energy source that is accessible and widely available while providing fuel stability [2]. It also offers versatility as an electrical or heat energy source as well as a transport fuel and an additive for chemical feed stock [2]. Political and environmental concerns are mitigated because of its CO₂ neutrality, provided it is grown and harvested sustainably [3]. Although biomass is increasingly being used for large-scale commercial processes [1, 4, 5], by far the largest consumers of biomass are small-scale domestic users. Almost 3 billion people throughout the developing world burn 2 million tons of biomass daily, in traditional cookstoves and open fires to cook their food and keep warm [6]. The vast majority of these people live in rural areas and are among society's poorest [7]. The poor indoor air quality that is a direct result from these biomass combustion emissions leads to an estimated 2 million deaths per year, especially among women and children [6]. Improving the efficiency of biomass combustion during the initial stages of combustion may result in reduced particulate formation thus improved air quality, and improve the lives of millions of people around the world.

Biomass combustion is a multistep process which includes the heating up, drying, devolatilization, and oxidation of volatiles and char. When incomplete combustion occurs, pollutants will form. Factors influencing the overall efficiency of biomass combustion include the stoichiometric air/fuel ratio, moisture content of the wood, ambient temperature, stove temperature, and mixing. Previous studies examining cookstove performance have established

that the presence of moisture in the wood effects generate PM_{2.5} emissions during the combustion process, even with better air/fuel mixing [8]. These include NO_x, SO_x, soot, smoke, unburned hydrocarbons, Cl compounds, and particulate metal aerosols, which form by nucleation, condensation, coagulation chemical reactions [9]. The release of pollutants in biomass combustion must be managed with care as to mitigate environmental and health impacts.

Several reviews have focused on biomass pyrolysis and combustion with regards to energy generation [10, 11] and pollutant formation [9, 12-16]. Pyrolysis occurs at the initial stages of combustion and is the solid thermal degradation in the absence of oxidizing agents and can be used for thermochemical conversion [11]. Due to the complexity and diversity of available biomass, the content and classification of biomass fuel is important. Conventional solid biomass fuels include wood, straw, and agricultural residues often in the form of chips, pellets, and pulverized fuels. The major chemical components of biomass are hemicellulose, cellulose, and lignin, where the ratio of each may affect tar formation and subsequent pollutant emissions [17]. Some of the minor nutrients present in biomass include N, P, K, Ca, Mg, Na and Si which can contribute to secondary catalytic reactions. [18, 19]. Simplified methods of classification have been utilized using elemental compositions based on the van Krevelen diagram [20].

The initial stages of combustion directly affect overall combustion efficiency and can be studied by examining pyrolysis. Products from pyrolysis include permanent gases (CO₂, H₂, CO, H₂O), aromatic tars, light hydrocarbons, and char [21]. Over the past several decades many types of pyrolysis mechanisms have been proposed for the purpose of thermochemical conversion [22]. The pyrolysis conversion efficiency can depend on factors such as the temperature, biomass

composition, pressure, and heating rate. Such factors have been used to classify pyrolysis. For example, the external heating conditions of pyrolysis can be classified as conventional pyrolysis, fast pyrolysis, and flash pyrolysis. Detailed parameters regarding these operating conditions have been summarized by Babu [10]. Previous studies regarding biomass pyrolysis have classified interparticle pyrolytic conditions into three main regimes: thermally thick, thermally thin, and pure kinetic [23] depending both on the heating rate and particle size.

Char formation in biomass pyrolysis under conventional and fast pyrolysis has been studied extensively for use with energy generation applications. In addition, devolatilization studies using flat flames have examined ignition characteristics for coal particles and the effect of particle diameter and heating rate [24]. Methane-air flat flames are ideal for studying the initial stages of combustion due to its short residence time and ability to achieve high heating rates. In addition, the devolatilized fraction, char yields, and evolution of char textures were examined in a flat flame by Therssen et al. [25]. Similar studies for sawdust pyrolysis in an atmospheric flat flame reactor compared char and volatile yields to devolatilization models while taking into account tar cracking [26]. Flat flames are ideal for studying flash pyrolysis due to the high heating rate, uniform flame temperature; ignition and pyrolysis can be studied without the influences of the flame [25].

Previous studies in biomass pyrolysis were primarily concerned with predicting char and tar yields and have not used flat flames to examine particle formation in biomass pyrolysis. Pollutant formation mechanisms in the initial stages of combustion have not been extensively examined. The beginning stages of combustion significantly affect the overall combustion efficiency and have a direct effect on the downstream pathways leading to pollutant formation.

This study aims to understand particle formation during the initial stages of combustion, namely under flash pyrolysis conditions for various types of biomass and moisture contents. In addition TGA was utilized to examine the kinetics of devolatilization for various fuel types, heating rates and moisture contents.

III.3 Experimental Methods

Experiments were conducted for six fuel types: applewood, cherrywood, cotton stalk, *Prosopis juliflora*, poplar, and oak. Results from proximate analysis are presented in Table III.1. Particle formation during biomass pyrolysis was examined in a premixed methane-air flat flame reactor (Figure II.1). The stainless steel burner head (diameter 38.0 mm) was packed with small stainless steel balls (diameter 2 mm) used to promote mixing, prevent the burner head from heating up, and to reduce the risk of flashback. The honeycomb burner nozzle was comprised of 207 separate holes with a diameter of 0.8 mm. Flow rates were 0.12 and 2.4 lpm for methane and air respectively, and controlled by MKS 1179A mass flow controllers. In order to maintain thermally thin pyrolysis conditions, raw, unburned biomass particles were kept under 105 μm by grinding samples in a IKA M20 Analytical Mill and sieved using a 105 μm mesh (Precision Eforming LLC., Cortland, NY). Particles were fed into the flame using a syringe pump (Harvard Apparatus, Holliston MA) and entrained using nitrogen flow (1 lpm) and fed axially in the methane-air flat flame using a concentric feeding tube in the center of the flame at a mass flow rate of 1 g hr⁻¹ (Figure III.1). Sampling was performed 120 mm above the flat flame and particle number size distributions were measured using a TSI 3080 Scanning Mobility Particle Sizer (SMPS) along with a TSI 3076 Condensation Particle Counter (CPC). The SMPS measures particle size distributions by classifying aerosols based on their electrical mobility while the condensation particle counter measures the total particle count per unit volume.

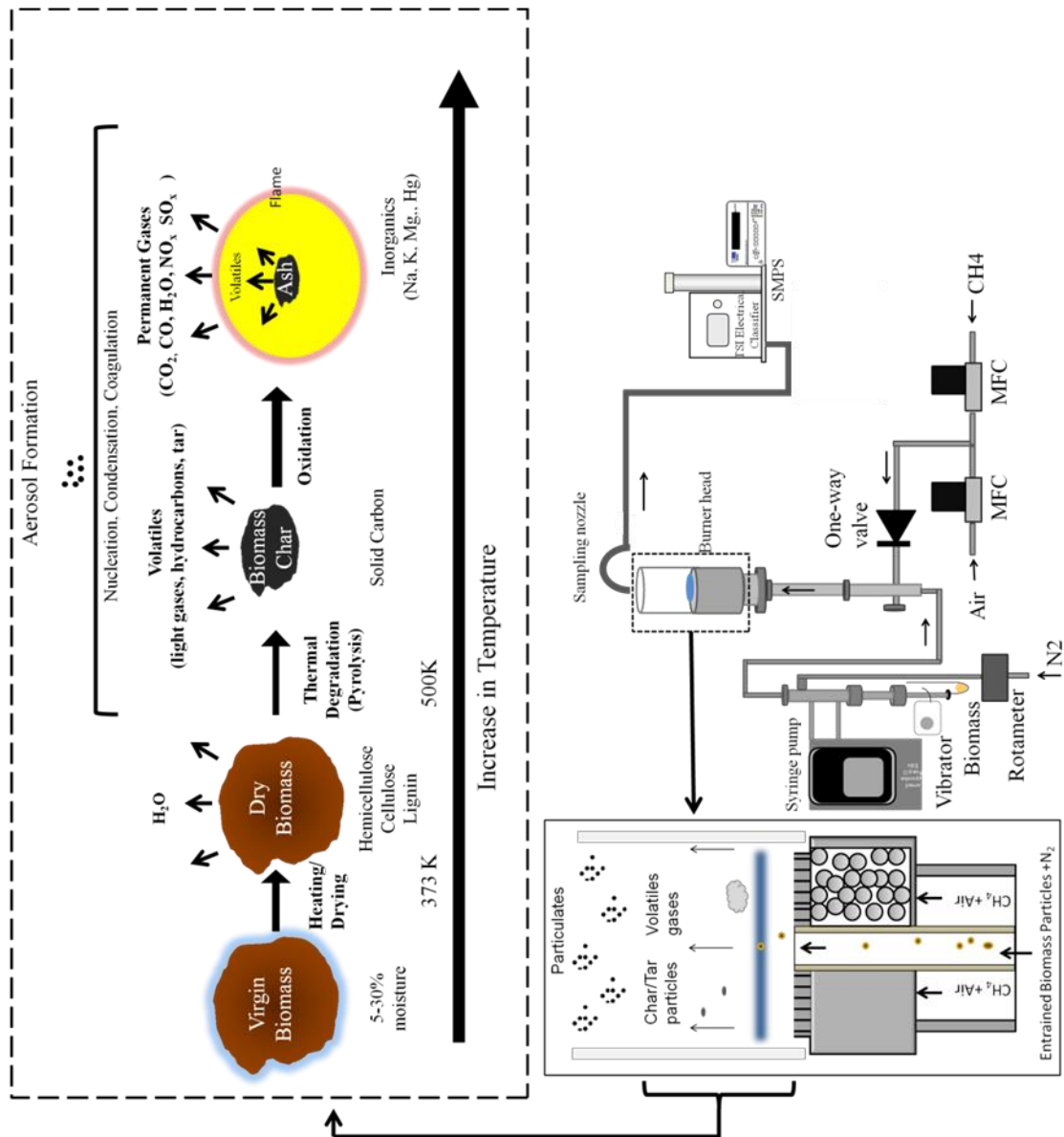


Figure III.1: Experimental setup of the flat flame for measuring particle size distributions with mechanisms of biomass combustion.

Table III.1: Proximate analysis of fuel

Fuel	Ash Content	Fixed Carbon	Volatile Matter	Moisture Content
Applewood	1.63	13.88	84.49	5.93
Cherrywood	0.074	15.51	84.41	5.99
Cottonstalk	6.01	20.16	83.34	8.69
<i>Prosopis juliflora</i>	4.60	19.82	75.60	6.71
Poplar	4.09	12.33	83.56	9.6
Oak	0.25	14.73	85.02	6.25

A TA Instruments Q5000IR apparatus was used to perform thermogravimetric analysis (TGA). The resolution for this apparatus was $< 0.1\mu\text{g}$ and could measure sample weights up to 100mg. Sample weights varied from 15-30 mg while high purity nitrogen was continuously purged at a rate of 150ml min^{-1} through the sample chamber to remove air and volatiles. A series of TGA experiments were run to examine pyrolysis kinetics. Moisture content was determined by ramping the temperature at a constant heating rate to 380 K and then holding the temperature isothermal for 40 minutes to ensure complete moisture evaporation followed by continuous ramping to 1173 K to ensure complete devolatilization. Moisture content was determined by taking the mass fraction at 380 K while the char content was evaluated by taking the mass fraction at 1173K. In addition, the effect of heating rate was examined by varying the heating rate of dry *Prosopis juliflora* from 50 K min^{-1} to 400 K min^{-1} . The delay in moisture was examined by rapid heating of high moisture and low moisture biomass and comparing the weight % and DTG curves. Finally the kinetic parameters were determined by Hi-Res Modulated TGA with a resolution of $1.0 \pm 2\text{ K}$ every 200 s. The experimental plan is summarized in Table III.2.

Table III.2: Experimental plan for thermogravimetric analysis

Experiment type	Fuel Type					
	Applewood	Cotton stalk	<i>Prosopis Juliflora</i>	Poplar	Oak	Cherrywood
1 Ambient (5-10%)	Y	Y	Y	Y	Y	Y
2 Oven-dried (<5%) and high (20%)	Y					
3 15°C/min	Y	Y	Y	Y	Y	Y
4 Varying the heating rate (15 to 400°C /min)			Y			
5 Modulated TGA	Y	Y	Y	Y	Y	Y
6 Varying moisture content (5-20%)	Y					

III.4 Mechanistic Devolatilization Kinetics Using Thermogravimetric Analysis

The steps of biomass combustion begin with the initial heating of the fuel and are followed by dehydration, fuel devolatilization (pyrolysis) into carbonaceous char and volatiles, and oxidation of volatiles and char. A detailed schematic of biomass combustion is illustrated in Figure III.1. Moisture evaporation occurs during the initial heating phase and is complete by 373 K. At approximately 500 K pyrolysis begins and significant weight loss will occur due to the release of volatiles where the main products are char, tar, volatiles, CO₂ and CO. The main products of pyrolysis are then oxidized to form residual ash, CO₂, NO_x, SO_x, and other pollutants. Moisture loss and pyrolysis are endothermic processes whereas char and volatile oxidation is exothermic [27]. Previous studies regarding each step of biomass combustion have been performed with varying degrees of detail and complexity [28, 29]. Upon closer examination of pollutant formation, it has been shown that aerosols from biomass burning are formed

primarily due to incomplete combustion [30]. Clearly, the initial stages of combustion are critical in determining the overall pollutant formation.

Detailed pyrolysis mechanisms of parallel and consecutive reactions have been proposed while it has been shown that the formation of tar and char may be competitive [31]. Simplified models assuming a global single stage process have also been utilized [32]. Many pyrolysis mechanisms have been suggested for the decomposition of volatiles with the most common model assuming a parallel independent decomposition of three main constituents, cellulose, hemicellulose, and lignin. Cellulose molecules are long chain linear polymers consisting of 7000-12,000 β -D glucospyranose monomers that begin to decompose from 570-660 K. Hemicellulose molecules are polysaccharides with monomers with 5-6 monosacharide units and decompose around 498-598 K. Lignin consists of irregular phenylpropane monomers and decomposes from 523-773 K [33-35]. Due to the overlap in temperature ranges, it is difficult to identify the pyrolysis curves of each component while at higher temperatures and heating rates, simultaneous decomposition will occur.

At more severe heating conditions and higher heating rates, different components of biomass pyrolysis tend to merge thus flash pyrolysis conditions can merit the use of single reactions to predict product formation. This can be attributed to the decrease in competition between liquid tar and gas volatile formation during pyrolysis [32, 36-38]. A simplified global single component mechanism has been assumed where dry biomass decomposes into char and volatiles.

Mathematical representations of devolatilization can be written as a first order reaction:

$$\frac{d\alpha}{dt} = K(1 - \alpha) \quad (1)$$

where K is the global kinetic rate constant and α (%) is the normalized mass fraction. The mass fraction, α , can be determined by taking the difference between the current mass and final mass and normalizing it with the difference between the initial and final mass. The pre-exponential factor K exhibits a temperature dependence which can be represented by the Arrhenius equation

$$K = Z \exp\left(\frac{-E}{RT}\right) \quad (2)$$

where Z is the pre-exponential factor at a given temperature, T is the temperature of interest, E is the activation energy in KJ mol^{-1} , and R is the ideal gas constant. Traditional TGA experiments utilize linear temperature ramps while determination of activation energy can require conducting multiple TGA experiments at various heating rates. Continuous kinetic data can be obtained by modulating the linear temperature profile using sinusoidal oscillations in a technique called modulated TGA[39]. In addition dynamic heating rates at high resolutions can be coupled with modulated TGA to obtain more reproducible results. Kinetic parameters such as the activation energy, E , and pre-exponential factor, Z , can be obtained by comparing the peaks and valleys of neighboring peaks in a sinusoidal signal based on the following expressions:

$$E = \frac{R(T^2 - A^2) \ln\left(\frac{d\alpha_p}{d\alpha_v}\right)}{2A} \quad (3)$$

$$\ln(Z) = \ln\left(\frac{\Delta\alpha}{1-\alpha}\right) + \frac{E}{RT} \quad (4)$$

where T is the average temperature of the oscillation while A is the amplitude of oscillation. The conversion values of the valleys and peaks are represented by α_v and α_p , respectively. This is an empirical approach and does not make any assumptions regarding the specific chemical mechanisms of devolatilization and measures the global activation energy.

III.5 Results and Discussion

The initial stages of combustion are critical in influencing the downstream processes of particle formation. First the results from TGA studies will be presented examining the devolatilization curves for various types of biomass fuels, increasing heating rates, and moisture levels. TGA studies will be used to understand fundamental properties of biomass pyrolysis. Finally results from flat flame experiments will be used to study particle formation during the initial stages of combustion. Results from both types of experiments will then be discussed in relation to each other.

III.5.1 Devolatilization Kinetics

Thermogravimetric experiments were performed to examine the devolatilization of various types of biomass. Figure III.2 displays weight percentages and derivative thermogravimetric (DTG) curves comparing applewood, cherrywood, cottonstalk, *Prosopis juliflora*, poplar, and oak with a constant heating rate of 15 K min^{-1} . Qualitative analysis of the plots reveals three distinct regions of devolatilization: evaporation region, main pyrolysis region, and termination region. The evaporation of moisture occurs from 330 to 380 K. The second region is the main pyrolysis region with its onset beginning at approximately 470 K and terminating at about 700-750 K for higher heating rates [40, 41]. Qualitatively, DTG curves can be described to show the

presence of an initial hemicellulose shoulder for pyrolysis due to the peak rates of hemicellulose devolatilization occurring at lower temperatures than the overall peak devolatilization. A DTG peak associated with cellulose pyrolysis follows and ends with a rapid decrease of pyrolysis rate to near zero after 750 K. The tail present in the DTG curves is due to lignin which has a wider range of devolatilization. As the heating rate increases, these characteristic peaks will become less discernible. More details regarding the effect of higher heating rates will be elucidated in section II.5.2.

Several key kinetic parameters determined by TGA and modulated TGA analysis describing biomass pyrolysis are summarized in Table III.3. The peak devolatilization temperature T_m is the temperature at which the peak devolatilization rate, DTG_m , occurs. Both T_m and DTG_m are useful in examining the changes in the fuel reactivity for various types of fuels and heating conditions. For the six types of fuel, peak devolatilization rates ranged from 10.43-16.52 % min⁻¹ at temperatures from 594 K to 649 K (Table III.3). From Figure III.2b, an initial shoulder can be observed in the DTG curve indicating local maxima associated with hemicellulose devolatilization. This shoulder is most pronounced for cherrywood at 293 K while it is not observable for cottonstalk indicating a more significant fraction of the devolatilization occurring due to cellulose in cottonstalk. For all types of biomass, low rates of thermal decomposition beyond 973 K can also be observed which is characteristic of lignin pyrolysis while the final char yield at slow heating rates ranged from 11.39% to 28.30% (Table III.3). Even under the same heating conditions, there are differences in the devolatilization characteristics for different types of biomass.

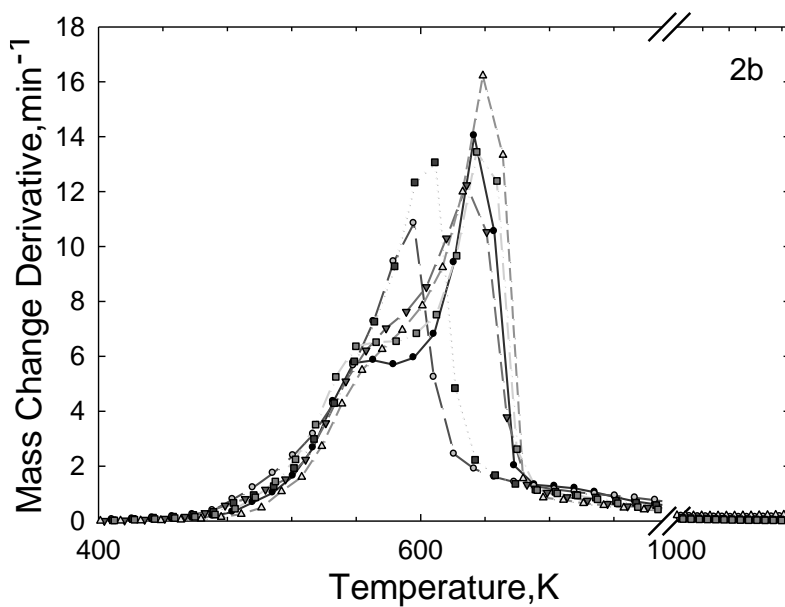
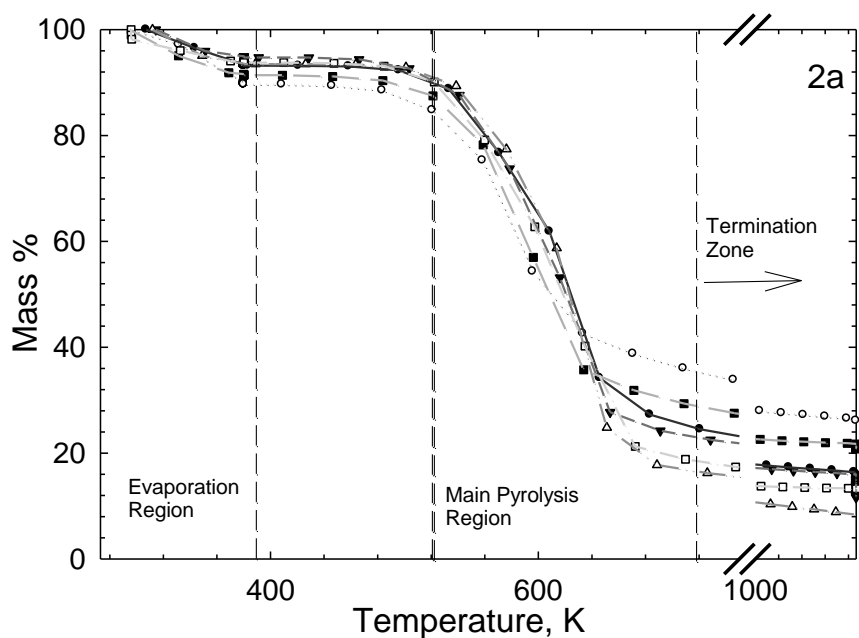


Figure III.2: Thermogravimetric mass % (2a) and DTG (2b) curves comparing applewood(▼), cottonstalk(○), Poplar(△), *Prosopis juliflora*(■), Cherrywood(●), Oak(□) at a constant heating rate of 15 K min⁻¹

Kinetic parameters such as the activation energy and pre-exponential factor were obtained from modulated TGA experiments. Measured activation energies averaged over the main pyrolysis zone ranged from 133 to 158 kJ mol⁻¹ for the six types of biomass fuels (Table III.3). Although several other techniques such as the Friedmann method [42], Flynn-Wall-Ozawa method [43], and Kissinger [44] method have been used to determine the activation energy, they require multiple TGA experiments at various heating rates. Hi-Resolution modulated TGA has been used successfully for biomass fuels to obtain kinetic parameters without theoretical assumptions or prior mathematical modeling [45]. Different types of fuels exhibit variations in key kinetic parameters which play a more significant role during the initial stages of combustion. The combustion of volatiles is a key step in the formation of aerosols such as tars, PAH, soot, and VOC's while the pathways to the formation of pollutants is directly affected by the rate of devolatilization. Subsequently, when complete oxidation reactions have yet to occur, the rapid release of volatiles promotes aerosol formation through nucleation, condensation and coagulation of volatiles, char, and tar which has direct effects on the mixing and rates of volatile oxidation. Because volatiles are primarily responsible for particle formation in pyrolysis, understanding differences in devolatilization characteristics between different types of biomass are critical in studying the overall pollutant formation mechanisms in biomass combustion. the variations observed through TGA experiments for biomass pyrolysis indicate that the initial stages of combustion are critical to understanding the formation of particulates.

III.5.2 The Effect of Heating Rate:

Results from TGA experiments comparing various higher heating rates are displayed in Figure III.3. *Prosopis juliflora* was pyrolyzed at 5, 50, 100, 200, and 400 K min⁻¹ in an inert N₂ environment. The peak devolatilization temperature T_m shifted from 577 K for 5 K min⁻¹ to 646 K for 400 K min⁻¹ (Table III.4). Qualitative observation of Figure III.3b shows that at lower heating rates the initial shoulder of hemicellulose devolatilization is discernible. Under slow heating rate conditions, first order, single stage mechanisms may not be sufficient for accurate prediction of biomass pyrolysis conversion [46]. As the heating rate increases, the initial shoulder becomes less discernible as hemicellulose and cellulose are not influenced the same by increasing the heating rate. High temperature reaction pathways become more favored and can be described by the rapid formation of reactive free radicals making the mechanisms of pyrolysis more characteristic of a single component mechanism as the assumption that they react independently may no longer hold [21].

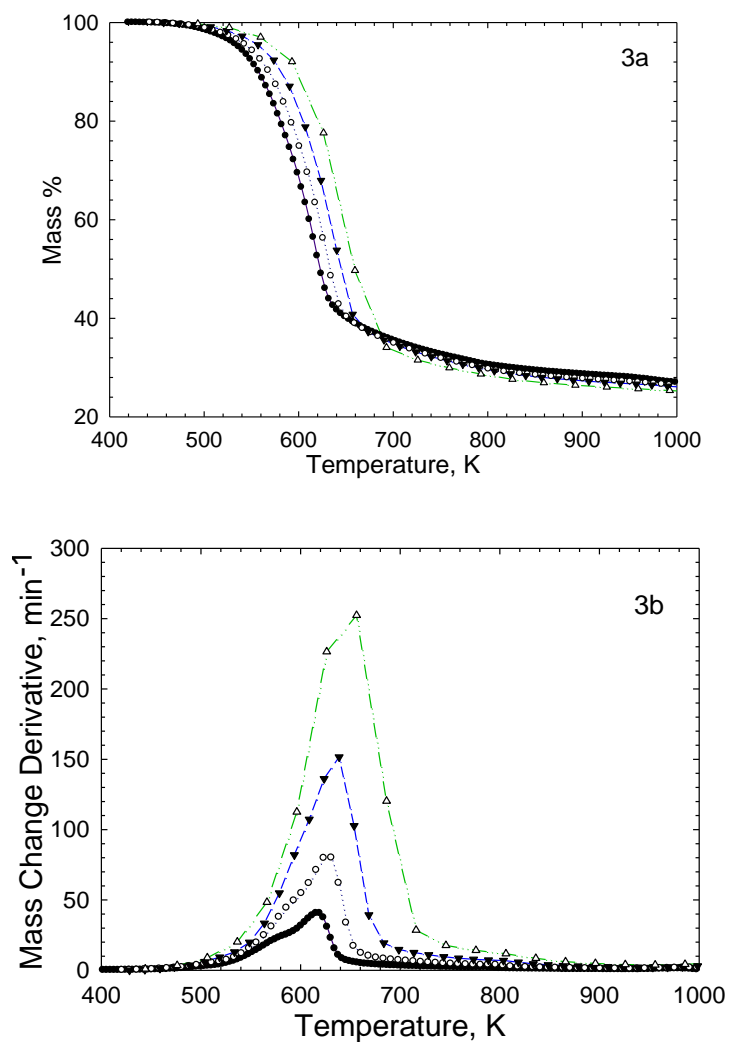


Figure III.3: Mass% (3a) and DTG (3b) curves comparing various heating rates for *Prosopis juliflora* for 50 K min⁻¹ (●), 100 K min⁻¹ (○), 200 K min⁻¹(▼), and 400 K min⁻¹ (△)

In addition, a shift to higher temperatures of the peak devolatilization rate from 577 K to 646 K is observed (Table III.4). Such a thermal lag is consistent with results from other studies and has been attributed to the delay in heat transfer to the sample [47]. As heating rates increase, a

single step devolatilization mechanism can be qualitatively observed showing that global single step rate mechanisms can be used to examining flash pyrolysis of biomass particles during the initial stages of combustion. In addition, it should be noted that 500 K min^{-1} is the highest heating rate achievable by the TGA instrument. The ability to achieve flash pyrolysis conditions is not possible due to limitations in instrumentation. Additionally, at higher heating rates, heat transfer effects are no longer negligible as temperature gradients may develop within the sample resulting from thermal conduction effects, thus smaller sample sizes and more precise instrumentation may be needed to achieve such conditions. Nonetheless, even though the heating rates between the TGA and flat flame are on different scales, the TGA is able to capture the effects of increasing heating rates during biomass pyrolysis. Further examination of more extreme heating rates in the pure kinetic regime would be difficult, especially for obtaining kinetic parameters and warrants more study.

Table III.3: Shift in peak devolatilization at higher heating rates as seen in Figure III.2

Heating Rate, K min^{-1}	Peak, K	Peak rate, $\% \text{ min}^{-1}$
5	577	4.641
50	618	40.78
100	627	81.34
200	637	153.3
400	646	269.5

III.5.3 Effect of Moisture as Measured by TGA

The role of moisture in biomass devolatilization is also examined by introducing rapid heating rates for fuels with various moisture contents and observing their behavior. Figure III.4 compares the devolatilization of applewood for high (~20%) and ambient (5%) moisture levels at 200 K min⁻¹ and 400 K min⁻¹. At 200 K min⁻¹, higher moisture content results in a delay in the peak devolatilization from 625 K to 631 K. A delay in devolatilization can be expected since drying is an endothermic process while the presence of water vapor may also have a cooling effect. As the moisture content increases, more energy and time will be required to increase the temperature extending conversion times [48]. In addition, the presence of moisture delays devolatilization by decreasing the pyrolysis temperature and through convective cooling by the presence of water vapors [49, 50]. Water can be present in biomass in three forms: water in pores, capillary water, and bound water [51]. Once the moisture content reaches approximately 30%, there are no more molecular sites for water to bind; this point is commonly referred to as the fiber saturation point. Mathematical models have been employed to characterize liquid and gas phase biomass particle drying and have demonstrated that at high heating rates, gas phase transport dominates the drying process [52].

At 400 K min⁻¹ the opposite effect seems to occur where T_m in fact shifts to lower temperatures from 362.6 K to 535.4 K when increasing the moisture to 20%. Similar results have been reported by Fanfei et al. [53] where the peak devolatilization will shift to lower temperatures with increases in initial moisture. These results indicate a potential favorability towards the catalytic pathways of cellulose hydrolysis in the presence of moisture at higher heating rates as evaporation may not be complete when biomass devolatilization begins. Since

these results were obtained in a more well controlled environment, the enhancement of devolatilization observed at 400 K min^{-1} does not necessarily indicate the same effect will be observed in practical combustors since moisture evaporation is dependent on factors such as the fuel dimensions, heating conditions, and type of biomass in addition to the kinetics. Heat and mass transport effects will play a larger role in determining the effect of initial moisture on biomass pyrolysis. In order to fully understand how moisture plays a role during the initial stages of combustion, transport effects must be taken into further consideration.

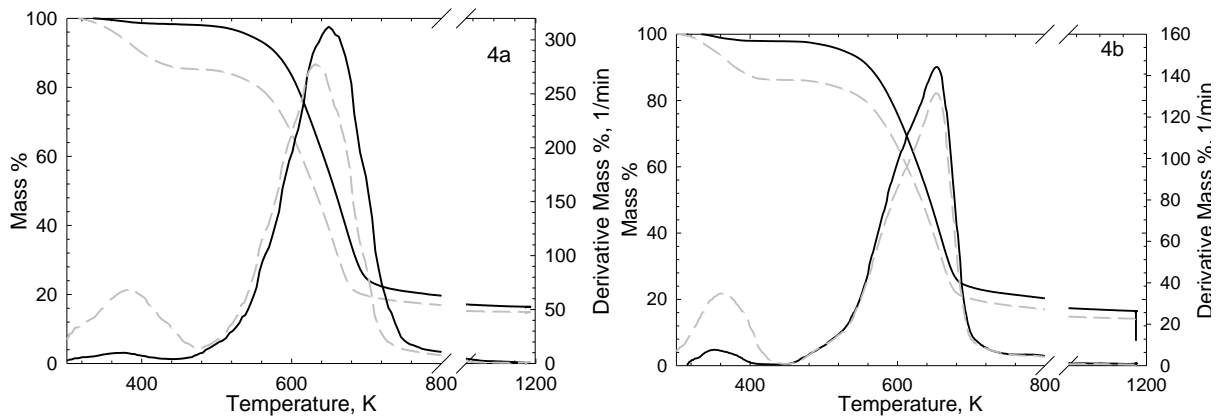


Figure III.4: Devolatilization of applewood particles for oven dry (solid) high moisture (dashed) fuel. Experiments were performed at a heating rate of 200 K min^{-1} (4a) and 400 K min^{-1} (4b)

III.5.4 Particle size distributions for various types of biomass

The measured particle number size distribution data from the flash pyrolysis of biomass in a flat flame are displayed in Figure III.5 for applewood, cherrywood, cottonstalk, oak, poplar, and *Prosopis juliflora*. The geometric mean diameter (d_{pg}), geometric standard deviation (σ_g),

and total number concentration (N_t) are shown in Table III.5. The measured flame temperature was 1073K while the heating rate was estimated at $\sim 5 \times 10^6 \text{ K s}^{-1}$. The geometric mean diameter varied from 58.15 nm (oak) to 112.91 nm (cherrywood) while the total number concentration ranged from 1.26×10^7 to $3.46 \times 10^7 \text{ # cc}^{-1}$. Measured particle size distributions are typical of ultrafine mode and accumulation mode aerosols formed through nucleation, coagulation, and condensation. Comparison of TGA kinetic parameters (Table III.3) and measured particle size distribution measurements (Table III.5) for different types of biomass does not yield a clear relationship or trend. This may be partially due to the fact that the time scales of devolatilization in TGA experiments are orders of magnitude larger than the time scales in the flat flame reactor while the physical processes of particle formation are not accounted for in TGA analysis. Although differences in the particle number size distributions can be observed between the types of biomass in the flat flame reactor and in TGA experiments, the direct effects on particulate formation still merit further consideration.

Table III.4: Key kinetic parameters of devolatilization as measured by TGA (Figure III.2) and modulated TGA

Fuel Type	$\log[A(\text{min}^{-1})]$	E_a (KJ mol ⁻¹)	Shoulder Temperature (°C)*	Peak Temperature (°C)*	Peak rate (min ⁻¹)*	Char Yield (Dry Basis)*
Applewood	11.90	134.55	582	626	11.43	17.04
Cherrywood	11.73	153.76	566	636	14.46	17.56
Cottonstalk	12.611	139	Na	594	10.43	21.46
<i>Prosopis Juliflora</i>	12.82	139.13	560	595	11.39	28.30
Poplar	11.65	158	573	646	16.52	11.39
Oak	11.74	133.64	566	640	14.22	14.15

Figure III.6 examines the particle size distribution for various levels of moisture for applewood. As moisture increased, the geometric mean diameter for applewood decreased to 59.89 nm while the total number concentration also decreased from 2.36×10^7 to 1.48×10^7 # cc⁻¹ indicating the presence of moisture suppressed devolatilization. The observed decrease in particle formation could be caused by two mechanisms. First, the presence of moisture will result in lower pyrolysis conversions due to the latent heat of water vaporization. As a result, for the same reaction time, there will be less volatiles released and a decreased rate of particle formation. The second mechanism is caused by the transport properties of fast evaporation. Under flash pyrolysis conditions such as in the flat flame, it can be assumed that fast drying occurred. During fast drying, the transport of convective gas phase vapors is very high and the increased presence of water vapor will decrease the overall pyrolysis temperature.

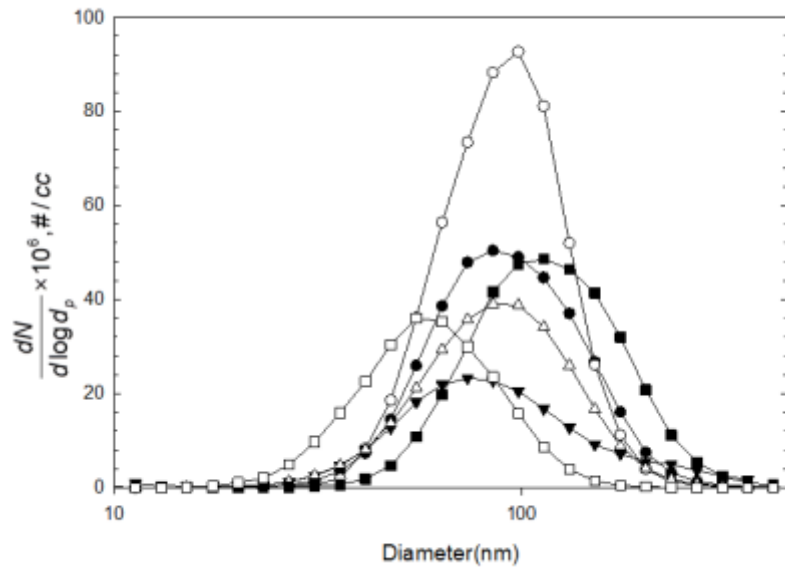


Figure III.5: Measured size distributions for various types of fuel comparing applewood(●), cottonstalk(○), Poplar(▼), *Prosopis juliflora*(△), Cherrywood(■), Oak(□)

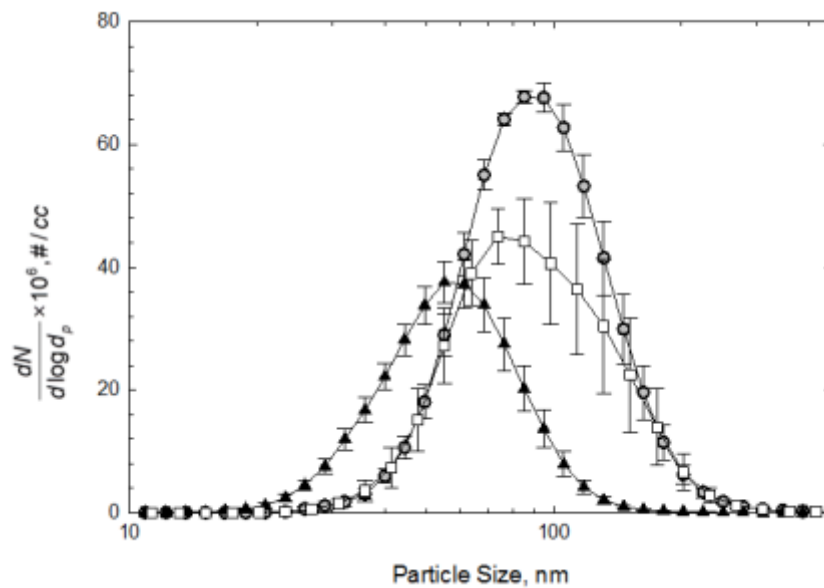


Figure III.6: Measured size distributions for high moisture applewood(▲), ambient moisture applewood(□), and oven dried applewood(●).

Table III.5: Size distribution statistics regarding for measured size distributions

Fuel type	GDM (nm)	GSD ₁	Nt (#/cc)
Cherrywood	112.91	1.45	2.39x10 ⁷
Cotton Stalk	88.72	1.39	3.46x10 ⁷
<i>Prosopis Juliflora</i>	85.6	1.45	1.81x10 ⁷
Poplar	84.63	1.69	1.26x10 ⁷
Oak	58.15	1.45	1.52x10 ⁷
Applewood	89.78	1.4	2.36x10 ⁷
Oven Dry Applewood	89.72	1.43	2.81x10 ⁷
High Moisture Applewood	59.89	1.44	1.48x10 ⁷

The relationship between aerosol formation during the initial stages of biomass combustion may not be entirely intuitive and merits some discussion. The effect of suppressed particle formation during the initial stages of biomass should not be confused with an overall decrease in pollutant emissions or higher combustion efficiencies. In the absence of excess oxygen, the flat flame only examines the initial pyrolysis stage. In a complete combustion flame, the byproducts of pyrolysis typically will undergo oxidation immediately after pyrolysis. The oxidation of volatiles will depend on various properties such as degree of mixing, temperature of the mixture, presence of condensed tars, and the composition of volatiles. In addition remaining solid char will also undergo oxidation in the flame. A key difference between pyrolysis and oxidation is that oxidation is highly exothermic and self sustaining. As the combustion reaction progresses, the energy from volatile and char burning will in turn heat the unpyrolysed fuel. Increased mixing between the fuel and oxidant can be encouraged by maximizing the release of volatiles in the gaseous phase. Suppressed particle formation in the flat flame is an indication that fewer volatiles were released from the fuel since a higher volatile concentration in the reactor will result in increased rates of nucleation. Thus the mechanisms responsible for a decrease in combustion efficiency begin during the initial stages of biomass combustion, namely pyrolysis. It has been demonstrated that at this stage factors such as fuel type and moisture level will effect pyrolysis conversion in biomass and therefore affect the downstream combustion efficiency.

III.5.5 Conclusions

Comparison of results from thermogravimetric analysis (TGA) and flat flame experiments show that both systems complement each other when studying combustion at fundamental scales. While the TGA provides a well controlled environment to carefully study

pyrolysis kinetics for various types of fuels and heating conditions, the flat flame can examine how these factors affect particle formation. Results for both the TGA and flat flame have demonstrated that the pyrolysis of biomass can vary significantly depending on the fuel type while the presence of moisture acts to suppress devolatilization. In addition using the flat flame and TGA permits the initial stages of combustion at different heating rates, length scales, and in pyrolysis environments to be examined.

The kinetics of pyrolysis was examined in a TGA to study the variation between six types of biomass fuel and the effects of increased moisture content. At slow heating rates of 15 K min^{-1} , the weight loss and derivative thermogravimetric curves were compared for various types of fuel. Differences were observed for the peak heating rates, heating temperatures and final char yields. In addition, modulated TGA was used to determine the average activation energy and pre-exponential parameters. Measured activation energies ranged from 133 to 158 kJ mol^{-1} while the pre-exponential factor ranged from 11.49-13.96 $\log [A \text{ min}^{-1}]$. These results demonstrate that differences in the type of biomass are apparent at the initial stages of combustion. Increasing the heating rate resulted in a shift in the peak devolatilization temperature from 577 K for 5 K min^{-1} to 646 K for 400 K min^{-1} while higher heating rates were more characteristic of single step mechanisms. Initial moisture in the biomass seemed to have a compound effect on the kinetics of devolatilization causing both a shift in the peak devolatilization to higher temperatures at 200 K min^{-1} while slightly enhancing devolatilization at 400 K min^{-1} . At higher heating rates in TGA, heat transfer effects may begin to have an effect on the kinetics of devolatilization thus further study into heat and mass transport should be considered.

Flash pyrolysis of biomass in a flat flame reactor was also studied to examine the same factors affecting pyrolysis. Particle number size distributions were measured in a flat flame reactor for six types of fuels while the moisture levels were varied for one type of fuel. Similar trends observed in TGA studies were also demonstrated in the methane-air flat flame reactor. The size distributions varied depending on the fuel type while increases in moisture suppressed particle formation indicating a lower overall pyrolysis efficiency. These results help elucidate how the initial stages of combustion are critical in determining the overall downstream combustion efficiency. Different types of biomass and varying moisture levels effect overall particulate formation, however a further examination of the transport phenomena is needed to establish clear relationships between the kinetics and pollutant formation. In the future results from this study can be used to generate simple cook stove models to predict particle formation. In addition more detailed studies should be performed on the transport and kinetics of oxidation following the products of pyrolysis.

III.5.6 References

- [1] M.F. Demirbas, M. Balat, H. Balat, Potential contribution of biomass to the sustainable energy development, *Energy Conversion and Management*, 50 (2009) 1746-1760.
- [2] P. McKendry, Energy production from biomass (part 1): overview of biomass, *Bioresource Technology*, 83 (2002) 37-46.
- [3] H. McKay, Environmental, economic, social and political drivers for increasing use of woodfuel as a renewable resource in Britain, *Biomass Bioenerg.*, 30 (2006) 308-315.
- [4] A. Evans, V. Strezov, T.J. Evans, Sustainability considerations for electricity generation from biomass, *Renewable & Sustainable Energy Reviews*, 14 (2010) 1419-1427.
- [5] A. Williams, J.M. Jones, L. Ma, M. Pourkashanian, Pollutants from the combustion of solid biomass fuels, *Prog. Energy Combust. Sci.*, 38 (2012) 113-137.
- [6] G. Legros, I. Havet, N. Bruce, S. Bonjour, The energy access situation in developing countries: a review focusing on the least developed countries and Sub-Saharan Africa, UNDP & WHO, New York, (2009).
- [7] WHO, Fuel for Life: Household Energy And Health, Stylus Pub Llc, 2006.
- [8] M. Sahu, J. Peipert, V. Singhal, G.N. Yadama, P. Biswas, Evaluation of Mass and Surface Area Concentration of Particle Emissions and Development of Emissions Indices for Cookstoves in Rural India, *Environ. Sci. Technol.*, 45 (2011) 2428–2434.
- [9] J.S. Lighty, J.M. Veranth, A.F. Sarofim, Combustion aerosols: Factors governing their size and composition and implications to human health, *J. Air Waste Manage. Assoc.*, 50 (2000) 1565-1618.
- [10] B.V. Babu, Biomass pyrolysis: a state-of-the-art review, *Biofuels, Bioproducts and Biorefining*, 2 (2008) 393-414.
- [11] C. Di Blasi, Modeling chemical and physical processes of wood and biomass pyrolysis, *Prog. Energy Combust. Sci.*, 34 (2008) 47-90.

- [12] K.R. Smith, R. Uma, V.V.N. Kishore, J.F. Zhang, V. Joshi, M.A.K. Khalil, Greenhouse implications of household stoves: An analysis for India, *Annual Review of Energy and the Environment*, 25 (2000) 741-763.
- [13] A.D. Sagar, S. Kartha, Bioenergy and sustainable development, in: *Annual Review of Environment and Resources*, 2007, pp. 131-167.
- [14] S.D. Pohekar, D. Kumar, M. Ramachandran, Dissemination of cooking energy alternatives in India - a review, *Renewable & Sustainable Energy Reviews*, 9 (2005) 379-393.
- [15] N.L. Panwar, S.C. Kaushik, S. Kothari, Role of renewable energy sources in environmental protection: A review, *Renewable & Sustainable Energy Reviews*, 15 (2011) 1513-1524.
- [16] B.H. Chen, C.J. Hong, M.R. Pandey, K.R. Smith, Indoor air pollution in developing countries, *World health statistics quarterly. Rapport trimestriel de statistiques sanitaires mondiales*, 43 (1990) 127-138.
- [17] Y. Chen, S. Charpenay, A. Jensen, M.A. Serio, M.A. Wojtowicz, Modeling biomass pyrolysis kinetics and mechanisms, *Abstr. Pap. Am. Chem. Soc.*, 213 (1997) 31-FUEL.
- [18] A. Jensen, K. Dam-Johansen, M.A. Wojtowicz, M.A. Serio, TG-FTIR study of the influence of potassium chloride on wheat straw pyrolysis, *Energy & Fuels*, 12 (1998) 929-938.
- [19] M. NikAzar, M.R. Hajaligol, M. Sohrabi, B. Dabir, Mineral matter effects in rapid pyrolysis of beech wood, *Fuel Process. Technol.*, 51 (1997) 7-17.
- [20] B.M. Jenkins, L.L. Baxter, T.R. Miles, Combustion properties of biomass, *Fuel Process. Technol.*, 54 (1998) 17-46.
- [21] R.J. Evans, T.A. Milne, Molecular characterization of the pyrolysis of biomass, *Energy & Fuels*, 1 (1987) 123-137.
- [22] G. Varhegyi, M.J. Antal, E. Jakab, P. Szabo, Kinetic modeling of biomass pyrolysis, *J. Anal. Appl. Pyrolysis*, 42 (1997) 73-87.
- [23] C. Diblasi, Modeling and Simulation of Combustion Processes of Charring and Non-Charring Solid Fuels, *Prog. Energy Combust. Sci.*, 19 (1993) 71-104.

- [24] M. Taniguchi, H. Okazaki, H. Kobayashi, S. Azuhata, H. Miyadera, H. Muto, T. Tsumura, Pyrolysis and Ignition Characteristics of Pulverized Coal Particles, *Journal of Energy Resources Technology*, 123 (2001) 32-38.
- [25] E. Therssen, L. Gourichon, L. Delfosse, Devolatilization of coal particles in a flat flame—experimental and modeling study, *Combustion and Flame*, 103 (1995) 115-128.
- [26] A.D. Lewis, Sawdust Pyrolysis and Petroleum Coke CO₂ Gasification at High Heating Rates, in: *Chemical Engineering*, Brigham Young University, 2011.
- [27] F. Shafizadeh, The Chemistry of Pyrolysis and Combustion, in: *The Chemistry of Solid Wood*, American Chemical Society, 1984, pp. 489-529.
- [28] T. Abbas, P.G. Costen, F.C. Lockwood, Solid fuel utilization: From coal to biomass, *Symposium (International) on Combustion*, 26 (1996) 3041-3058.
- [29] A. Williams, M. Pourkashanian, J.M. Jones, Combustion of pulverised coal and biomass, *Prog. Energy Combust. Sci.*, 27 (2001) 587-610.
- [30] B.R.T. Simoneit, Biomass burning — a review of organic tracers for smoke from incomplete combustion, *Applied Geochemistry*, 17 (2002) 129-162.
- [31] D.F. Arseneau, Competitive Reactions in the Thermal Decomposition of Cellulose, *Canadian Journal of Chemistry*, 49 (1971) 632-638.
- [32] C. Di Blasi, C. Branca, Kinetics of primary product formation from wood pyrolysis, *Ind. Eng. Chem. Res.*, 40 (2001) 5547-5556.
- [33] F. Shafizadeh, Pyrolytic reactions and products of biomass, *Fundamentals of Biomass Thermochemical Conversion*, (1985) 183-217.
- [34] H.L. Chum, M.M. Baizer, The electrochemistry of biomass and derived materials, *American Chemical Society*, 1985.
- [35] J.M. Ebeling, B.M. Jenkins, Physical and Chemical-Properties of Biomass Fuels, *Trans. ASAE*, 28 (1985) 898-902.

- [36] W.C.R. Chan, M. Kelbon, B. Krieger-Brockett, Single-particle biomass pyrolysis: Correlations of reaction products with process conditions, *Industrials and Engineering Chemistry Research*, 27 (1988) 2261-2275.
- [37] B.M. Wagenaar, W. Prins, W.P.M. van Swaaij, Flash pyrolysis kinetics of pine wood, *Fuel Process. Technol.*, 36 (1993) 291-298.
- [38] T.R. Nunn, J.B. Howard, J.P. Longwell, W.A. Peters, Product compositions and kinetics in the rapid pyrolysis of sweet gum hardwood, *Industrial & Engineering Chemistry Process Design and Development*, 24 (1985) 836-844.
- [39] R.L. Blaine, B.K. Hahn, Obtaining kinetic parameters by modulated thermogravimetry, *J. Therm. Anal.*, 54 (1998) 695-704.
- [40] M.J. Antal, Jr., G. Varhegyi, Cellulose Pyrolysis Kinetics: The Current State of Knowledge, *Ind. Eng. Chem. Res.*, 34 (1995) 703-717.
- [41] D.L. Pyle, C.A. Zaror, Heat transfer and kinetics in the low temperature pyrolysis of solids, *Chemical Engineering Science*, 39 (1984) 147-158.
- [42] H.L. Friedman, Kinetics of thermal degradation of char-forming plastics from thermogravimetry. Application to a phenolic plastic, *Journal of Polymer Science Part C: Polymer Symposia*, 6 (1964) 183-195.
- [43] L.A. Wall, A quick, direct method for the determination of activation energy from thermogravimetric data, *Journal of polymer science. Part B, Polymer letters*, 4 (1966) 323-328.
- [44] H.E. Kissinger, Variation of Peak Temperature with Heating Rate in Differential Thermal Analysis, *Journal of Research of the National Bureau of Standards*, 57 (1956) 217-221.
- [45] W.T. Winter, A.J. Stipanovic, A modulated-TGA approach to the kinetics of lignocellulosic biomass pyrolysis/combustion, *Polymer degradation and stability*, 97 (2012) 1606-1615.
- [46] A. Fantei, L. Tognotti, Effect of the heating rate on the devolatilization of biomass residues, *Thermochim. Acta*, 472 (2008) 55-63.
- [47] P.T. Williams, S. Besler, The influence of temperature and heating rate on the slow pyrolysis of biomass, *Renewable Energy*, 7 (1996) 233-250.

- [48] A.M.C. Janse, R.W.J. Westerhout, W. Prins, Modelling of flash pyrolysis of a single wood particle, *Chemical Engineering and Processing: Process Intensification*, 39 (2000) 239-252.
- [49] W.C.R. Chan, M. Kelbon, B.B. Krieger, Modeling and Experimental-Verification of Physical and Chemical Processes During Pyrolysis of a Large Biomass Particle, *Fuel*, 64 (1985) 1505-1513.
- [50] C.K. Lee, J.R. Diehl, Combustion of irradiated dry and wet oak, *Combustion and Flame*, 42 (1981) 123-138.
- [51] J.F. Siau, *Transport processes in wood*, Springer-Verlag, 1984.
- [52] C. Di Blasi, Multi-phase moisture transfer in the high-temperature drying of wood particles, *Chemical Engineering Science*, 53 (1998) 353-366.
- [53] M. Fanfei, Z. Mingxu, Influence of initial moisture on pyrolysis of fresh biomass, *International Journal of Oil, Gas and Coal Technology*, 3 (2010) 278-292.

Curriculum Vitae

Jiayi Fang

Department of Energy, Environmental & Chemical Engineering

Washington University in St. Louis

St. Louis, MO, 63130

Phone: (650)288-9061

Email: jiayi@wustl.edu

Education

2011-present PhD Candidate Energy, Environmental & Chemical Engineering

Washington University in St. Louis

2009-2011 M.S. Biological and Agricultural Engineering

University of California Davis

2004-2009 B.S. Biological and Agricultural Engineering

University of California Davis

Professional Experience

2014-present Applied Particle Technology, LLC

CEO and Co-founder

2011-present Energy Environmental and Chemical Engineering, Washington University in St. Louis

Graduate Researcher/teaching assistant. Advisor: Pratim Biswas

Thesis topic: Flame Aerosol synthesis of multicomponent nanoparticles for clean energy applications

- 2009-2011** **Biological and Agricultural Engineering, University of California Davis**
M.S. 2009-2011. Advisor: D.K. Giles
 Thesis topic: Effect of nozzle design on reaction thrust and spray dynamics
- 2008-2011** **Human Exposure Laboratory-University of California San Francisco Lung
 Biology Laboratory**
Research Intern. Advisor: Suzaynn Schick

Volunteer/Non-Profit Experience

- 2015** **The BALSAs Foundation**
 Grant supporter
- 2014-2015** **The BALSAs group**
 Director of Professional Development
- 2012-2015** **The BALSAs group**
 Project Manager
- 2012-2014** **Graduate Student Senate**
 Senator and Sustainability Committee Chair

Journal Publications in Preparation

1. **Fang J.**, Wang Y., Kangasluoma J., Attoui M., Junninen H., Kulmala M., Petäjä T. Biswas, P., The initial stages of multicomponent particle formation during the combustion synthesis of mixed SiO₂/TiO₂, *in preparation*
2. **Fang J.**, Wang Y., Kangasluoma J., Attoui M., Junninen H., Kulmala M., Petäjä T. Biswas, P.; Biswas, P., "Cluster formation mechanisms of titanium dioxide during combustion synthesis", *in preparation*
3. **Fang, J.**, Chadha T., Raliyah R., Gao Z., Banerjee P., and Biswas P., Characterization of nanostructured niobium doped TiO₂ thin films synthesized in a flame aerosol reactor, *in preparation*

Referred Journal Publications

4. Patel, S., Leavey, A., He, S., **Fang, J.**, O'Malley, K., and Biswas, P., Characterization of Gaseous and Particulate Pollutants from Gasification-based Improved Cookstoves DOI: 10.1016/j.esd.2016.02.005, 2016.
5. Wang, Xiaofei, Cotter, E., Iyer, K. N., **Fang, J.**, Williams, B. J., and Biswas, P. Relationship between pyrolysis products and organic aerosols formed during coal combustion. *Proceedings of the Combustion Institute* 35.2 (2015): 2347-2354.
6. Liu, P., Arnold, I. J., Wang, Y., Yu, Y., **Fang, J.**, Biswas, P., and Chakrabarty, R. K. Synthesis of Titanium Dioxide Aerosol Gels in a Buoyancy-Opposed Flame Reactor. *Aerosol Science and Technology* 49.12 (2015): 1232-1241.
7. Wang, Yang, Liu, P., **Fang, J.**, Wang, W. N., & Biswas, P. Kinetics of sub-2 nm TiO₂ particle formation in an aerosol reactor during thermal decomposition of titanium tetraisopropoxide. *Journal of Nanoparticle Research* 17.3 (2015): 1-13.
8. **Fang, J.**; Wang, Y.; Attoui, M.; Chadha, T. S.; Ray, J. R.; Wang, W. N.; Jun, Y. S.; Biswas, P., Measurement of Sub-2 nm Clusters of Pristine and Composite Metal Oxides during Nanomaterial Synthesis in Flame Aerosol Reactors. *Anal. Chem.* **2014**, 86 (15), 7523-7529.
9. Wang, Y.; **Fang, J.**; Attoui, M.; Chadha, T. S.; Wang, W.-N.; Biswas, P., Application of Half Mini DMA for sub 2nm particle size distribution measurement in an electrospray and a flame aerosol reactor. *J. Aerosol. Sci.* **2014**, 71 (0), 52-64.
10. **Fang, J. X.**; Leavey, A.; Biswas, P., Controlled studies on aerosol formation during biomass pyrolysis in a flat flame reactor. *Fuel* **2014**, 116, 350-357.
11. Leavey, A.; **Fang, J. X.**; Sahu, M.; Biswas, P., Comparison of Measured Particle Lung-Deposited Surface Area Concentrations by an Aerotrak 9000 Using Size Distribution Measurements for a Range of Combustion Aerosols. *Aerosol Sci. Technol.* **2013**, 47 (9), 966-978.
12. Schick, S. F., Farraro, K. F., **Fang, J.**, Nasir, S., Kim, J., Lucas, D., Wong, H., Balmes, J., Giles, D. K. and Jenkins, B. (2012). An Apparatus for Generating Aged Cigarette Smoke for Controlled Human Exposure Studies. *Aerosol Science and Technology* 46:1246-1255.

Patents

- 2016 Tandeep Chadha, Jiayi Fang, and Pratim Biswas, Systems and methods for gas cleaning, using electrostatic precipitation and photoionization, US Patent application number 62297270

Research Grants Awarded

- 2016 NSF IIP Division of Industrial Innovation & Partnership, STTR Phase I: Soft X-ray Enhanced Electrostatic Precipitator for High Efficiency Air Purification in Indoor Environments, \$223,865.00, Award No. 1549666

Awards and Fellowships

- 2015 Global Impact Awards Winner
2015-2016 Arch Grants Winner-Summer Cohort
2015 CleanTech Open Midwest-Breakthrough technology of the year
2015 MIT Clean Energy Prize-Semifinalist
2015 Bioentrepreneurship Core Bench to Business Challenge-2nd place
2014 Olin Cup-2nd Place
2012 American Association for Aerosol Research student poster award
2011-2012 Olin W. & LaVerne C. Kriege Fellowship,

Memberships and Associations

Idea Labs	2015-2016
Materials Research Society	2014-2015
American Association for Aerosol Research	2012-2015
Association for Graduate Engineering Students	2012-2014

Oral Presentations

1. *Wang, Y., Li, J., Fang, J., Reed, N., Biswas, P., Studying the charging characteristics of flame generated particles below 3nm with a condensation particle counter batter (CPCB).* American Association for Aerosol Research, October 2015, Minneapolis, MN
2. *Fang, J., Chadha, T.S, Banerjee, P., Biswas, P., Flame aerosol synthesis of niobium doped TiO₂ nanostructured thin films for applications towards transparent conducting oxides,* Materials Research Society Fall Meeting, December 2014, Boston, MA
3. *Chadha, T.S., Fang, J, Biswas, P., “Single Step Aerosol Route Synthesis of Mixed Oxide Nanostructures for Use as Additive Free Lithium Ion Battery Electrodes”* Electrochemical Society, October 2014, Cancun, Mexico
4. *Fang, J., Wang, Y. Biswas, P., Collisional growth below 2nm in flame aerosol reactors* American Association for Aerosol Research, October, 2014, Orlando, FL
5. *Fang, J., Wang, Y., Chadha, T.S., Yang, M., Biswas, P., Evolution of Particle Size Distribution of Pristine and Doped Titanium Dioxide in a Flame Reactor: Role of Various Process Parameters.* American Association for Aerosol Research, October, 2013, Portland, OR

Poster Presentations

1. *Reed, N., Fang, J., Chavalmane, S., Biswas, P., American Association for Aerosol Research, October 2015, Minneapolis, MN*
2. *Fang, J., Chadha, T.S., Biswas, P., Aerosols to Cookstoves, Clinton Global Initiative University Exchange, April 2012, St. Louis MO*
3. *Fang, J., Leavey, A., Biswas, P. Controlled Studies on Aerosol Formation During Biomass Pyrolysis in a Flat Flame Reactor, American Association for Aerosol Research 31st Annual Conference, Oct 2012, Minneapolis, MN*

Coursework

Year	Semester	Course	Title	Credit	Grade
2011	Fall	EECE 501	Transport Phenomena	3	A-
2011	Fall	EECE 548	Environmental Organic Chemistry	3	B
2011	Fall	EECE 518	Aerosol Science and Technology	3	A-
2012	Spring	EECE 503	Kinetics and Reaction Engineering Principles	3	B
2012	Spring	EECE 534	Environmental Nanochemistry	3	A
2012	Spring	ESE 517	Partial Differential Equations	3	A
2012	Fall	EECE 5404	Combustion Phenomena	3	A-